ICCESEN-2025

12th International Conference on Computational and Experimental Science and ENgineering

Antalya-TURKEY

17-20 October 2025

www.iccesen.org iccesen2025@gmail.com

Proceedings of ICCESEN-2025

EDITORS

Prof.Dr. İskender AKKURT

Dr. Sabiha Anas BOUSSAA

ISBN : 978-605-68728-9-1

ICCESEN 17-20 October 2025 Kemer-Antalya-TURKEY www.iccesen.org

12th International Conference on Computational and Experimental Science and ENgineering

Antalya-TURKEY
17-20 October 2025

Proceedings of ICCESEN-2025

Editors:
Prof.Dr. İskender AKKURT
Dr. Sabiha ANAS BOUSSAA

ISBN: 978-605-68728-9-1

Proceedings of ICCESEN-2025 ,

12th International Conference on Computational and Eperimental Science and Engineering (**ICCESEN-2025**)

17-20 October 2025, Antalya-TURKEY

Editors:
Prof. Dr. İskender AKKURT
Dr. Sabiha ANAS BOUSSAA

Published : 31 October 2025
ISBN: 978-605-68728-9-1

TABLE OF CONTENTS

FOREWORD

Dear Colleagues,

It is a great honor for me to host you all in **"12th International Conference on Computational and Experimental Science and Engineering (ICCESEN-2025)"** was taken place in Antalya-TURKEY in the period of 17-20 October 2025.

We are also happy to publish the proceeding of ICCESEN-2025. All papers have been reviewed by two reviewers.

Prof. Dr. İskender AKKURT

Chair for ICCESEN-2025
Editor for Proceedings of ICCESEN-2025

ORGANISATION COMMITTEE

Prof.Dr. Iskender AKKURT (Chair)	Suleyman Demirel University, Isparta -Turkey
Dr. Sabiha Anas BOUSSAA (Secretary)	CRTSE-Algeria
Dr. Hakan AKYILDIRIM	Suleyman Demirel University, Isparta -Turkey
Dr. Nurdan KARPUZ	Amasya University, Amasya -Turkey
Dr. Feride KULALI	Üsküdar University, Istanbul-Turkey
Dr. Osman GÜNAY	Yıldız Technical University, Istanbul -Turkiye
Dr. Feride KULALI	Üsküdar University, Istanbul-Turkey
Dr. Mucize SARIHAN	Okan University, Istanbul-Turkey
Dr. Aycan ŞENGÜL	Akdeniz University, Antalya-Turkey
Lect. Berra Seda SARIHAN	Okan University, Istanbul-Turkey

SCIENTIFIC COMMITTEE

Prof.Dr. Iskender AKKURT (Chair)	Suleyman Demirel University, Isparta –Turkey
Prof.Dr. Majid ABBASPOUR	Sharif University of Technology-Iran
Prof.Dr. Zahid Hussain ABRA	Quadi-E-Awam University, Sindh-Pakistan
Prof.Dr. Abdullah ALAMRI	King Saud University, Saudi Arabia
Prof.Dr. Nezam Mahdavi-AMIRI	Sharif University Iran
Dr.Sabiha Anas Boussaa	CRTSE,Algeria.
Dr. John R.M.ANNAND	Glasgow University, Glasgow-Scotland (UK)
Dr. Majda AOUITITEN	Abdelmalek Essaadi University-Morocco
Prof.Dr. Mohamed Kheireddine AROUA	University of Malaya-Malaysia
Dr. Rachid BELKADA	CRSTSE -Algeria
Dr. Radhey S BENIWAL	CSIR-NISCAIR, New Delhi 110012, India
Dr. Mahmoud Abdullah BENNASER	Kuwait University-Kuwait
Dr. Djoudi BOUHAFS	Centre de Recherche en Technologie -Algeria
Prof. Oleg BURDAKOV	Linköping University Linköping, Sweden
Dr. Yusuf CEYLAN	Selcuk University, Konya-Turkey
Prof.Dr. Lotfi CHOUCHANE	Weill Cornell MEdical College-Qatar
Dr. Manju D CHOUDHARY	Niscair-India
Dr. Nermin DEMİRKOL	Kocaeli University, Kocaeli –Turkey
Prof.Dr. İbrahim DİNÇER	University of Ontario Institue of Technology (UOIT)-Canada
Prof. Dr. Mitra DJAMAL	Institute Teknologi Bandung-Indonesia
Prof.Dr. Mahmut DOĞRU	Bitlis Eren University, Bitlis-Turkey
Prof.Dr. Mohammed Mostafa EL TOKHI	United Arab Emirates University-UAE
Dr. Zuhal ER	Istanbul Technical University, Istanbul-Turkey
Prof.Dr. Mustafa EROL	Dokuz Eylul University, İzmir-Turkey
Prof.Dr. Madjid FATHI	Dept. of EECS University of Siegen- Germany
Prof.Dr. Jan FELBA	Wroclaw University of Technology-Poland
Prof.Dr. S. Mostafa GHIAASIAAN	Mechanical/Nuclear Engineering, Georgia Tech USA
Prof.Dr. Mustafa GÜNAL	Gaziantep University, Gaziantep-Turkey
Prof. Dr. Amir HUSSAIN	University of Stirling- Scotland(UK)
Dr. Nabi IBADOV	Warsaw University of Technology-Poland
Prof.Dr. Fatma KARİPCİN	Nevşehir Hacı Bektaşi Veli University-Turkey
Prof.Dr. Hamdi Ş. KILIÇ	Selcuk University, Konya-Turkey

Dr. Menekşe V. KILIÇARSLAN	İstanbul Aydın University, Istanbul-Turkey
Prof.Dr. Ziya Erdem KOÇ	Selcuk University, Konya-Turkey
Prof. Dr. İsmail KOYUNCU	Istanbul Technical University, Istanbul-Turkey
Dr. Irida MARKJA	Polytechnic University,Tirana-Albania
Dr. F.Zümrüt Biber MÜFTÜLER	Ege University, Izmir-Turkey
Dr. Susan Shukur NOORI	Kirkuk University, Kirkuk-lraq
Prof.Dr. Ravindra NUGGEHALLI	New Jersey Institute of Technology-USA
Prof.Dr. İbrahim ÖRÜN	Aksaray University, Aksaray-Turkey
Prof.Dr. Necati ÖZDEMİR	Balıkesir University, Balıkesir-Turkey
Dr. Zeynep PARLAR	Istanbul Technical University, Istanbul-Turkey
Prof.Dr. Ioana G. Petrisor	ToxStrategies, Inc., Mission Viejo, CA
Dr. Tomasz PIOTROWSKI	Warsaw University of Technology, Warsaw-Poland
Prof.Dr. Javad RAHIGHI	AEOI, Tehran-Iran.
Dr. Abdelmadjid RECIOUI	University of Boumerdes-Algeria
Prof.Dr. Osman SAGDIÇ	Yıldız Technical University, Istanbul-Turkey
Prof.Dr. Miljko SATARIC	Faculty of Technical Sciences Novi Sad-Serbia
Prof.Dr. Saleh SULTANSOY	TOBB University, Ankara-Turkey
Dr. Naim SYLA	University of Prishtina-Kosova
Prof. Dr. Mustafa TAVASLI	Uludag University, Bursa-Turkey
Dr. Huseyin TOROS	Istanbul Technical University, Istanbul-Turkey
Prof.Dr. Ahmad UMAR	Najran University-Saudi Arabia
Prof.Dr. Gerhard-Wilhelm WEBER	Middle East Technical University Ankara-Turkey
Prof.Dr. Erol YAŞAR	Mersin University, Mersin-Turkey

INVITED SPEAKERS

Prof. Dr. Amir HUSSEIN

Edinburgh Napier University, UK

Title: Trustworthy AI-enabled Sustainable Technologies

Prof.Dr. Madjid FATHI

Dept. of EECS University of Siegen, GERMANY

Title: Artificial Intelligent as a Concept or as a System: utilizing and conceptualizing AI in Industrial and health care

Dr. Hayat ARBOUZ

University Saad Dahlab Blida1, Algeria

Title: Investigation of the potential of the double perovskite materials Cs2BX6 and Cs2BB'X6 as absorbers in single and tandem solar cells for high-efficiency photovoltaic conversion

Prof.Dr. Mansour Almatarneh

University of Jordan-Jordan

Title: Sustainable Development in the Global Rankings

Prof.Dr. Gerhard-Wilhelm WEBER

Poznan University of Technology-POLAND

Title: Regime-switching models via stochastic optimal control & robust control theory, with applications in finance and insurance

Integrating Computational Modeling with Experimental Methods in Bending Behavior Analysis of Round Rods

Rilindë RAÇI[1], Latif HASI[2*]

[1] *University of Prishtina/Faculty of Mathematics and Natural Sciences/Department of Phsyics, Prishtina, Kosova*

[2*] *University of Prishtina/Faculty of Mechanical Engineering, Prishtina, Kosova*

latif.hasi@uni-pr.edu

ABSTRACT

The integration of modeling software into scientific research has gained significant traction as a reliable complement to traditional experimental methods. This study examines the mechanical behavior of three different round rods under three-point bending tests, combining experimental procedures with computational simulations. Using ANSYS software, the bending tests are modelled to analyze stress distribution, deflection, and overall material performance. A comparative analysis between experimental results and simulations evaluates the accuracy and reliability of computational modeling in replicating physical behavior. By highlighting the potential of modeling software in predicting material responses under loading conditions, this study underscores its growing significance in both engineering research and educational applications.

KEYWORDS - Three-point bending test, Finite element analysis (FEA), ANSYS simulation.

1. INTRODUCTION

A Three-Point Bend test is performed on a round rod as shown in Figure 1. As a downward force (F) is applied in the middle of the rod, the flex (Δx) is recorded. The ratio (F/Δx) is the effective stiffness of the length of rod being tested. The distance between the anvils (see inset) is varied, and the resulting effect on the stiffness of the beam is measured. A graph of the resulting data yields the Flexural Elastic Modulus for the material. (PASCO)

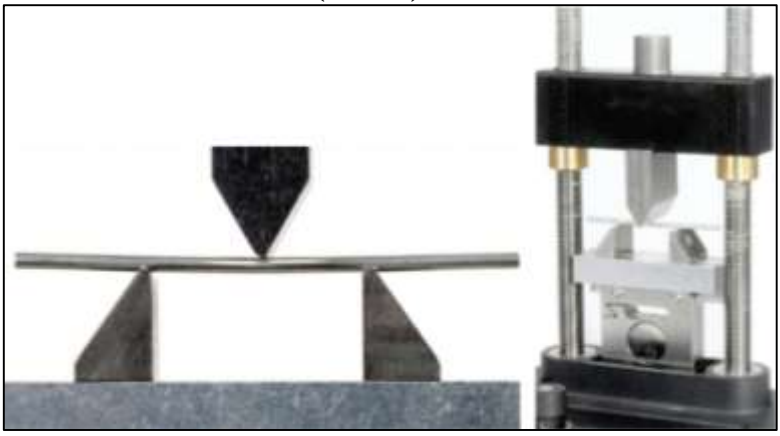

***Figure 1**. Three-point bending (PASCO)*

After completing the experimental measurements, we continue by modelling the same problem with the same parameters in the ANSYS modelling software. This is a computer program that enables the modelling of various physical and engineering problems and simulating them to generate results as if by experiment. A great advantage of this program is that in its database there is data for many different materials. Also, if we use a material that is not recognized by ANSYS, we can determine the parameters of that material (Young's Modulus, Flexural Modulus, Poisson's ratio, etc.) experimentally and then use that data to model more complex structures and simulate them for testing, thus saving us a lot of time and materials.

2. EXPERIMENTAL METHODS

A sample is supported by two anvils placed at a distance, L, as shown in Figure 2. A force F of $100N$ is applied in the middle, at an equal distance from each anvil, and the deflection Δx is measured. The force is applied by moving the upper anvil, namely by rotating its upper part which causes the vertical displacement of the anvil. The distance between the two anvils is changed several times and in each case $F/\Delta x$ is measured, which we read in the PASCO Capstone program.

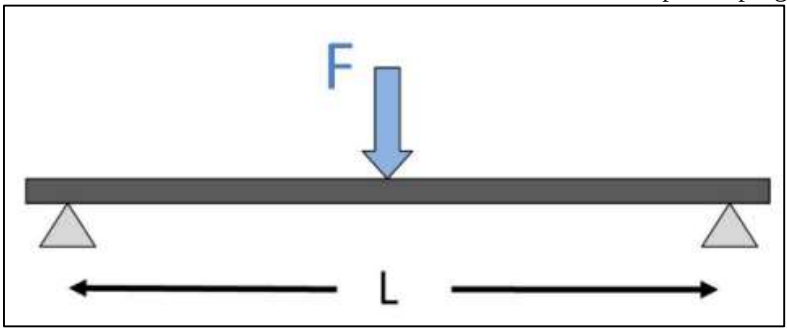

***Figure 2**. 3-Point Bending Test (PASCO)*

The ratio $F/\Delta x$ is the stiffness of the sample, and depends on the length, L. It also depends on the shape and cross-sectional area of the sample, as well as the material. If E is the flexural modulus for the material, and I is the surface moment of inertia for the sample, then:

$$\frac{F}{\Delta x} = \frac{48IE}{L^3}$$

The Area Moment of Inertia depends on the shape of the cross section of the sample. For a round rod of radius, r,

$$I_{rod} = \frac{1}{4}\pi r^4$$

Thus, we see from Eqn. (1) that the stiffness (F/Δx) is inversely proportional to the cube of the anvil separation, L, and a graph F/Δx vs. $1/L^3$, yields a straight line with a slope = 48IE. Finally, solving for E yields

$$E = \frac{gradient}{48I}$$

(PASCO)

Flexural modulus is technically not the same as Young's modulus. Flexural testing involves tensile and compressive stresses, and for some materials these moduli are different. For isotropic and homogeneous materials, these two moduli have the same values, but for some materials, such as

composites and polymers, the flexural modulus is greater than Young's modulus due to the nonlinearity of the material in bending.
The measurements were performed using PASCO Capstone. There we generate a table $F/\Delta x$ *vs* L. Its graph will highlight the fact that the hardness is inversely proportional to the cube of the distance between the two anvils.
The same procedure was repeated for three different materials: aluminum, steel, and brass.

3.EXPERIMENTAL RESULTS

These are experimental measurements carried out in the laboratory.

Table 1. *Experimental results for Aluminum*

L (m)	F/Δx (N/m)
0.079	33900
0.0645	59900
0.045	184000
0.031	577000

Table 2. *Experimental results for Steel*

L (m)	F/Δx (N/m)
0.050	347000
0.077	89400
0.033	1240000
0.027	2540000

Table 3. *Experimental results for Brass*

L (m)	F/Δx (N/m)
0.078	50700
0.057	125000
0.038	445000
0.027	1250000

3.1Analysis of experimental results

From the experimental measurements, we are first generating the graph $F/(N/m)$ versus $L(m)$ for each material.

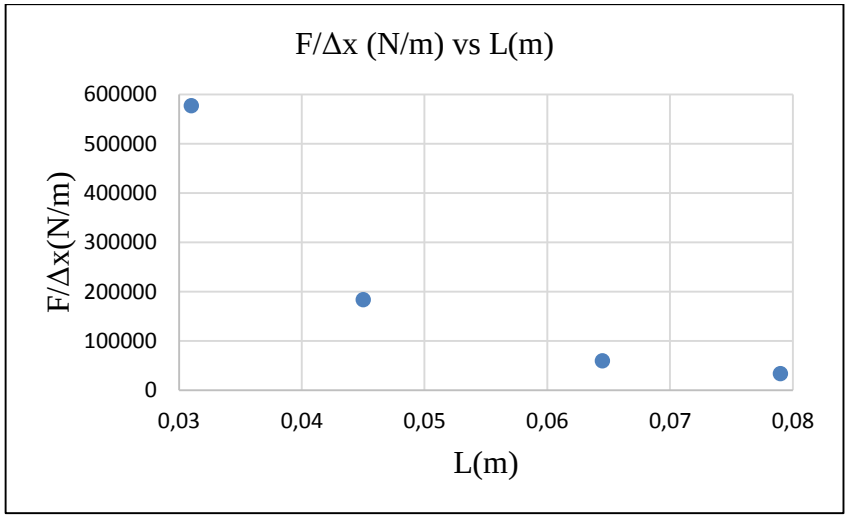

Figure 3. *Graph of stiffness F/Δx versus distance L for aluminum*

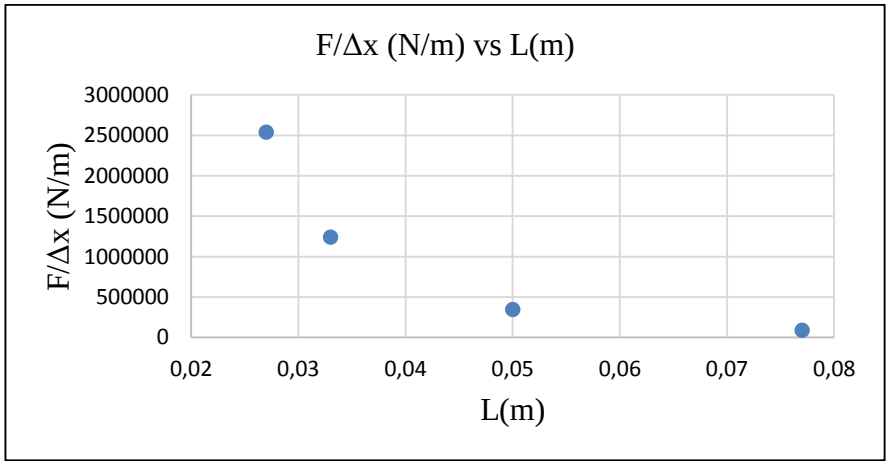

Figure 4. *Graph of stiffness F/Δx versus distance L for steel*

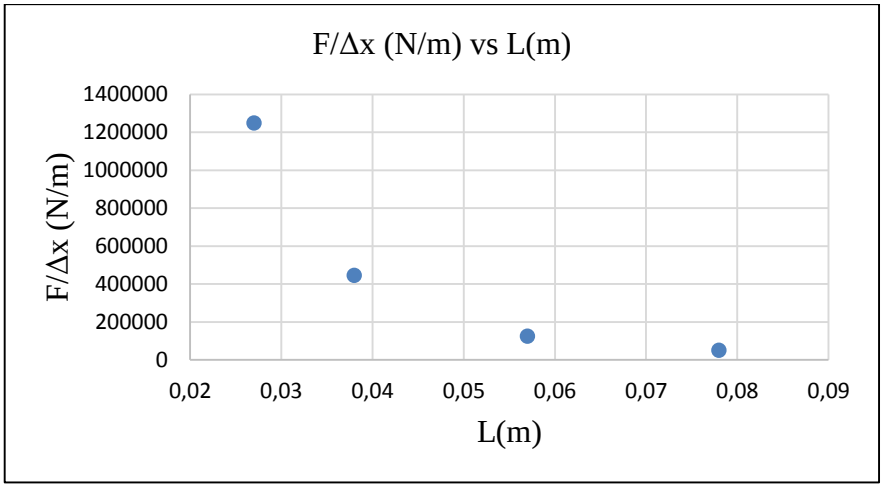

Figure 5. *Graph of stiffness F/Δx versus distance L for brass*

From the graphs above (figures 3,4, and 5) it is clear that the strength of the material is inversely proportional to the cube of the distance between the holding anvils. If we generate the graph of $F/\Delta x$ against $1/L^3$, we will obtain a linear graph.

3.1.1Material 1 (aluminium)

Below I am presenting the graph of the material's hardness $F/\Delta x$ against L^{-3}. This is expected to give us a linear graph based on equation (1), where the gradient of this line will be equal to $48IE$.

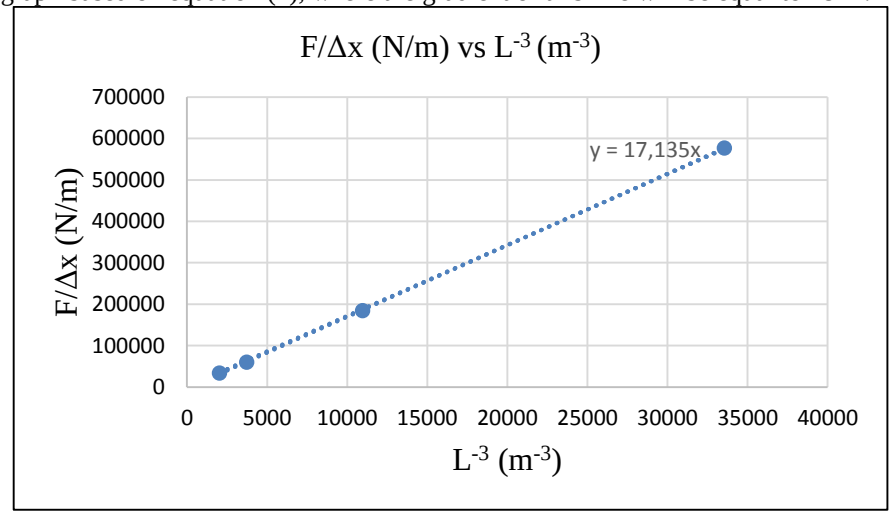

Figure 6. *Graph of F/Δx versus L-3 for aluminum*

As expected, this graph is a straight line. The next step is to determine the gradient of this line. Then, using equation (3), we can calculate the flexural modulus, after calculating the moment of inertia using equation (2). I will calculate the gradient of the line in the above graph using the method of least squares. This can also be done in Excel, which is able to generate the best-fit line. It generates the line and the equation of this line. An important step here is to select the Set intercept option and

make the intercept zero. This is because equation (3), through which we will calculate the value of the modulus E, does not have an intercept.

For this material, Excel has provided this equation:

$$y = 17.235x$$

Here the variable y represents the stiffness $F/\Delta x$, while x represents $L{-}3$. We see that the gradient of this line is 17.135. From equation (3) we find:

$$E = (89.79 \pm 0.51)GPa$$

We calculate the uncertainty using the LINEST function, which finds the uncertainty in the gradient, through which we then find the uncertainty in E.

According to the method of least squares we have these two formulae:

$$m = \frac{n\sum xy - \sum x \sum y}{n\sum x^2 - (\sum x)^2} \tag{5}$$

$$c = \frac{\sum y - m\sum x}{n} \tag{6}$$

Replacing x with L^{-3}, and y with $F/\Delta x$, we get:

$$m = \frac{n\sum(L^{-3})(F/\Delta x) - \sum(L^{-3})(\sum F/\Delta x)}{n\sum(L^{-3})^2 - (\sum L^{-3})^2} \tag{7}$$

$$c = \frac{\sum(F/\Delta x) - m\sum(L^{-3})}{n} \tag{8}$$

I entered these formulas in Excel and obtained these values:

$$m = 17.27535 \approx 17.3, c = -3520.41 \approx -3520.4 \tag{9}$$

We obtain the same values in Excel if we do not make the intercept zero. From the gradient value we obtain the value of the flexural modulus: $9.05 \cdot 10^{10}\frac{N}{m^2} = 90.5GPa$. The least squares method described above does not make the intercept zero so it gives us another result, which is not so reliable. The value stated above fits the expected value for aluminium alloys which is expected to be in the range 70-90GPa.

3.1.2Material 2 (steel)

We are continuing the same procedure for the second material. First, I am presenting the graph of $F/\Delta x$ against L^{-3}.

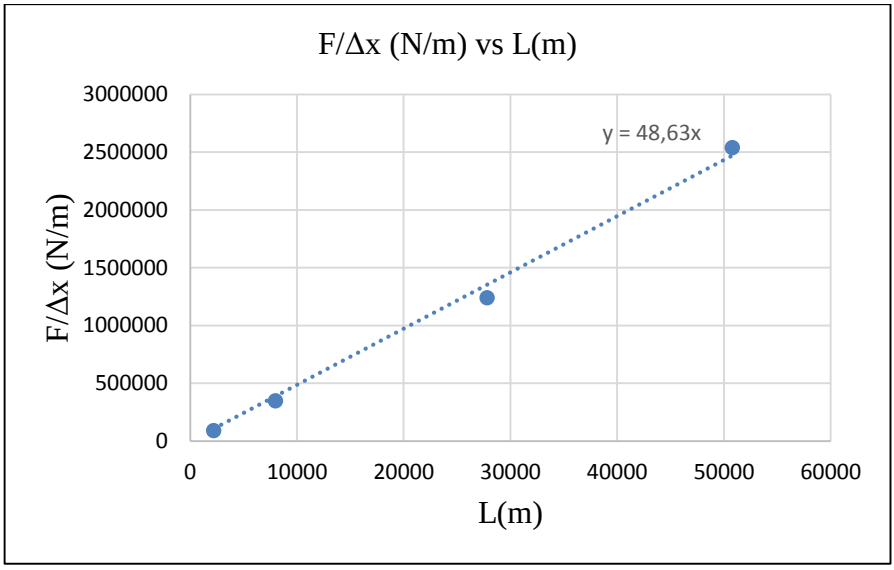

Figure 7. *Graph of F/Δx versus L^{-3} for steel*

It can be seen that the gradient of the best-fit line is equal to 48.63. Using the method of least squares, I obtained the value 50.30239 (without forcing the line to pass through the point (0,0)).
Using the same equations as for the first material, we obtain a value of the flexural modulus of

$$E = (254.81 \pm 7.23)GPa$$

This value is significantly higher than the common value of steel alloys, which have flexural moduli of around $200GPa$.

3.1.3Material 3 (brass)

Below I present the F/Δx vs. L^{-3} graph for the third material.

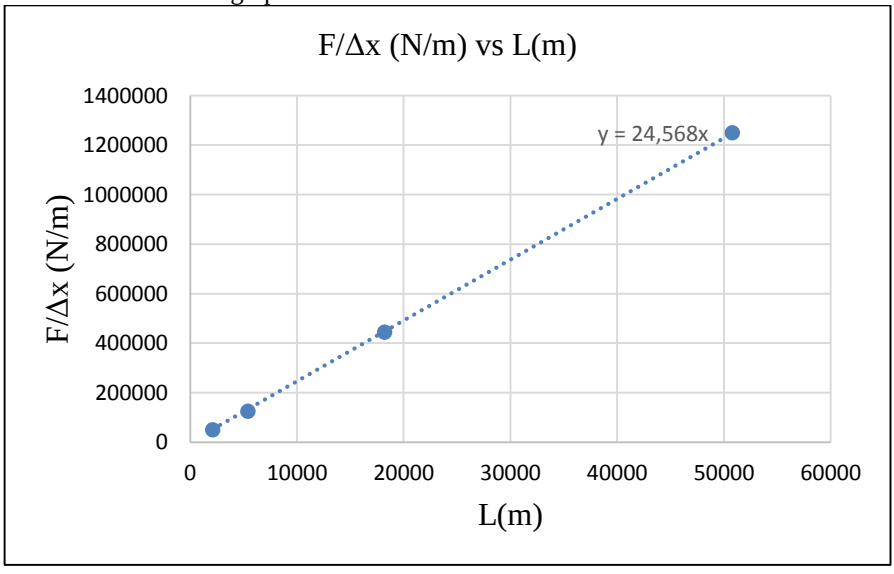

Figure 8. *Graph of F/Δx versus L^{-3} for brass*

We can see that the gradient of the best-fit line is equal to 24.568. Using the method of least squares, I obtained the value 24.69176. Using the same equations as for the first material, we obtain a value of the flexural modulus of $E = (128.73 \pm 0.47)GPa$.
For brass, which is a copper-nickel alloy, a value of the flexural modulus in the range $90 - 110GPa$ is expected. It is seen that our sample has a significantly higher value of this modulus.

4.MODELING IN ANSYS

In the ANSYS program, I have modeled a thin metal rod with a cylindrical shape with a radius of $1.5mm$ and a length of $100mm = 10cm$ which is supported at two points. I will generate the supporting rods by adding the condition that these rods are stationary (static). Then, right in the middle of the rod, I will place a force of $100N$ with a vertically downward direction. To make the problem as realistic as possible, I can also add the gravitational force, in which case the bending contribution due to the weight of the rod itself is also added. For the dimensions of our rods, we do not expect a large force, so this contribution is not expected to be very large, but this practice can be very useful in other modeling cases, e.g. if the rod represents a part of the structure of a building or house, where this rod can have the function of supporting the floor, there, due to the larger dimensions of the rod, we would be dealing with a greater weight of the rod that could significantly affect its strength and bending, as well as the safety of the residents.
I will note all lengths in mm, so I must choose the mm unit before starting to model this problem. I made the geometry of the experiment using Design Modeler and Space Claim that ANSYS Workbench enables.
First, I generated a cylinder with a radius of 1.5mm (diameter 3mm) and a length of 100mm (10cm) that fits the length of the sample used in the laboratory. As for the supporting anvils, it is not necessary to draw them. It is enough to know the coordinates of the meeting points between the anvils and the rod. Then, at those points, we set the movement constraints. We limit the movement in the vertical direction (the y axis), because these points should not move in this direction since they represent the support points. However, we should leave them free to move in the x and y directions, as well as rotations. I set these support points at distances L=60mm, 70mm, 80mm, and 90mm; and I generated the results for these distances. I did this for the Structural Steel, Aluminum Alloy, and BRASS materials, which are in the ANSYS material database.

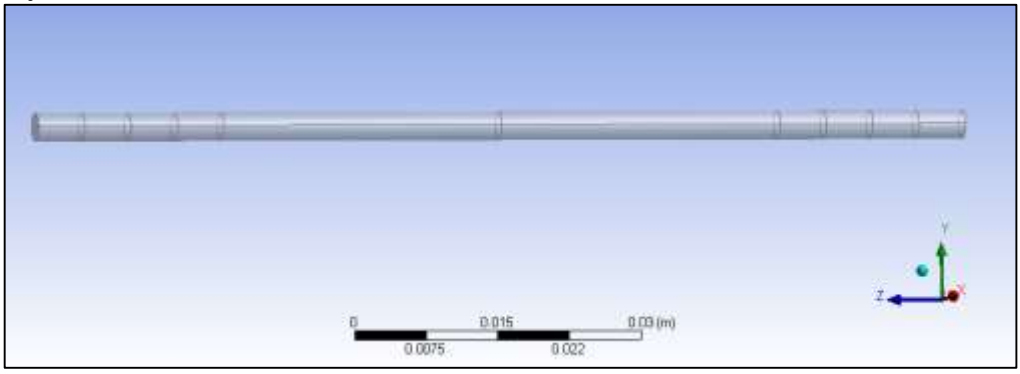

Figure 9. *Model geometry in ANSYS Workbench (Design Modeler)*

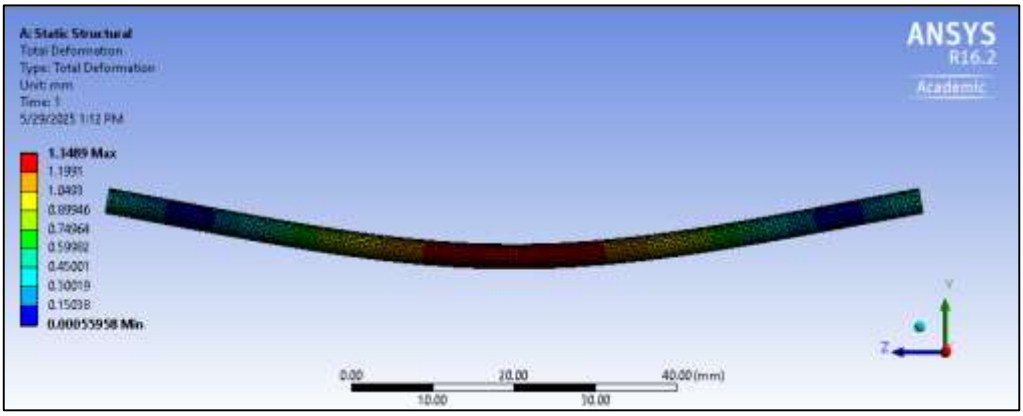

Figure 10. *Curvature generated in ANSYS Workbench*

4.1ANSYS results

These are the results generated in ANSYS.

Table 4. *ANSYS Results for Structural Steel*

L (m)	F/Δx (N/m)
0.06	174972.0045
0.07	110717.4491
0.08	74134.47995
0.09	51639.5559

Table 5. *ANSYS Results for Aluminum Alloy*

L (m)	F/Δx (N/m)
0.06	62262.62375
0.07	39277.29772
0.08	26143.79085
0.09	18248.17518

Table 6. *ANSYS Results for BRASS*

L (m)	F/Δx (N/m)
0.06	104128.7031
0.07	65932.61687
0.08	44016.02183
0.09	30726.68613

4.2Analysis of ANSYS results

Based on the ANSYS Workbench results, we first generate the $F/(N/m)$ versus $L(m)$ graph for each material.

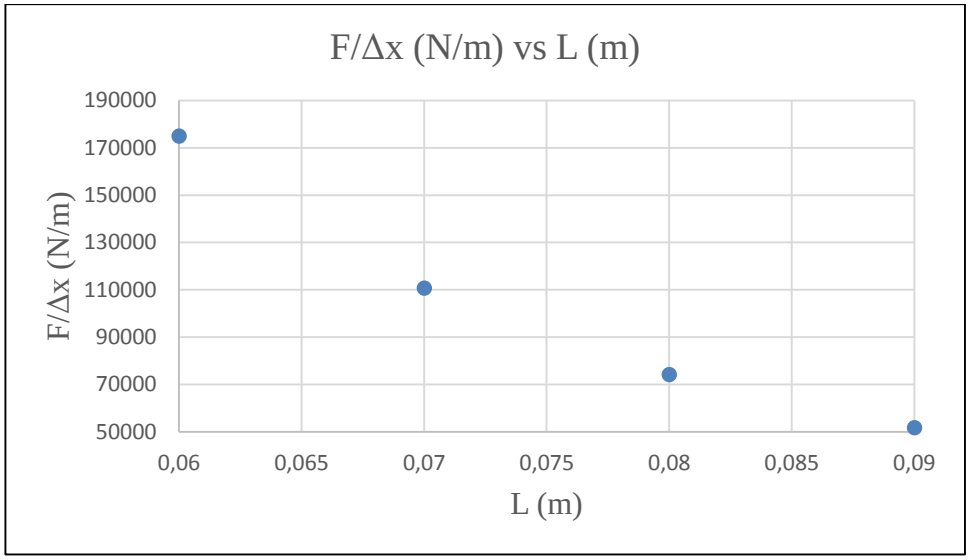

Figure 11. *Graph of strength F/Δx versus distance L for Structural Steel*

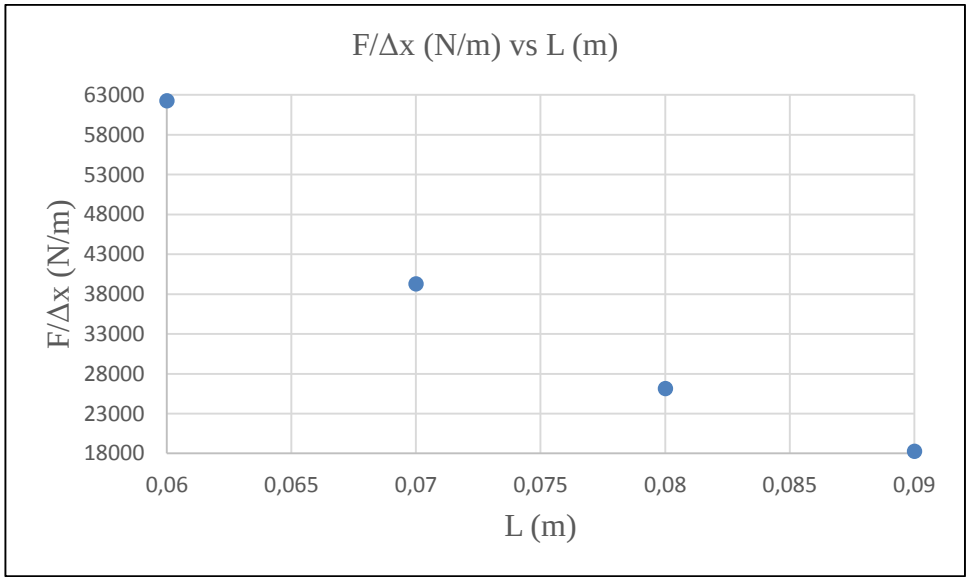

Figure 12. *Graph of strength F/Δx versus distance L for Aluminum Alloy*

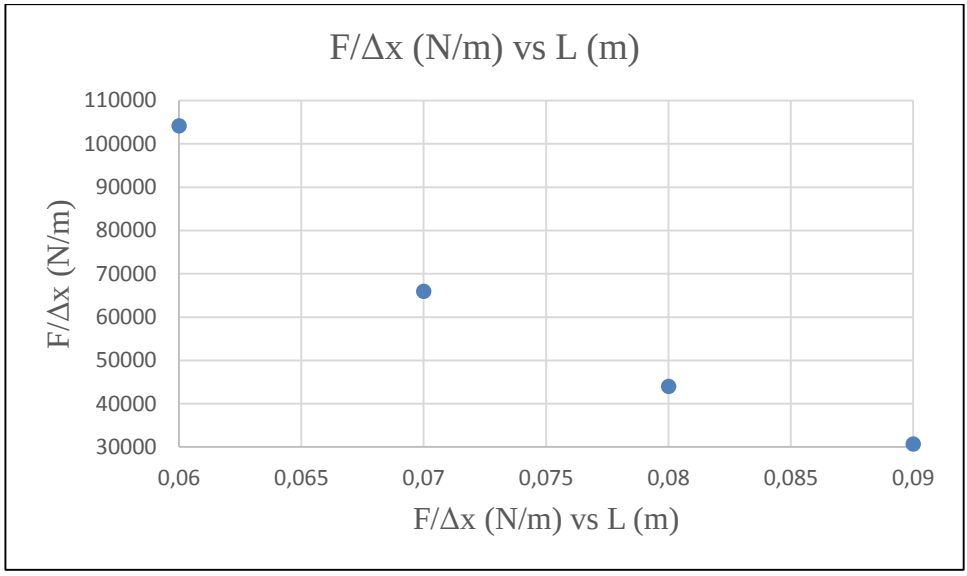

Figure 13. *Graph of strength F/Δx versus distance L for BRASS*

Now we can generate graphs of strength versus $1/L^3$ to see if the graph is linear like the graphs of experimental measurements.

4.2.1Material 1 (Structural Steel)

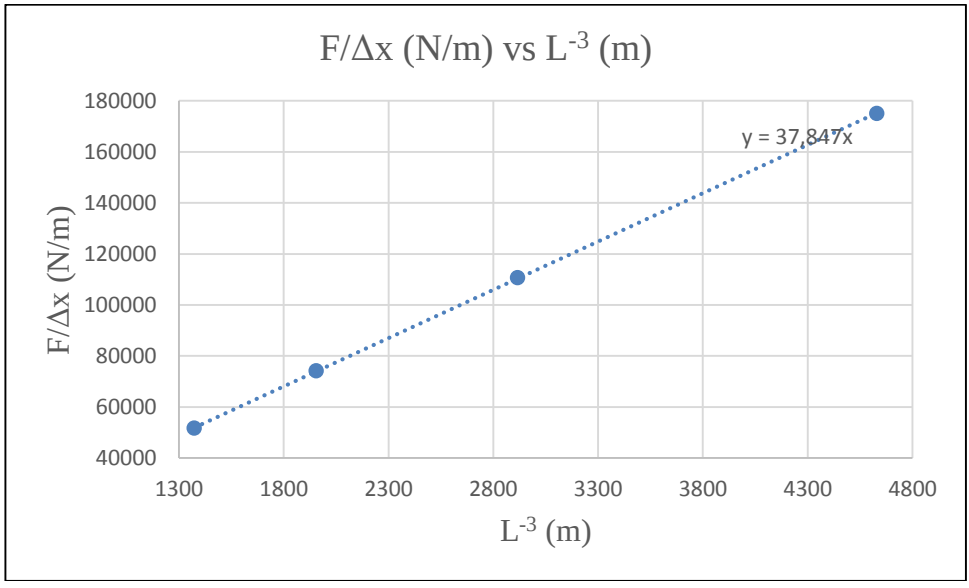

Figure 14. *Graph of F/Δx vs. L^{-3} for Structural Steel*

We see that the equation of the line (best fit) is:

$$y = 37.847x \quad (10)$$

Now using equation (3) we calculate the value of the flexural modulus and obtain the value of:

$$E = (198.31 \pm 0.29)GPa$$

4.2.2Material 2 (Aluminum Alloy)

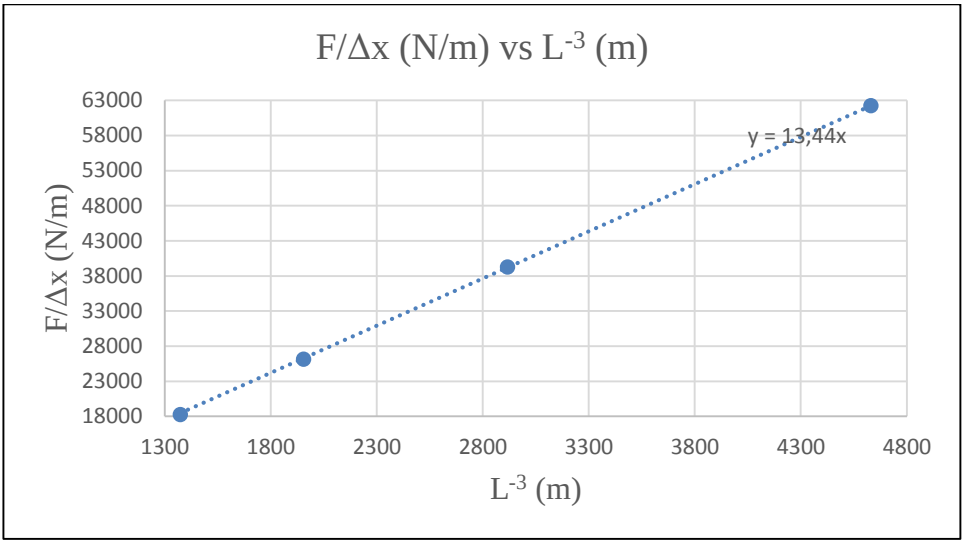

Figure 15. *Graph of F/Δx vs. L^{-3} for Aluminum Alloy*

We see that the equation of the line (best fit) is:

$$y = 13.44x \quad (11)$$

Now using equation (3) we calculate the value of the flexural modulus and obtain the value of:

$$E = (70.42 \pm 0.12)GPa$$

4.2.3Material 3 (BRASS)

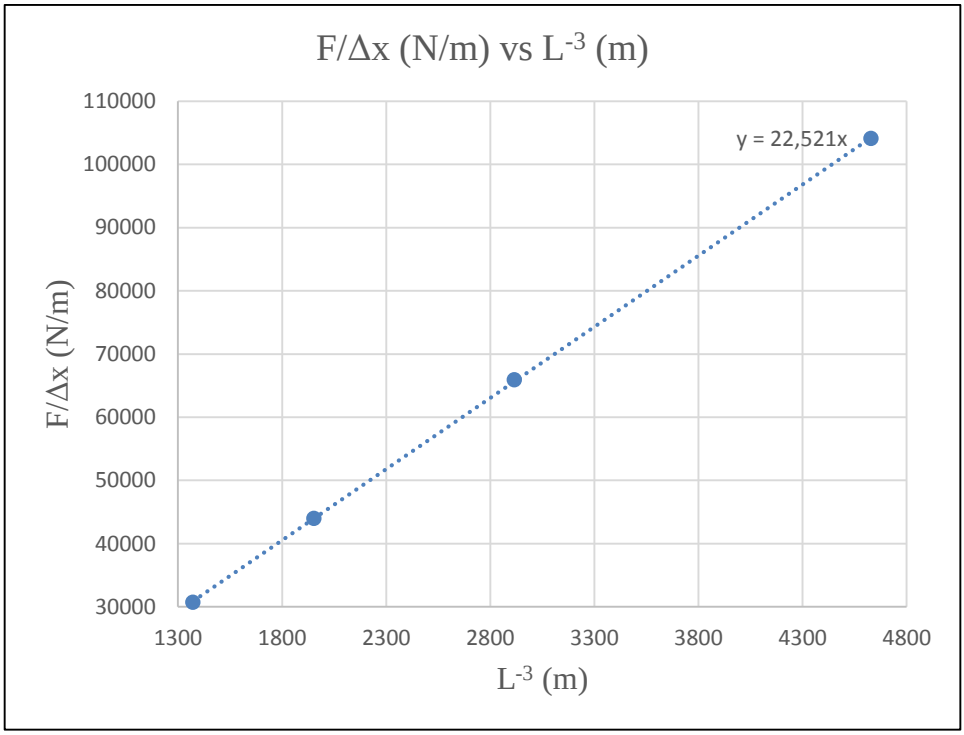

Figure 16. *Graph of F/Δx vs. L^{-3} for BRASS*

We see that the equation of the line (best fit) is:

$$y = 22.521x \tag{12}$$

Now using equation (3) we calculate the value of the flexural modulus and obtain the value of:

$$E = (118.00 \pm 0.18)GPa$$

5.EVALUATION OF RESULTS GENERATED BY ANSYS BY COMPARISON WITH EXPERIMENTAL RESULTS

We see that the results generated by ANSYS, as well as those obtained from the experiment, obey the theory and relations presented at the beginning of this paper.

If we analyze the correlation coefficient for the graphs of the hardness F/Δx versus L^{-3}, we have a coefficient very close to 1, and in fact in the results generated by the software it can even be equal to 1. This is because the software relies on formulas and theories and according to them generates data that match very well. The fact that the correlation coefficient for laboratory measurements is very close to 1 increases the reliability of these measurements, because the best-fit line describes the points of the graph very well and passes through them.

It should be noted that the results generated by ANSYS are significantly improved when, instead of drawing the retaining pins, we set constraints on the movement at those points where these pins should touch the sample. If we decide to draw and generate those pegs as bodies, we must be very careful when defining the contact points. The program provides several options for these contact points and depending on which one we choose (or what coefficient of friction we give at those

points) it has an effect on the generated results, and can even add uncertainty or even points that do not fit in the graph (outliers).

5.CONCLUSIONS AND RECOMMENDATIONS

Considering that the results generated by ANSYS are very similar to the experimental results, except for the fact that we do not have exactly the same materials in the program database, we recommend that in cases of application in engineering or something else, for any sample/material to be used, first determine the properties and parameters of the material, such as Young's Modulus and Poisson's ratio, and then model the system in the software.

This program can be very useful in engineering applications of modeling various building structures or something similar.

Also, if there are other factors that may affect the results, they should be determined and included in the modeling, depending on the level of accuracy required.

REFERENCES

[1] W.D. Callister Jr., D.G. Rethwisch, Materials Science and Engineering: An Introduction, Wiley.
[2] B. Dalipi, et al., Modeling of thermal stresses on steel beam, Int. J. Comput. Exp. Sci. Eng. 11 (2025). DOI: https://doi.org/10.22399/ijcesen.767
[3] D. Halliday, R. Resnick, Fundamentals of Physics, 10th ed., Wiley, 2014.
[4] PASCO, Three-Point Bending.
[5] N. Syla, F. Aliaj, Finite-element modelling and experimental study of nitrogen concentration profile in 16MnCr5 gas nitrided steel, Sci. Res. Essays 10 (19) 615–623. DOI: https://doi.org/10.5897/SRE2015.6331
[6] E. Tunca, H. Kafalı, Compression and three-point bending analyzes of aerospace, Eur. J. Sci. Technol. (2021). DOI: https://doi.org/10.31590/ejosat.1012658
[7] L. Hasi, R. Raçi, N. Hasi, Using modeling software as an alternative to experiment: The magnetic field of a Helmholtz coil, Int. J. Comput. Exp. Sci. Eng. 11 (2025). DOI: https://doi.org/10.22399/ijcesen.653
[8] A.N. Aldeen, Y. Can, M. Yazici, Modeling hyperelastic materials by MATLAB, Int. J. Comput. Exp. Sci. Eng. 6 (2020) 144–148. DOI: https://doi.org/10.22399/ijcesen.662707
[9] S. Bartels, Finite element simulation of nonlinear bending models for thin rods and plates, Comput. Struct. 225 (2020) 106–119. https://doi.org/10.1016/j.compstruc.2019.106119
[10] L. Novotný, Finite element simulation of bending of steel bar including plasticity, Adv. Mater. Res. 1105 (2015) 101–106. https://doi.org/10.4028/www.scientific.net/AMR.1105.101
[11] Q.J. Chen, et al., Experimental study on bending behavior of cold-rolled deformed steel bars reinforced concrete slabs, Adv. Mater. Res. 639–640 (2013) 341–345. https://doi.org/10.4028/www.scientific.net/AMR.639-640.341
[12] M. Obst, et al., Experimental investigation of four-point bending of thin cold-formed C-channel steel beams, Sci. Rep. 12 (2022) 1–10. https://doi.org/10.1038/s41598-022-10035-z
[13] V. Kahya, M. Turan, Bending of laminated composite beams by a multi-layer finite element based on a higher-order theory, Acta Phys. Pol. A 132 (3) (2017) 473–475. DOI: https://doi.org/10.12693/APhysPolA.132.473

Özel Öklid Lie Grubu SE(2)

Elif Akgün Aslan , Mehmet Sezgin

Edirne Sosyal Bilimler Lisesi , Trakya Üniversitesi Fen Fakültesi Matematik Bölümü
Edirne , Türkiye
elifakgunaslan@trakya.edu.tr , msezgin22@yahoo.com

ÖZET

Bu çalışmada ilk önce Lie grubu tanımı ve $SE(2)$ grubu ifade edildi. Daha sonra bu grubun sonsuz küçük operatörleri ve Casimir operatörü elde edildi. Bu operatörle oluşturulan özdeğer ve özfonksiyon probleminin çözümü verildi. Fiziksel bir sistemin Hamiltonyeni ile sistemin simetri grubunun Casimir operatörü arasındaki ilişkiden Schrödinger denkleminin çözümü olan dalga fonksiyonu elde edildi.

Anahtar Kelimeler : Lie grubu, Casimir operatörü, Schrödinger denklemi

1. GİRİŞ

Evariste Galois ilk defa 1830 da grup yapısından bahsetmiş ve her polinomu, polinomun köklerinin bir permütasyon grubuyla eşleştirmiştir. Böylece grup teorisinin temelleri atılmış ve sonraki yıllarda teori büyük gelişmeler göstermiştir. Galois'nın cebirsel denklemleri çözmek için grup teoriyi kullanması Norveçli bilim adamı Marius Sophus Lie'yi de kendi çalışması için benzer bir tekniğe yönlendirmiştir. Sonlu grupların denklemlerin çözülebilirliğine karar vermede kullanılması, sonsuz grupların da adi veya kısmi diferansiyel denklemlerin çözümü ile ilişkisi olabileceği görülmüştür. Bunun üzerine Lie, adi diferansiyel denklemleri çözmede kullanılan karmaşık teknikleri bir düzene koymak için simetri dönüşümlerinin sürekli bir grubu fikrini ortaya koymuş ve çalışmalarını bu fikir üzerine kurarak Lie teorisini geliştirmiştir. Günlük hayatımızdaki birçok problemin matematiksel ifadesi olan diferansiyel denklemlerin çözümleri araştırılırken bu problemlerin geometrik yapıları ve simetri özelliklerine başvurulur. Lie grubu ve cebiri teorisinde kullanılan temel yöntemler simetri yapısına dayanır. Bu nedenle teori, uzun yıllardır matematiğin birçok alanında kullanılmıştır [1,2,3,4,5].

Lie gruplarını homojen ve homojen olmayan gruplar olarak düşünebiliriz. Homojen olmayan Lie grupları, standart hareket gruplarının ötesine geçerek daha karmaşık yapıların incelenmesine imkân tanır. Bu tür gruplar, robotların ve farklı mekanik kısıtlamalara sahip sistemlerin matematiksel analizinde önemli bir araç olarak kullanılır. Özellikle Robotik sistemlerin modellenmesinde Lie grupları önemli bir rol oynar. Örneğin uzayda dönme ve öteleme hareketlerini temsil eden $SE(3)$grubu, robotların hareketlerini tanımlamak için temel bir matematiksel yapı sağlar. Günümüzde robotlar, endüstriden sağlığa kadar pek çok alanda verimliliği artıran ve insan yaşamını kolaylaştıran teknolojiler olarak büyük önem taşımaktadır [6].

G boş olmayan bir küme olsun. Eğer aşağıdaki koşullar sağlanıyorsa, G bir Lie grubudur.

1. G bir grup,
2. G türevlenebilir bir manifold,
3. G grubu üzerinde tanımlanan grup işlemi

$$f : G \times G \to G,\ f(g,h) = gh\,, \quad g,h \in G$$

ve ters işlemi

$$u : G \to G\,,\ u(g) = g^{-1}\,, \quad g \in G$$

türevlenebilirdir.

Matematikte ve bilimin diğer alanlarında ortaya çıkan Lie gruplarının birçoğu matris gruplarıdır. Bu alanlarda sıklıkla karşılaşılan matris gruplarına birkaç örnek verelim.

$$GL(n,\mathbb{R}) = \{A = (a_{ij}) |\ a_{ij} \in \mathbb{R},\ i,j = 1,2,\dots,n,\ \det A \neq 0\}$$
$$SL(n,\mathbb{R}) = \{A \in GL(n,\mathbb{R}) |\ \det A = 1\}\,,\ O(n,\mathbb{R}) = \{A \in GL(n,\mathbb{R}) |\ A^t = A^{-1}\}$$
$$SO(n,\mathbb{R}) = \{A \in O(n,\mathbb{R}) |\ \det A = 1\}$$

Üstel fonksiyon, matematiğin birçok dalında karşımıza çıkar. Lie teorisinde bir matrisin üsteli, bir Lie grubuna karşılık gelen Lie cebirini tanımlamada ortaya çıkar ve Lie cebirlerine karşılık gelen Lie gruplarına bilgi aktarımı sağlayan bir mekanizma görevi görür. Yani, Lie teorisinde bir matrisin üsteli, Lie cebiri ile ona karşılık gelen Lie grubu arasındaki ilişkiyi kurar. Grubun özellikleri kendisine karşılık gelen cebirin özellikleriyle yakından ilişkilidir. Her bir Lie grubuna bir Lie cebiri karşı gelir. Bilinen bazı Lie gruplarına karşılık gelen Lie cebirlerini yazalım. $SL(n,\mathbb{R})$, $SO(n,\mathbb{R})$, $U(n,\mathbb{C})$, $SU(n,\mathbb{C})$ gruplarının cebirleri sırasıyla aşağıdaki gibi verilebilir.

$$sl(n,\mathbb{R}) = \{A \in gl(n,\mathbb{R}) |\ \mathrm{tr}(A) = 0\}\ ,\ so(n,\mathbb{R}) = \{A \in gl(n,\mathbb{R}) |\ A + A^T = 0\}$$
$$u(n,\mathbb{C}) = \{A \in gl(n,\mathbb{C}) |\ A + (\bar{A})^T = 0\}\ ,\ su(n,\mathbb{C}) = \{A \in gl(n,\mathbb{C}) |\ A + (\bar{A})^T = 0,\ \mathrm{tr}(A) = 0\}$$

Buraya kadar homojen olan Lie grupları ve cebirleri hakkında bazı temel bilgiler verdik. Çünkü homojen olmayan Lie grupları homojen olan grupları da içerir. Şimdi homojen olmayan Lie gruplarına ait bazı örnekler verelim.

Poincare grubu (Homojen olmayan Lorentz grubu) $P(n,1)$, $\mathbb{R}^{n+1}$'deki tüm

$$x' = Ax + b\,, \quad A \in O(n,1)\,,\ b \in \mathbb{R}^{n+1}$$

şeklindeki dönüşümler grubudur. Başka sözle bu grup, $\mathbb{R}^{n+1}$ de uzunluğunu koruyan afin dönüşümler grubudur ve $A \in O(n,1)$ olmak üzere $(n+2)\times(n+2)$ formundaki matrisler grubuna izomorftur.

$\mathbb{R}^n$ vektör uzayında öteleme grubu,

$$T = \{f(a) : a \in \mathbb{R}^n\}\ ,\quad f(a) : x \mapsto x' = x + a$$

şeklinde tanımlanır.

n boyutlu Öklid uzayı E^n, Öklid metriğine sahip bir $\mathbb{R}^n$ uzayıdır. Afin grubu $E(n)$, Öklid grubu olarak da bilinir ve

$$E(n) = \{g(A,a) : A \in O(n),\ a \in \mathbb{R}^n\} = O(n) \times T(n)$$

şeklinde tanımlanır. Dönüşüm $g(A,a) : x \mapsto x' = Ax + a$ ve boyutu da $\dim(E(n)) = \frac{n(n+1)}{2}$ ile verilir. $E(n)$ grubu E^n uzayının simetri grubudur.

$ISO(n) = SE(n)$ grubu, $\begin{pmatrix} w & x \\ 0 & 1 \end{pmatrix}$, $w \in SO(n)$ formundaki matrisler grubudur.

Homojen gruplar dönme ve yansıma dönüşümlerini içerirken homojen olmayan gruplar ayrıca öteleme dönüşümünü de içerir. Yani homojen olmayan gruplar homojen gruplara göre daha zordur. Önceki bölümde homojen grupların cebirlerinden söz etmiştik. Benzer şekilde homojen olmayan Lie gruplarının da cebirlerini ifade edebiliriz. Örneğin , $IU(n)$ ve $ISO(n)$ homojen olmayan Lie grupları ve cebirleri

$$IU(n) = \left\{\begin{pmatrix} u & a \\ 0 & 1 \end{pmatrix} : u \in U(n),\ a \in \mathbb{C}^n\right\},\ ISO(n) = \left\{\begin{pmatrix} u & a \\ 0 & 1 \end{pmatrix} : u \in SO(n),\ a \in \mathbb{R}^n\right\}$$
$$iu(n) = \left\{\begin{pmatrix} X & x \\ 0 & 0 \end{pmatrix} : X \in u(n),\ x \in \mathbb{C}^n\right\},\ iso(n) = \left\{\begin{pmatrix} X & x \\ 0 & 0 \end{pmatrix} : X \in so(n),\ x \in \mathbb{R}^n\right\}$$

formunda ifade edilebilir [7].

2. SE(2) LİE GRUBU

2×2 tipindeki reel değerli ortogonal matrislerin kümesi, bilinen matris çarpımı işlemine göre ortogonal grup oluşturur ve bu grup

$$O(2,\mathbb{R}) = \{A \in GL(2,\mathbb{R}) \mid detA = \pm 1\}$$

şeklinde ifade edilir. Determinantı bir olan matrislerin kümesi de özel ortogonal grup oluşturur ve bu grup

$$SO(2,\mathbb{R}) = \{A \in O(2,\mathbb{R}) \mid detA = 1\} \ , \ SO(2,\mathbb{R}) \subset O(2,\mathbb{R})$$

olarak ifade edilir.

$\mathbb{R}^2$ vektör uzayında $f: x \to x' = x + a$ dönüşümleri grup oluşturur ve bu grup $T(2) = \{f: a \in \mathbb{R}^2\}$ şeklinde tanımlanır [4,5,8].

Öklid uzayında, noktalar arasında mesafeyi koruyan ve düzlemin yönünü değiştirmeyen dönüşümlere düzlemin hareketleri denir. Bu hareketlere örnek olarak düzlemin paralel kayması ve bir nokta etrafındaki dönmesi verilebilir. Düzlemin tüm bu hareketlerinin kümesi bir grup oluşturur ve bu grup Öklid uzayının simetri grubudur. Başka sözle, $g(A,a): x \to x' = Ax + a$ formundaki dönüşümlerin kümesidir. Burada A ortogonal dönme matrisi ve a da öteleme vektörüdür. Bu dönüşümlerin simetri grubu

$$SE(2) = ISO(2) = \{g(A,a) \mid A \in SO(2) \ , \ a \in \mathbb{R}^2\} = SO(2) \times T(2)$$

şeklinde ifade edilir ve iki boyutlu özel Öklid dönüşümler grubu olarak adlandırılır. Bu grup aynı zamanda homojen olmayan Lie grubu olarak da belirtilir. $SE(2)$ özel Öklid Lie grubu, $SO(2)$ dönme grubu ile $T(2)$ öteleme grubunun yarı direkt çarpımıdır. Bu grup, $\mathbb{R}^2$'de mesafeyi ve yönü korur. Ayrıca bir dönme ve bir ötelemeden oluşan böyle bir kombinasyona katı hareket denir ve $x' = Ax + a$ dönüşümüyle verilir. Mühendislik, fizik, geometri ve bunun gibi alanlardaki önemli kontrol sistemleri doğal olarak bu gruplarla çalışılır.

$x' = Ax + a$ dönüşümünü daha açık olarak

$$x' = x\cos\theta - y\sin\theta + a_1 \ , \ y' = x\sin\theta + y\cos\theta + a_2$$

veya matris gösterimiyle

$$\begin{pmatrix} x' \\ y' \end{pmatrix} = \begin{pmatrix} cos\theta & -sin\theta \\ sin\theta & cos\theta \end{pmatrix} \begin{pmatrix} x \\ y \end{pmatrix} + \begin{pmatrix} a_1 \\ a_2 \end{pmatrix}$$

şeklinde yazabiliriz. Grubun (θ, a_1, a_2) gibi üç bağımsız parametresi vardır, yani boyutu üçtür, $k = \frac{n(n+1)}{2} = \frac{2\cdot 3}{2} = 3$.

$SE(2)$ grubu, ilk bakışta bir matris grubu olarak tanımlanmasa da $x' = Ax + a$ dönüşümü 3×3 tipinde matrislerle verilebilir. $x' = Ax + a$ dönüşümünü matris formunda

$$\begin{pmatrix} x' \\ 1 \end{pmatrix} = \begin{pmatrix} A & a \\ 0 & 1 \end{pmatrix} \begin{pmatrix} x \\ 1 \end{pmatrix} = \begin{pmatrix} Ax + a \\ 1 \end{pmatrix}$$

şeklinde de yazılabilir. Böylece $SE(2)$ gurubunu küme formunda

$$SE(2) = ISO(2) = \left\{ \begin{pmatrix} A & a \\ 0 & 1 \end{pmatrix} \mid A \in SO(2) \ , \ a \in \mathbb{R}^2 \right\}$$

olarak ifade edebiliriz. Yani her bir katı hareket $\begin{pmatrix} A & a \\ 0 & 1 \end{pmatrix}$ formunda 3×3 tipinde matrisle temsil edilebilir. Bu durumda $SE(2)$ grubunun bir g elemanı

$$g(\theta,a) = \begin{pmatrix} cos\theta & -sin\theta & a_1 \\ sin\theta & cos\theta & a_2 \\ 0 & 0 & 1 \end{pmatrix} \in SE(2) \quad , \quad 0 \le \theta < 2\pi,$$
$$a = (a_1, a_2)^T \in \mathbb{R}^2 \ , \ a_1, a_2 \in \mathbb{R}$$

olarak verilir.

Şimdi de grubun cebirini ifade edelim. $SE(2)$ grubunun biriminde tanjant (teğet) uzayı bulmak için $h: t \to \begin{pmatrix} A(t) & a(t) \\ 0 & 1 \end{pmatrix}$ dönüşümünü ele alalım. Bu t parametresine bağlı $SE(2)$ grubunda bir

eğridir. Bu matrisin $t = 0$ da türevini alırsak $\begin{pmatrix} B & b \\ 0 & 0 \end{pmatrix}$ formunda olur. Burada B, 2×2 tipinde anti simetrik bir matris ve b de 2 bileşenli bir vektördür. Böylece grubun cebirini küme şeklinde

$$se(2) = iso(2) = \left\{ \begin{pmatrix} B & b \\ 0 & 0 \end{pmatrix} \mid B \in so(2,\mathbb{R}),\ b \in \mathbb{R}^2 \right\} = so(2) \times t(2)$$

olarak yazabiliriz [9-13].

3. GRUBUN SONSUZ KÜÇÜK OPERATÖRLERİ

$SE(2)$ grubunun bir parametreli alt grupları, $g_j(t)$, $j = 1,2,3$

$$g_1(t) = R(t) = \begin{pmatrix} cost & -sint & 0 \\ sint & cost & 0 \\ 0 & 0 & 1 \end{pmatrix} \qquad \text{(Dönme)}$$

$$g_2(t) = T_1(t) = \begin{pmatrix} 1 & 0 & t \\ 0 & 1 & 0 \\ 0 & 0 & 1 \end{pmatrix}, \quad g_3(t) = T_2(t) = \begin{pmatrix} 1 & 0 & 0 \\ 0 & 1 & t \\ 0 & 0 & 1 \end{pmatrix} \quad \text{(Öteleme)}$$

şeklinde verilir. Buradan teğet (tanjant) matrisleri (üreteçlerin matris formu)

$$L = \frac{dg_1(t)}{dt}\Big|_{t=0} = \begin{pmatrix} 0 & -1 & 0 \\ 1 & 0 & 0 \\ 0 & 0 & 0 \end{pmatrix}, \qquad N_1 = \frac{dg_2(t)}{dt}\Big|_{t=0} = \begin{pmatrix} 0 & 0 & 1 \\ 0 & 0 & 0 \\ 0 & 0 & 0 \end{pmatrix}, N_2 = \frac{dg_3(t)}{dt}\Big|_{t=0} = \begin{pmatrix} 0 & 0 & 0 \\ 0 & 0 & 1 \\ 0 & 0 & 0 \end{pmatrix}$$

formunda bulabiliriz. Bu matrisler $se(2) = iso(2)$ cebirinin bazlarının matris formudur ve komütasyon bağıntılarını,

$$[N_1, N_2] = 0\ , \quad [N_2, L] = N_1\ , \quad [L, N_1] = N_2$$

sağlar.

Bu üreteçleri diferansiyel operatör formunda da yazabiliriz. Grubun bir parametreli alt gruplarına karşılık gelen üreteçler,

$$y = g_j(t)\, x\ , \quad x = (x_1, x_2, \dots, x_n)\ , \quad y = (y_1, y_2, \dots, y_n)\ , A_{jk}(x) = \frac{dy_k}{dt}\Big|_{t=0}$$

$$L_j = -\sum_{k=1}^{2} A_{jk}(x) \frac{\partial}{\partial x_k}$$

ifadesiyle bulunur. Buradan $SE(2) = ISO(2) = SO(2) \times \mathbb{R}^2$ grubunun $g_j(t)$ bir parametreli alt gruplara karşılık gelen üreteçleri sırasıyla

$$L = x_2 \frac{\partial}{\partial x_1} - x_1 \frac{\partial}{\partial x_2}\ , \quad N_1 = -\frac{\partial}{\partial x_1}\ , \quad N_2 = -\frac{\partial}{\partial x_2}$$

$x_1 \to x$, $x_2 \to y$ olarak alırsak,

$$L = y \frac{\partial}{\partial x} - x \frac{\partial}{\partial y}\ , \ N_1 = -\frac{\partial}{\partial x}\ , \ N_2 = -\frac{\partial}{\partial y}$$

formunda buluruz.

4. GRUBUN CASİMİR OPERATÖRÜ

Fiziğin ve matematiğin bazı uygulama alanlarında problemlerin belirli dönüşümler altında invaryant kalmaları, bu problemlerin çözümlerinde büyük kolaylıklar sağlar. Bu nedenle invaryant operatörler uygulamalarda büyük bir öneme sahiptir. Problemlerin çözümünde ortaya çıkan birçok diferansiyel operatör invaryant olma özelliğine sahiptir. Örneğin, Laplace operatörü

$$\Delta = \frac{\partial^2}{\partial x^2} + \frac{\partial^2}{\partial y^2} + \frac{\partial^2}{\partial z^2}$$

Öklid uzayındaki katı hareketler altında invaryant kalır [14]. Alman fizikçi Casimir'in 1931'de $so(3)$ cebirini kullanarak yaptığı invaryant operatör çalışmaları ardından Lie cebirleri için tanımlanan operatörler Casimir operatör adını almıştır.

Eğer bir C operatörü, bir $\mathfrak{g}$ Lie cebirinin tüm elemanları ile komüte oluyor; yani

$$[C, X_i] = 0 \ , \quad \forall X_i \in \mathfrak{g}$$

ise böyle operatörler invaryant ya da Casimir operatör olarak adlandırılır. Farklı mertebelerde Casimir operatörleri tanımlanabilir. Bir Lie grubunun ikinci mertebeden Casimir operatörü, sonsuz küçük operatörler yardımıyla da ifade edilebilir. g^{ab} metrik tensörün tersi, J sonsuz küçük operatör olmak üzere Casimir operatörü, $C = g^{ab} J_a J_b$ ile verilir. Önceki bölümde elde edilen üreteçlere göre $SE(2)$ grubunun kartezyen koordinatlarda Casimir operatörü

$$C = \sum_{k=1}^{2} {N_k}^2 = {N_1}^2 + {N_2}^2 = \frac{\partial^2}{\partial x^2} + \frac{\partial^2}{\partial y^2}$$

şeklinde oluşturulur. Üniter indirgenemez temsiller uzayında Casimir operatörü,

$$C = -k^2 I, \quad C + k^2 I = 0$$

şeklinde bir sabite eşittir. Burada I birim operatör, k da pozitif reel bir sabittir [4,9,15].

Bu Casimir operatörüyle

$$CF(x,y) = -k^2 F(x,y) \ , \ CF(x,y) + k^2 F(x,y) = 0$$

$$\frac{\partial^2 F}{\partial x^2} + \frac{\partial^2 F}{\partial y^2} + k^2 F(x,y) = 0 \tag{4.1}$$

denklemini oluşturalım. Burada $F(x,y)$ fonksiyonu grubun manifoldu üzerinde tanımlı analitik bir fonksiyondur. Bu denklem iki boyutlu homojen Helmholtz denklemidir [16]. Adını ünlü Alman bilim adamı Hermann von Helmholtz'tan (1821-1894) alır. Bu denklem fiziğin genel korunum yasalarından ortaya çıkar ve tek renkli dalgalar için dalga denklemi olarak bakılır. Denklem eliptik türden kısmi türevli diferansiyel denklemdir. Helmholtz denklemi; ısı, Schrödinger, telgraf veya diğer başka tür dalga denklemlerinden türetilebilir. Matematikte ise bu denklem, Laplace operatörü için bir özdeğer ve özvektör problemi olarak incelenir [17-20]. Bu denklemden $k = 0$ durumu için

$$CF(x,y) = F_{xx} + F_{yy} = 0$$

Laplace denklemi yazılabilir. Yani Laplace denklemi Helmholtz denkleminin özel bir halidir. Laplace denklemi tüm katı hareketler altında invaryant kalır.

k reel bir sabit olmak üzere

$$\frac{\partial^2 F}{\partial x^2} + \frac{\partial^2 F}{\partial y^2} + k^2 F(x,y) = 0 \tag{4.2}$$

denkleminin çözümünü bulalım. Bunun için değişkenlerine ayırma yöntemini kullanabiliriz. Denklemin $F(x,y) = A(x)B(y)$ formunda bir çözümünü arayalım. Bu durumda (4.2) kısmi türevli diferansiyel denklemi,

$$\frac{d^2 A}{dx^2} + \alpha^2 A(x) = 0 \tag{4.3}$$

$$\frac{d^2 B}{dy^2} + (k^2 - \alpha^2) B(y) = 0 \tag{4.4}$$

şeklinde iki adet adi diferansiyel denkleme indirgenir, burada α ayırma sabitidir. Bu denklemlerin ayrı ayrı çözümlerini bulalım.

(4.3) denklemi için $A(x) = e^{\lambda x}$ şeklinde bir çözüm arayalım. Bu durumda karakteristik denklemin kökleri $\lambda_1 = i\alpha$, $\lambda_2 = -i\alpha$ şeklinde bulunur. Buradan (4.3) denkleminin çözümü,

$$A(x) = c_1 e^{\lambda_1 x} + c_2 e^{\lambda_2 x} = c_1 e^{i\alpha x} + c_2 e^{-i\alpha x}$$

$$A(x) = c_1 \cos(\alpha x) + c_2 \sin(\alpha x) \ , \quad \alpha = 1,2, \ldots$$

olarak bulunur. Benzer şekilde (4.4) denkleminin çözümünü de

$$B(y) = c_3 e^{\lambda_1 y} + c_4 e^{\lambda_2 y} = c_3 e^{i\sqrt{k^2-\alpha^2}\,y} + c_4 e^{-i\sqrt{k^2-\alpha^2}\,y}$$

$$B(y) = c_3 \cos(\sqrt{k^2 - \alpha^2}\, y) + c_4 \sin\left(\sqrt{k^2 - \alpha^2} y\right) \ , \quad k^2 - \alpha^2 \neq 0$$

formunda bulunur. Burada, c_i'ler keyfi sabitlerdir ve sınır şartlarından belirlenebilir ($i = 1,2,3,4$). Böylece (4.2) denkleminin çözümünü, Kartezyen koordinatlarda üstel fonksiyonların çarpımı şeklinde

$$F(x,y) = A(x)\,B(y)$$
$$= [c_1 e^{i\alpha x} + c_2 e^{-i\alpha x}]\left[c_3 e^{i\sqrt{k^2-\alpha^2}y} + c_4 e^{-i\sqrt{k^2-\alpha^2}y}\right]$$

veya

$$F_k(x,y) = \sum_{j,l=1}^{2} c_{jl} A_j(x) B_l(y)$$

formunda bulabiliriz.

Casimir operatörüyle Kartezyen koordinatlarda oluşturulan (4.1) denklemi, fiziksel probleme göre polar, parabolik, eliptik gibi başka koordinatlarda da ifade edilip çözümü bulunabilir. Örneğin denklemi polar koordinatlarda ifade edelim.

$$x = r\cos\theta \;,\; y = r\sin\theta \quad , \quad r \geq 0 \,,\, 0 \leq \theta \leq 2\pi$$
$$\frac{y}{x} = \frac{r\sin\theta}{r\cos\theta} = \frac{\sin\theta}{\cos\theta} = \tan\theta \;, \quad \theta = \arctan(y/x) = tan^{-1}(y/x)$$
$$r^2 = x^2 + y^2 \quad , \quad r = \sqrt{x^2+y^2} = (x^2+y^2)^{1/2}$$

Böylece kartezyen koordinatlarda yazılan Laplace denklemini, $\frac{\partial^2 F}{\partial x^2} + \frac{\partial^2 F}{\partial y^2} = 0$

polar koordinatlarda,

$$\frac{\partial^2 F}{\partial r^2} + \frac{1}{r}\frac{\partial F}{\partial r} + \frac{1}{r^2}\frac{\partial^2 F}{\partial \theta^2} = 0 \quad , \quad F_{rr} + \frac{1}{r}F_r + \frac{1}{r^2}F_{\theta\theta} = 0$$

şeklinde ifade edilir. Grubun üreteçlerini de polar koordinatlarda ifade edersek

$$L = -\frac{\partial}{\partial\theta} \;,\; N_1 = -\cos\theta\frac{\partial}{\partial r} + \frac{\sin\theta}{r}\frac{\partial}{\partial\theta} \;,\; N_2 = -\sin\theta\frac{\partial}{\partial r} - \frac{\cos\theta}{r}\frac{\partial}{\partial\theta}$$

şeklinde olur. Böylece polar koordinatlarda Helmholtz denkleminin ifadesi

$$F_{rr} + \frac{1}{r}F_r + \frac{1}{r^2}F_{\theta\theta} + k^2 F(r,\theta) = 0 \tag{4.5}$$

formunda bulunur.

Bu denklemin değişkenlerine ayırma yöntemine göre, $F(r,\theta) = R(r)\,H(\theta)$ formunda bir çözümünü bulalım [17, 21]. Bu durumda

$$\frac{d^2H}{d\theta^2} + \alpha^2 H(\theta) = 0 \tag{4.6}$$
$$r^2\frac{d^2R}{dr^2} + r\frac{dR}{dr} + (k^2r^2 - \alpha^2)R(r) = 0 \tag{4.7}$$

denklemini elde ederiz. Benzer şekilde (4.6) denkleminin çözümü

$$H(\theta) = c_1 H_1(\theta) + c_2 H_2(\theta) = c_1 e^{i\alpha\theta} + c_2 e^{-i\alpha\theta} \quad , \quad \alpha = 0, \pm1, \pm2, \ldots$$

olarak bulunur. Burada c_1 ve c_2 keyfi sabitler, $H_1(\theta) = e^{i\alpha\theta}$, $H_2(\theta) = e^{-i\alpha\theta}$ ise denklemin lineer bağımsız çözümleridir.

(4.7) denklemi ise Bessel diferansiyel denklemidir. Denklemin çözümü Frobenius metoduyla bulunabilir. Denklemin $r = 0$ civarında bir seri çözümü vardır.

$\alpha^2 > 0$, denklemin genel çözümü,

$$R(r) = c_3 J_\alpha(kr) + c_4 J_{-\alpha}(kr) \quad , \quad \alpha \text{ tam sayı değilse}$$
$$R(r) = c_3 J_\alpha(kr) + c_4 Y_\alpha(kr) \;,\; \alpha = 0,1,2,\ldots \tag{4.8}$$

ile verilir.

$$J_\alpha(kr) = \sum_{n=0}^{\infty} \frac{(-1)^n}{n!\Gamma(n+\alpha+1)}\left(\frac{kr}{2}\right)^{2n+\alpha}$$
$$J_{-\alpha}(kr) = (-1)^\alpha J_\alpha(kr) \;,\; \alpha = 1,2,3,\ldots$$

Bessel denkleminin herhangi bir mertebeden tam çözümleri (4.8) gibi verilir. Burada $Y_\alpha(kr)$ çözümü $r = 0$ da analitik değildir. Böylece bizim esas çözümümüz $J_\alpha(kr)$ olur. Bu durumda (4.7) denkleminin çözümü

$$R(r) = c_3 J_\alpha(kr)$$

olur. Böylece, polar koordinatlarla ifade edilen (4.5) denkleminin çözümü

$$F(r,\theta) = R(r)\,H(\theta) = c_3\,J_\alpha(kr)\left[c_1 e^{i\alpha\theta} + c_2 e^{-i\alpha\theta}\right]$$

olarak bulunur [16, 22,23,24].

Kuantum mekaniğinde zamandan bağımsız iki boyutlu Schrödinger denklemi

$$-\frac{\hbar^2}{2m}\left(\frac{\partial^2\psi}{\partial x^2} + \frac{\partial^2\psi}{\partial y^2}\right) + V(x,y)\psi(x,y) = E\psi(x,y)$$

formunda verilir ve denklem eliptik türdendir. Burada,

$$H = -\frac{\hbar^2}{2m}\left(\frac{\partial^2}{\partial x^2} + \frac{\partial^2}{\partial y^2}\right) + V(x,y)$$

operatörü Hamiltonyen veya enerji operatörünü, $V(x,y)$ potansiyel enerjiyi temsil eden reel değerli bir fonksiyon, E parametresi sistemin enerjisini, $\psi(x,y)$ dalga fonksiyonunu, m parçacığın kütlesini ve $\hbar$ ise Planck sabitini ifade eder. Kuantum mekaniği üzerine yapılan ilk çalışmalardan bu yana, tam olarak çözülebilen kuantum mekaniği problemleri sayısı oldukça azdır. Bu nedenle tam bir çözüm elde etmek amacıyla birçok yaklaşım metodu geliştirilmiştir. Geliştirilen bu yöntemlerin birçoğu sistemlerin simetrileri, daha özel bir ifade ile Lie cebiri özelliklerine dayanmaktadır. Bu nedenle Lie grupları ve cebirleri teorisi bu alanda büyük bir öneme sahiptir. Bu yaklaşıma göre zamandan bağımsız Schrödinger denkleminin Hamiltonyeni ile Lie cebirinin Casimir operatörü arasında bir ilişki kurulur. Bu ilişki

$$\begin{aligned} H\psi(x,y) &= [-C + V(x,y)]\,\psi(x,y) \\ &= [-\Delta_{LB} + V(x,y)]\,\psi(x,y) = E\psi(x,y) \quad , \quad (\hbar = 2m = 1) \end{aligned}$$

ile verilir [25,26]. Birçok Casimir operatörü oluşturulabilir ancak bunlardan sadece bir tanesi Δ_{LB} Laplace-Beltrami operatörüne eşdeğerdir. Casimir operatörü daha yüksek mertebeden olabilir fakat Laplace-Beltrami operatörü ise sadece ikinci mertebedendir [27]. Schrödinger denklemi mikroskobik boyuttaki fiziksel sistemlerin davranışları hakkında bilgi verir ve sistemin durumları bu denklemin çözümleri olan dalga fonksiyonları ile ifade edilir. Çoğu zaman Schrödinger denkleminin çözümü, belirli bir potansiyel fonksiyonuna bağlı olarak yapılır ve bu denklem kuantum teoride önemli bir yere sahiptir [28,29]. Schrödinger denklemi ile ilgili bu kısa bilgiden sonra $SE(2)$ grubuyla bağlantılı fiziksel sistem için zamandan bağımsız Schrödinger denkleminin çözümünü bulalım. Denklem Kartezyen ve polar koordinatlarda

$$\left(\frac{\partial^2}{\partial x^2} + \frac{\partial^2}{\partial y^2}\right)\psi(x,y) + \big(E - V(x,y)\big)\psi(x,y) = 0$$

$$\psi_{rr} + \frac{1}{r}\psi_r + \frac{1}{r^2}\psi_{\theta\theta} + \big(E - V(r,\theta)\big)\psi(r,\theta) = 0$$

şeklinde yazılabilir. Basit olsun diye denklemin serbest parçacık, yani $V(r,\theta) = 0$ için çözümünü bulalım. Bu durumda denklem

$$\psi_{rr} + \frac{1}{r}\psi_r + \frac{1}{r^2}\psi_{\theta\theta} + E\psi(r,\theta) = 0 \tag{4.9}$$

haline dönüşür [30,31]. (4.2) veya (4.5) denklemindeki $k^2 = E$ enerji olarak alırsak (4.9) denklemi (4.5) Helmholtz denklemine indirgenir.

$$\psi_{rr} + \frac{1}{r}\psi_r + \frac{1}{r^2}\psi_{\theta\theta} + k^2\psi(r,\theta) = 0$$

Yukarıda (4.5) denkleminin çözümünü vermiştik. Bu durumda Schrödinger denkleminin çözümü olan dalga fonksiyonu

$$\psi(r,\theta) = c_3\,J_\alpha(kr)\left[c_1 e^{i\alpha\theta} + c_2 e^{-i\alpha\theta}\right]$$

veya

$$\psi_\alpha(r,\theta) = c_1 c_3\,J_\alpha(kr)\,e^{i\alpha\theta} = c\,J_\alpha(kr)\,e^{i\alpha\theta} \quad , \quad c = c_1 c_3$$

formunda yazılabilir. Serbest bir parçacığın E enerjisinin olası değerlerinin hepsi pozitif sayılardır, yani Hamiltonyenin spektrumu $[0,\infty)$, $E > 0$ olur [32].

5. SONUÇLAR VE TARTIŞMA

Oluşturulan bir modelden ortaya çıkan denklemlerin simetri yöntemiyle çözümünün bulunması literatürde önemli bir yere sahiptir. Simetri yöntemi grup teorinin en çekici ve pratik uygulamalarından birini temsil eder. Ortaya çıkan denklemin simetri grubunun bulunması ve simetri yöntemiyle çözümünün elde edilmesi ilginç olmuştur. Özellikle fizik ve uygulamalı matematik alanlarındaki problemlerin çözümünde grup teorisi tekniği kullanımı giderek artmaktadır. $SE(2)$ özel Öklid grubu, iki boyutlu uzayda ötelemelerin ve dönmelerin kümesidir, yani iki boyutlu uzayda katı cisim dönüşümlerinin grubudur. Bu dönüşümler, fizik ve mühendislikteki birçok farklı problemdeki hareketleri tanımlamak için kullanılır. Örneğin, bu hareketler birçok farklı endüstride bulunan bir robotik kol gibi bir mekanizma tarafından yapılabilir. Basit bir kolun, dönme ve öteleme veya ikisinin bir kombinasyonunu yapabilen ve katı elemanlarla birbirine bağlanan bir dizi eklem olarak modellenebilir. Günümüzde robot teknolojisinde önemli ilerlemeler olmuştur ve bu Lie grupları robotun hareketlerini (pozisyon ve dönüş) daha düşük boyutlarda temsil etmemizi sağlar. Bu çalışmada ele alınan $SE(2)$ homojen olmayan Lie grubu hakkında bilgi verilmiştir. Daha sonra bu grubun sonsuz küçük operatörleri ve bu operatörlerle oluşturulan özdeğer ve özfonksiyon problemi ele alınıp çözümü verilmiştir. Bir fiziksel sistemin özdeğer ve özfonksiyonlarının bulunması önemli bir problemdir. Robot teknolojisi ve Kuantum mekaniği Lie gruplarının önemli uygulama alanlarındandır. Kuantum mekaniği deyince Schrödinger denklemi akla gelir. Schrödinger denklemi ile Lie grubunun Casimir operatörü arasında bir ilişki vardır. Bu ilişkiden $SE(2)$ Lie grubuyla bağlantılı fiziksel sistemin dalga fonksiyonu verilmiştir. Bu çalışmalar başka homojen olmayan Lie grupları içinde yapılabilir.

KAYNAKLAR

[1] Gilmore R., (2008), Lie groups, Physics and Geometry, Cambridge University Press
[2] Rotman J. J., (1995), In An Introduction to the Theory of Groups, Springer-Verlag New York, Inc.
[3] Wigner E. P., (1959), Group Theory and Its Application to the Quantum Mechanics of Atomic Spectra, Academic Press, Inc.
[4] Vilenkin N. J. , Klimyk A. U., (1991), Representation of Lie Groups and Special Functions, Vol. 1,2, Kluwer Academic Publishers
[5] Iachello F., (2006), Lie Algebras and Applications, Springer-Verlag, Berlin Heidelberg
[6] Murray R. M., Li Z., Sastry S. S., (2017), A Mathematical Introduction to Robotic Manipulation, CRC Press
[7] Kaneta H., (1984), The Invariant Polynomial Algebras For The Groups IU(n) and ISO(n), Nagoya Math. J., Vol. 94, 43-59
[8] Barut A. O., Raczka R., (1980), Theory of Group Representations and Applications, Polish Scientific Publishers
[9] Selig J.M., (2004), Lie Groups and Lie Algebras in Robotics, Computational Noncommutative Algebra and Applications, Kluwer Academic Publishers, 101-125
[10] Kim Y. S., Noz M. E., (1986), Theory and Applications of the Poincaré Group, D. Reidel Puhlishing Company, Dordrecht, Holland
[11] Erkuş S., (2017), *Lie Group Applications on Robotics*, Dokuz Eylül Üniversitesi
[12] Bassey U. N., Edeke, U. E., (2024), Convolution Equation and Operators on the Euclidean Motion Group, J. Nig. Soc. Phys. Sci. 6
[13] Mashtakov A., Ardentov A., Sachkov Y. L., (2016), Relation Between Euler's Elasticae and

Sub-Riemannian Geodesics on SE(2), Regular and Chaotic Dynamics, Vol. 21, No:7-8, 832-839

[14] Carinena J.F., Gallardo J.C., Ramos A., (2003), Motion on Lie Groups and Its Applications in Control Theory, Reports on Mathematical Physics, Vol. 51, 159-170

[15] Rozenblyum A. V., (1992), Representations of Lie Groups and Multidimensional Special Functions, Acta Applicandae Mathematica, 29, 171-240

[16] Miller W.,(1977), Symmetry and Separation of Variables, Addison-Wesley Publishing Co.

[17] Moon P., Spencer D. E., (1952), Separability Conditions for the Laplace and Helmholtz Equations, Journal of the Franklin Institute, Vol. 253 (6), 585-600

[18] Pogosyan G., Sissakian A., Winternitz P., (2003), Separation of Variables and Lie Algebra Contractions , Applications to special functions, arXiv preprint math-ph/0310011

[19] Kalnins E., Pogosyan G. S., Yakhno A., (2012), Separation of Variables and Contractions on Two-Dimensional Hhyperboloid, Symmetry, Integrability and Geometry: Methods and Applications, SIGMA 8, 105

[20] Audu E. E., Eteng A. A., (2025), Electromagnetic Modes in Optical Fiber Waveguides Using Nikifarov-Uvarov Method, Results in Optics, 18, 100784

[21] Rubinstein I., Rubinstein L., (1998), Partial Differential Equations in Classical Mathematical Physics, Cambridge University Press

[22] Taşeli H., Zafer A., (1997), A Fourier-Bessel Expansion for Solving Radial Schrödinger Equation in Two dimensions, International Journal of Quantum Chemistry, Vol. 61, 759-768

[23] King A.C., Billingham J., Otto S. R., (2003), Differential Equations, Cambridge University Press

[24] Han D., Kim Y. S., Son D., (1982), E(2)-Like Little Group for Massless Particles and Neutrino Polarization as a Consequence of Gauge İnvariance, Physical Review D, Vol. 26 , Num. 12, 3717

[25] Pogosyan G. S., Yakhno A., (2009), Lie-Algebra Contractions and Separation of Variables. Three-Dimensional Sphere, Physics of Atomic Nuclei, Vol., No. 5, 836-844

[26] Weidmann J., (1987), Spectral Theory of Ordinary Differential Operators, Springer-Verlag Berlin Heidelberg

[27] Helgason S., (1984), Groups and Geometric Analysis, American Mathematical Society

[28] Flügge S. (1999). Practical Quantum Mechanics, Springer-Verlag Berlin Heidelberg

[29] Landau L. D., Lifshitz E. M., (1977), Quantum Mechanics, Pergamon Press Ltd.

[30] Reid G. J., (1988), J. Phys. A: Math. Gen. 21, 353-362

[31] Newhouse P. F., McGill K. C., (2004), J. of Chemical Education , Vol. 81, No. 3

[32] Messiah A., (1961), Quantum Mechanics, Vol. 1,2, North-Holland Publishing Company, Amsterdam

Evaluation of Atomic and Electronic Cross Sections of Human Bone Tissue for Photon Interactions

Nuray Kutu[1]✉, İskender AKKURT[1] , Osman GÜNAY[2]

[1]Suleyman Demirel University, Physics Department, Isparta, Turkey
[2]Yıldız Technical University, Faculty of Electrical and Electronics Engineering, Department of Biomedical Engineering, Istanbul, Türkiye

ABSTRACT

Atomic cross section (ACS) and electronic cross section (ECS) parameters provide detailed insight into photon interaction probabilities with matter. In this study, ACS and ECS values of bone tissue were calculated using its elemental composition derived from hydroxyapatite and collagen with the Phy-X software. The variation of ACS and ECS with photon energy was analyzed across the diagnostic and therapeutic ranges.

The results reveal characteristic energy-dependent trends reflecting the underlying photon interaction mechanisms. The calculated ACS and ECS datasets are valuable for advanced radiation transport modeling, quantitative imaging studies, and the design of bone-equivalent phantoms in radiological research.

Keywords: *ACS, ECS, Bone*

✉ *Corresponding Author Email : nuraykutu@sdu.edu.tr*

1 INTRODUCTION

Accurate characterization of photon–matter interactions is fundamental to radiation physics, particularly in medical imaging, radiation dosimetry, and radiological research. Quantitative parameters such as the atomic cross section (ACS) and electronic cross section (ECS) play a crucial role in describing the probability of photon interactions with matter at the atomic and electronic levels. These parameters provide more detailed physical insight than macroscopic attenuation coefficients, especially when evaluating energy-dependent interaction mechanisms in complex biological materials.

Bone tissue represents a unique and clinically significant medium due to its heterogeneous composition, primarily consisting of mineral components such as hydroxyapatite and organic constituents including collagen. This composite structure results in photon interaction characteristics that differ substantially from those of soft tissues, particularly at diagnostic and therapeutic photon energies.

Precise determination of ACS and ECS values for bone is therefore essential for accurate radiation transport modeling, patient dose estimation, and quantitative interpretation of medical images involving skeletal structures.

The interaction of photons with bone tissue is strongly energy dependent, governed by fundamental processes such as the photoelectric effect, Compton scattering, and pair production. At lower photon energies, the photoelectric effect dominates, leading to enhanced interaction probabilities associated with the higher effective atomic number of bone minerals. As photon energy increases, Compton scattering becomes the predominant mechanism, resulting in characteristic changes in ACS and ECS behavior. Analyzing these variations provides critical insight into the microscopic interaction dynamics underlying macroscopic imaging and dosimetric outcomes.

Recent advances in computational tools have enabled efficient and accurate calculation of photon interaction parameters based on elemental composition and material density. Among these tools, the Phy-X software offers a reliable platform for determining ACS and ECS values across a broad photon energy spectrum using well-established cross-section databases. In this context, the present study aims to evaluate the energy-dependent behavior of ACS and ECS for bone tissue modeled using hydroxyapatite and collagen composition. The generated datasets are expected to contribute to advanced radiation transport simulations, quantitative imaging studies, and the development of bone-equivalent phantoms for radiological applications.

2 MATERIALS AND METHODS

In this study, bone tissue was modeled based on its fundamental mineral and organic constituents, namely hydroxyapatite and collagen. The elemental composition of bone was defined by combining the elemental weight fractions of these two components as reported in standard reference data. The resulting composite composition was used to represent human cortical bone for photon interaction calculations[1-12]. The mass density of the bone tissue was taken from literature values and implemented as an input parameter in the computational analysis.

The atomic cross section (ACS) and electronic cross section (ECS) values of bone tissue were calculated using the Phy-X software, a well-established computational platform for evaluating photon–matter interaction parameters. Phy-X computes energy-dependent cross sections based on the elemental composition and density of the material, utilizing photon interaction data derived from recognized cross-section databases.

Calculations were performed over a broad photon energy range covering both diagnostic and therapeutic applications. For each selected photon energy, Phy-X was used to obtain the total atomic cross section and total electronic cross section of the modeled bone tissue. The software automatically accounts for the contribution of individual elements and their respective interaction probabilities at different energies.

The calculated ACS and ECS values were analyzed as a function of photon energy to investigate the energy-dependent interaction behavior of bone tissue. Particular attention was given to identifying characteristic trends associated with dominant photon interaction mechanisms across different energy regions. The results were presented in graphical and tabulated forms to clearly illustrate the variation of ACS and ECS with photon energy.

Phy-X has been widely used and validated in previous radiation physics and medical physics studies, demonstrating good agreement with both experimental measurements and other established computational codes. Therefore, its application in the present work provides a reliable and efficient approach for evaluating photon interaction parameters of bone tissue.

3 RESULTS

The atomic cross section (ACS) and electronic cross section (ECS) values of bone tissue were successfully calculated using the Phy-X software over a broad photon energy range covering both diagnostic and therapeutic energies. The results demonstrate a pronounced energy dependence for both parameters, reflecting the fundamental photon interaction mechanisms governing radiation transport in bone tissue.

At low photon energies within the diagnostic range, ACS values were relatively high, indicating a strong probability of photon interaction with the constituent atoms of bone. This behavior is primarily attributed to the dominance of the photoelectric effect, which is enhanced by the presence of high-atomic-number elements in hydroxyapatite. Correspondingly, ECS values also exhibited elevated levels at low energies, reflecting increased photon interactions at the electronic level.

As photon energy increased, a systematic decrease in both ACS and ECS values was observed. In the intermediate energy region, where Compton scattering becomes the predominant interaction mechanism, the variation of ACS and ECS with energy followed a smoother trend, indicating reduced sensitivity to atomic number and increased dependence on electron density. This transition region highlights the changing interaction dynamics from atom-dominated to electron-dominated processes.

.

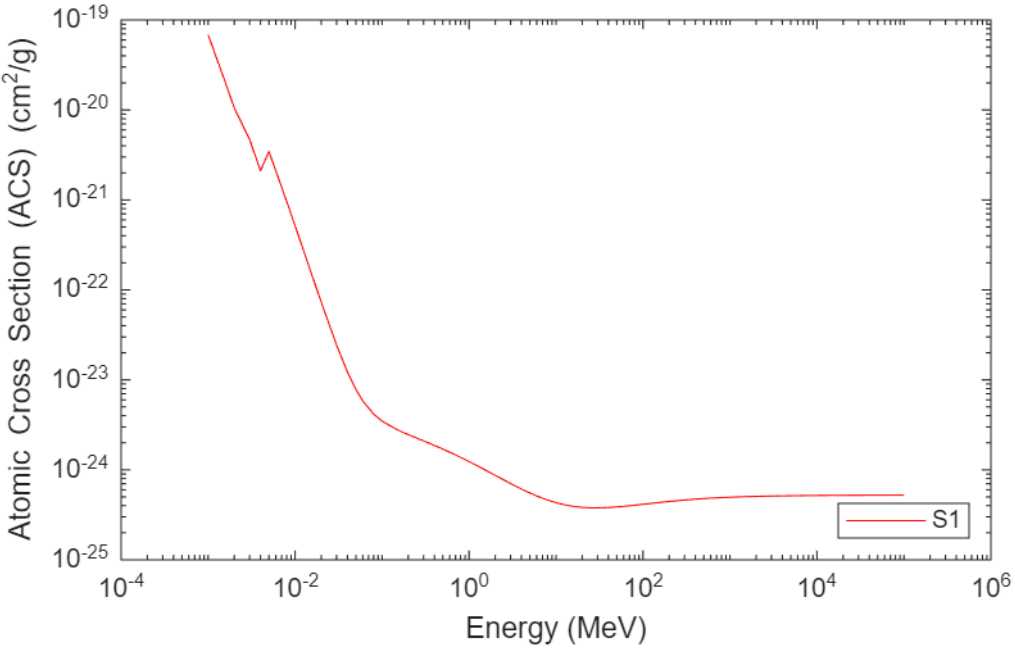

Figure 1. Atomic cross section

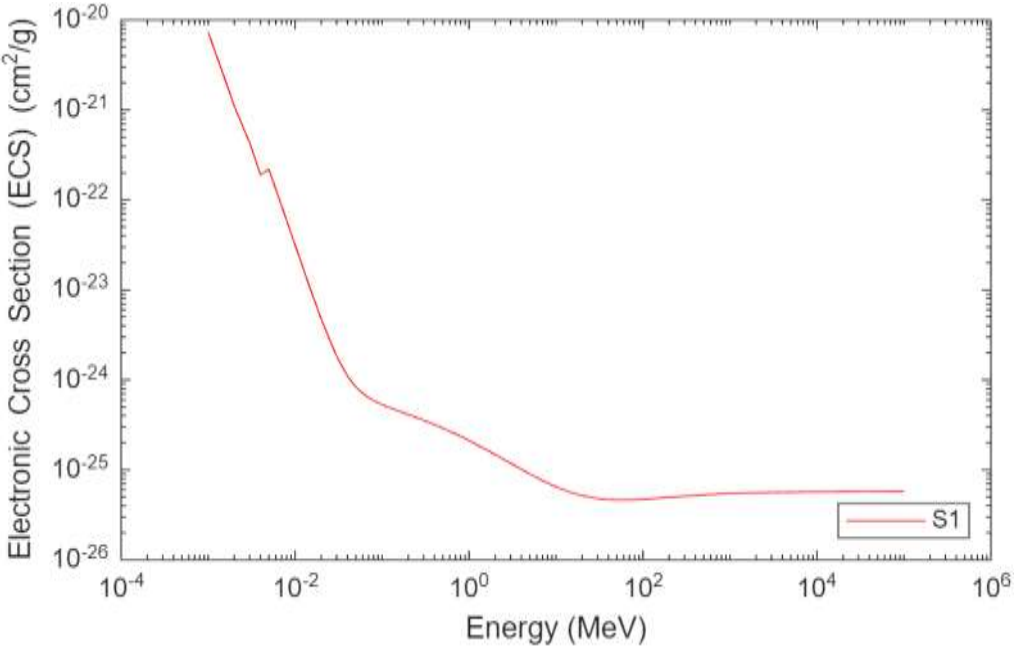

Figure 1. Electronic cross section

At higher photon energies approaching the therapeutic range, ACS and ECS values reached lower and more gradually varying levels, consistent with the increased penetrating power of high-energy photons and the reduced interaction probability per atom and per electron. The observed trends confirm the strong influence of photon energy on microscopic interaction parameters in bone tissue.

Overall, the calculated ACS (fiq 1) and ECS(fig 2) datasets provide detailed quantitative insight into the photon interaction behavior of bone across clinically relevant energy ranges. These results are directly applicable to advanced radiation transport simulations, quantitative imaging analyses, and the development of bone-equivalent phantoms for radiological and medical physics research.

4 CONCLUSION

In this study, the atomic cross section (ACS) and electronic cross section (ECS) of bone tissue were evaluated over a wide photon energy range using the Phy-X software. The results demonstrated clear energy-dependent trends, reflecting the transition between dominant photon interaction mechanisms from the diagnostic to the therapeutic energy regions.

The relatively higher ACS and ECS values at low energies highlight the significant interaction probability of bone tissue in diagnostic imaging, while the gradual decrease at higher energies indicates increased photon penetration. The generated ACS and ECS datasets provide valuable input for advanced radiation transport modeling, quantitative imaging studies, and the design of bone-equivalent phantoms in radiological research.

REFERENCE

[1] Singh, N., Singh, K.J., Singh, K., Singh, H., 2004. Comparative study of lead borate and bismuth lead borate glass systems as gamma-radiation shielding materials. Nucl. Instrum. Methods Phys. Res. Sect. B Beam Interact. Mater. Atoms 225, 305–309.

[2] Dogra M, Singh KJ, Kaur K, Anand V, Kaur P (2017) Gamma Ray Shielding and Structural Properties of Bi2O3-B2O3-Na2WO4 Glass System. Universal Journal of Physics and Application 11(5):190-195

[3] Deliormanlı AM, ALMisned G, Ene A (2023) Graphene-Bioactive Composites: Structural, Vickers Hardness, and Gamma-Ray Attanuation Characteristics. Front. Mater 10:117950

[4] Oruncak, B., 2023. Computation of neutron coefficients for B2O3 reinforced composite. Int. J. Comput. Exp. Sci. Eng. 9, 50–53.

[5] Kassab LRP, Issa SAM, Mattos GR, ALMisned, G., Bordon, C.D.S., Tekin, H.O., Gallium (III) oxide reinforced novel heavy metal oxide (HMO) glasses: a focusing study on synthesis, optical and gamma-ray shielding properties. Ceram Int 2022. https://doi.org/10.1016/j.ceramint.2022.01.314.

[6] Kheswa BV (2024) Gamma Radiation Shielding Properties of (x) Bi2O-(0.5-x)ZnO-0.2B2O3-0.3SiO2 Glass System. Nukleonika 69(1):23-29

[7] Damoom MM, Alhawsawi AM, Benoqitah E, Moustafa EB, Sallam OH, Hammad AH (2024) Simulation of Sodium Diborate Glass Containing Lead and Cadmium Oxides for Radiation Shielding Applications. JOR. 20(3):285-293

[8] Buyuk, B., Tugrul, A.B., Cengiz, M., Yucel, O., Goller, G., Sahin, F.C., 2015. Radiation shielding properties of spark plasma sintered boron carbide–aluminium composites. Acta Phys. Pol., A 128–2B, 132–134.

[9] Issa SAM, Ali AM, Susoy G, Tekin HO, Saddeek YB, Elsaman R, et al. Mechanical, physical and gamma ray shielding properties of xPbO-(50–x) MoO3–50V2O5 (25 ≤x ≤ 45 mol %) glass system. Ceram Int 2020. https://doi.org/10.1016/j. ceramint.2020.05.107.

[10] Sonia M. Reda, Hosam M. Saleh, Calculation of the gamma radiation shielding efficiency of cement-bitumen portable container using MCNPX code, Progress in Nuclear Energy, Volume 142. 104012. ISSN 2021;0149–1970. https://doi.org/ 10.1016/j.pnucene.2021.104012.

[11] Aygun M, Aygün Z (2023) A Comprehensive Analysis on Radiation Shielding Characteristics of Borogypsum (Boron Waster) by Phy-X/PSD code. Rev. Mex. Fis. 69:1-7

[12] Henaish AMA, Mostafa M, Salem B, Zakaly HMH, Issa S, Weinstein, I, Hemeda OM (2020) Spectral, Electrical, Magnetic and Radiation Shielding Studies of Mg-doped Ni–Cu–Zn Nanoferrites. Journal of Materials Science: Materials in Electronics. 22:1–13

Microcontroller-Guided DIBH Phantom: A Low-Cost Training Tool for Patient Positioning in Radiotherapy

Besnik SARAMATI[2]✉, Burim UKA[3], Fesal SELIMI[1], Behar RACI[1], Labinot KASTRATI[4]

[1]University Clinical Center of Kosova, Oncology Clinic, Prishtina-KOSOVA
[2]University of Prishtina "Hasan Prishtina", Department of Paramedical Subjects, Prishtina-KOSOVA
[3]University of Business and Technology, Department of Medical Sciences, Prishtina-KOSOVA
[4]University of Mitrovica "Isa Boletini", Department of Mechanical Engineering, Mitrovica-KOSOVA
✉ *Corresponding Author Email: besniksaramati@gmail.com*

ABSTRACT

Today, interactive phantoms are not only necessary but also indispensable. The advanced Deep Inspiratory Breath Holding (DIBH) treatment technique is now a clinically important technique in radiotherapy, which is particularly used to minimize cardiac exposure during the treatment of left-sided breast cancer. Mastering the positioning of the patient treated with DIBH is of particular importance and is a challenge in medical physics education due to the lack of practical training tools. The study presents the design and development of an interactive 3D printed phantom that realistically simulates the movement of the anatomical thoracic area during DIBH, and this by integrating with microcontroller-based sensors and actuators to reflect the dynamics of chest rise and breath hold. The phantoms interpret real-time feedback through sound sensors, servomotors, and various visual indicators, allowing students to observe and adjust the accuracy of positioning. The study reflects that the low cost of creating interactive phantoms advances the teaching of the principles of DIBH and patient positioning in radiotherapy, also demonstrating maximum student engagement, resulting in improved conceptual understanding and potential for broader application in academic-clinical settings.

Keywords: DIBH Simulation, Microcontrollers, Patient Positioning.

1.INTRODUCTİON

Deep Inspiration Breath Hold (DIBH) is a deep technique in radiotherapy for left-side breast cancers that requires patients to take and hold a deep breath for left-sided radiation delivery [1, 2]. This voluntary breath-holding expands the lungs, moving the heart further away from the chest wall and out of the radiation path, which can reduce the cardiac dose by 40–50% [3]. It should be noted that despite the low cardiac exposures, there is a tendency for long-term cardiac risk to increase, making safe and accurate radiation delivery using DBH extremely important for patient outcomes [4]. Implementing DIBH in a manner that is consistent with training students and clinicians regarding full implementation is very challenging because it relies on accurate physical imitation of the human body and continuous monitoring [5]. Current educational tools—often static phantoms or passive observation capabilities—do not provide the opportunity to capture the logic and dynamic nature of thoracic motion and the real-time nature of breath-holding [6]. The lack of affordable interactive phantoms limits hands-on experience and educational equity, especially in resource-limited settings. The need for innovative, reproducible, and cost-effective simulations impacts the enhancement of conceptual understanding and practical competence with DIBH [7, 8, 9, 10, 11]. The project in question provides a full description of the feasibility of developing and evaluating a new DIBH

phantom, integrated and driven by microcontrollers and 3D-printed combinations—a project developed by the team of the Radiotherapy and Brachytherapy Department at the Oncology Clinic in Kosovo. The interactive phantom simulates realistic chest wall movements by providing interactive feedback and enabling the idea of training based on scalable and affordable reproduction for future generations of medical physicists and beyond.

2.PROBLEM STATEMENT

In most countries around the world, including Kosovo, general or medical physics students, not to mention the laboratory exercises for medical students taking the Medical Physics course, have so far graduated with limited practical skills in DIBH procedures, because standard training relies on static models, video observation, or, in some cases, exposure to real patients during clinical treatment. This outdated approach does not provide dynamic feedback, fails to accurately represent the timing and amplitude of thoracic motion, and does not include the repetitive practice that is essential for skill acquisition. Cost-restricted access to high-end simulation equipment exacerbates the problem in countries and regions. The insurmountable obstacle for most institutions that need to improve local capacities regarding radiotherapy education related to DIBH are commercial trainings, which are costly according to our project. We reflect that the basic lack of interactive simulations becomes an obstacle to the needs for developing motor and critical skills and closing the theoretical gaps in practical ones. The fundamental goal of this project is to address these limits and obstacles through an interactive phantom for DIBH built at a local level, through integration with microcontrollers and sensor modules that are affordable for reproduction at a cost (under 100 euros). By integrating electronic feedback and anatomically realistic motion, this project aims to foster better experiential learning, accommodate repeated practice, and support wider adoption in medical physics training programs—particularly in resource-constrained environments.

3.METHODOLOGY

3.1The Interactive Phantom Design

We designed the interactive 3D phantom to replicate the realistic vertical displacement of the chest wall during a typical deep breath hold. Initially, the atomic base was designed to simulate the body of a female patient using the 3D Blender software. The central control base is an Arduino Uno microcontroller, chosen due to its affordable price and programmability via C++. A servomotor (SG90) was installed inside a sample frame with dimensions of 14x14x14 cm² before being placed on a 3D printed anatomical base, designed and engineered precisely to produce controlled rises and falls as a chest plate over the region that realistically corresponds to the left chest. The chest plate, the amplitude, and the time it takes to simulate the breath-hold pattern are programmable with maximum precision. Also integrated are LEDs (red - exhale, green - hold your breath, yellow - hold your breath for 20-40 seconds) as well as a piezo buzzer that provides auditory feedback by imitating the patient's voice, who can ask for help if they do not feel well, connected to a sound sensor to simulate the interruption of receiving radiotherapy automatically, thus recreating the sensory signals present in modern clinical environments. The project was inspired by open educational resources and research on interactive lung phantoms based on Arduino, which typically cost up to €350 [12]; however, we were able to create similar systems with a maximum budget of €100.

3.2 System Components

The prototype’s modular system included:

1. Arduino Uno microcontroller as the core controller [13].
2. Continuous rotation servomotor (SG90), delivering millimeter-scale vertical motion of the plate.

3. KY-038 Microphone sound sensor for distinguishing voluntary breath holds from passive breathing.
4. RGB LEDs and a buzzer for multimodal feedback.
5. 3D-printed base incorporating thoracic contours for anatomical realism.
6. USB/serial interface for live data capture and programming updates.

Figure 1. *System components of the 3D interactive phantom, showing the integration of the virtual model, rendering engine, sensor interface, and user interaction layer.*

Closed-loop feedback enabled the device to adjust servo activity in response to real-time input, simulating the adaptive approach used in clinical tracking technologies. All materials were sourced for less than €100, and assembly required only basic soldering, 3D printing, and microcontroller programming skills.

3.3 Prototyping, Testing, and Assembly

To refine the movements, profiles, and feedback mechanisms, we built an iterative design approach. Durability and reliability were tested on simulated breath holds of varying duration and amplitude, to mimic chest heaves. Using digital calipers, vertical displacement measurements were made to estimate latency using LED video signal tracking and activation time. Supporting further customization and modular expansion, documentation of the designed prototype, circuit diagrams, and control code with modification options are available.

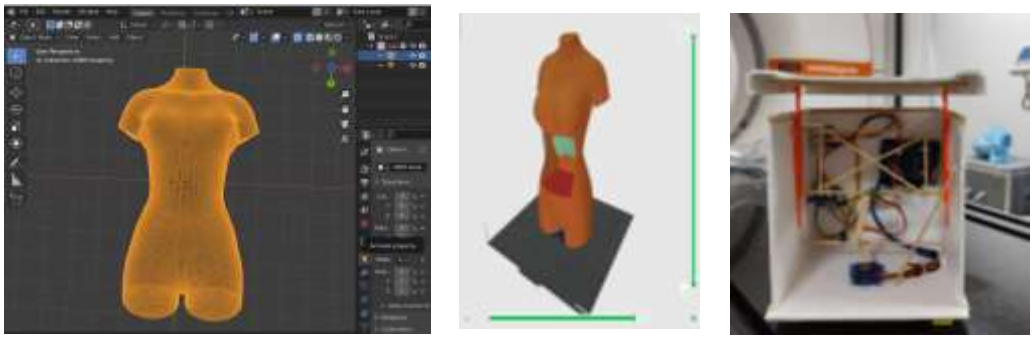

Figure 2.*The design, 3D printing, and final prototype of the phantom, illustrating the transition from digital modeling to physical fabrication*

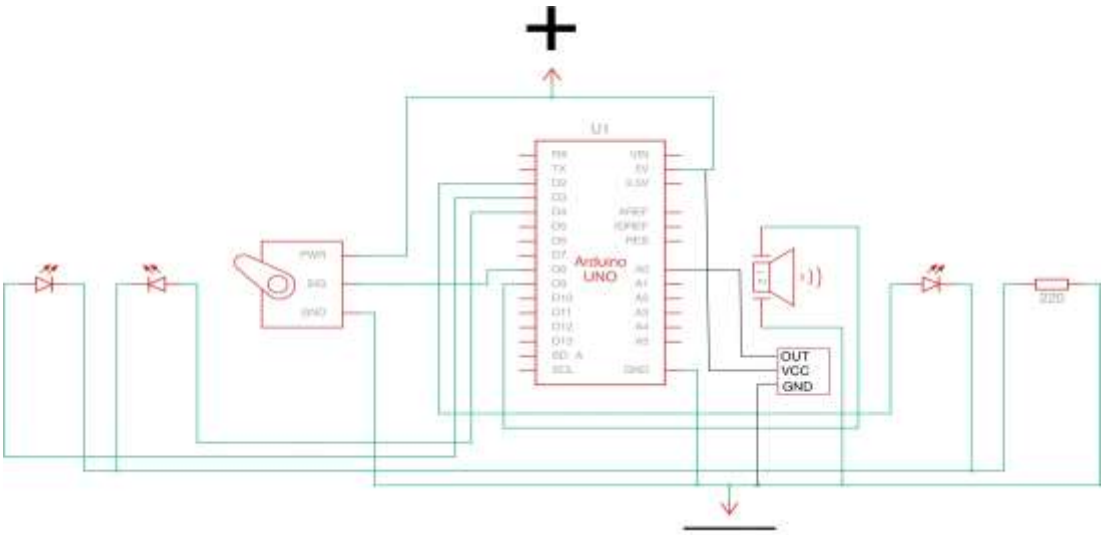

Figure 3. *Scheme of microcontroller integration and component connections generated in Fritzing, illustrating the wiring layout and system architecture.*

Table 1. *Structure of the C++ code for the phantom control system, showing the variable definitions, setup configuration, and loop-based operational logic.*

Includes & Variables	Setup Function	Loop Function
#include <Servo.h> Servo myServo; int servoPin = 8; int ledInhale = 2; int ledExhale = 3; int ledHold = 4; int buzzerPin = 9; const int HOLD_TIME = 5000; const int STEP_DELAY = 55; const int BUZZ_INTERVAL = 18000; const int BUZZ_DURATION = 200;	void setup() { myServo.attach(servoPin); pinMode(ledInhale, OUTPUT); pinMode(ledExhale, OUTPUT); pinMode(ledHold, OUTPUT); pinMode(buzzerPin, OUTPUT); digitalWrite(ledInhale, LOW); digitalWrite(ledExhale, LOW); digitalWrite(ledHold, LOW); Serial.begin(9600); delay(500); }	void loop() { Serial.print("Starting Inhale\n"); digitalWrite(ledInhale, HIGH); for (int pos = 0; pos <= 90; pos += 5) { myServo.write(pos); delay(STEP_DELAY); } digitalWrite(ledInhale, LOW); Serial.print("Inhale Complete\n"); Serial.print("Starting Hold (5s)\n"); digitalWrite(ledHold, HIGH); unsigned long holdStart = millis(); while (millis() - holdStart < HOLD_TIME) { tone(buzzerPin, 1000, BUZZ_DURATION); delay(BUZZ_INTERVAL); } digitalWrite(ledHold, LOW); Serial.print("Hold Complete\n"); Serial.print("Starting Exhale\n"); digitalWrite(ledExhale, HIGH); for (int pos = 90; pos >= 0; pos -= 5) { myServo.write(pos); delay(STEP_DELAY); } digitalWrite(ledExhale, LOW); Serial.print("Exhale Complete\n"); delay(2000); }

4.RESULTS

4.1 Performance and Reliability

The prototype of the interactive phantom reliably reproduced the movements that mimic the chest wall with a constant latency of less than 0.5 seconds and a high vertical displacement precision of ±2 mm, thus providing the required accurate simulation of mimicking human breathing patterns, essential for radiotherapy training and medical physics education. The achieved performance was realized through a calibrated SG90 servomotor, controlled by an Arduino Uno, moving a 3D printed plate along a smooth linear track with minimal mechanical feedback. Real-time visual feedback was provided by LEDs - green for correct inhalation/exhalation phases, closely mimicking the alarms used in commercial patient monitoring systems such as the Varian RPM or VisionRT.

The prototype, or rather the affordable price, offers a key advantage: the total cost of realization (less than 100€, including Arduino Uno 18€, Servomotor SG90 5€, LED 3€, Buzzer 3€, Ky-038 10€, and printed parts for anatomical base 1.5 kg–2.5 kg filament 40-60€) this offer is much smaller compared to commercial breathing movement imitation phantoms (1,000€–10,000€), enabling a wide use in institutions with limited resources, especially in developing countries or educational settings. Under full control we performed over 50 cycles of repeated testing simulating full breathing sessions, thus confirming the repeatability and stability in training or classroom conditions, without any measurable change in displacement or time even after prolonged operation. We emphasize that in the output of the serial monitor, we recorded the timed phases for post-session analysis, this is a feature towards refinement and usability, while the modular design allowed it to be easily reconfigured for other different breathing patterns. Testing with students, residents, and young medical physicists demonstrated intuitive operation and high engagement, thus reinforcing the conceptual understanding of breathing control and the importance of DIBH. In the near future, wireless control via ESP32 or various force sensors for closed-loop feedback may be included, thus further narrowing the gap between low-cost solutions and clinical-grade tools. The provided prototype serves as a scalable and open-source platform for practical training in radiation oncology and medical physics education.

5.DİSCUSSİON

The success of the microcontroller-guided DIBH phantom supports several important points for medical physics education and global health equity, drawing from key studies on DIBH in breast cancer radiotherapy [14, 15, 16]. The phantom precisely simulates chest motion with servo precision, allowing trainees to practice gaiting without the need for advanced equipment. For example, the phantom simulates chest motion with servo precision, allowing trainees to practice gating without high-end equipment. Studies on the role and importance of DIBH and its management demonstrate that by reducing the target boundaries by 5-10 mm and noting the obstacles encountered by small and medium-sized sites on the required training, the Arduino microprocessor-controlled interactive phantom is affordable to address this requirement without a hindrance for them, enabling practical sessions regarding the reduction of cardiac exposure dose. Real-time implementation is essential because for learning combined and complex tasks such as patient positioning through breath holding, involving increased accuracy and confidence is ideal. Components such as LEDs and buzzers provide real-time signals, let's say instantaneous, which closely mimic the chest monitoring models with DIBH, achieving accuracy <2 mm. Demonstration of the ExacTrac phantom for breast DIBH reflects a setup time of less than 5 minutes with feedback, thus improving reproducibility and reducing LAD dose by 30-50% [17]. Open-source phantom designs encourage adaptation and customization for generalization to different training contexts, thus making them ideal for development in resource-limited environments. Programming the phantom allows for

model adjustments (e.g., irregular breathing), consistent with previous studies on SGRT where DIBH stability demonstrated that cardiac dose was reduced by more than 40% compared to tangential fields. In Iran, it was estimated that through the implementation of SGRT DIBH, lung exposure dose was reduced by more than 25%, thus highlighting the potential of low-cost tools for equivalence in suggested training [18,19]. The integration of LED lights, sound features, and a 3D anatomical base enables the approximation of the constructivist theory of experiential learning with a maximum tendency to preserve and transfer the acquired skills. All this unique and multisensory approach reflects on the findings of CBCT, improving the quality of images by 20% in DIBH of the lungs. Finally, we emphasize that the combined DIBH+SGRT+CBCT significantly reduces the doses of OARs by 15-35%, relying on interactive phantoms through theory-practice integration. Equally important, the DIY approach allows for rapid updates and expansions—potentially integrating with commercial systems (e.g., C-Rad optical tracking) or simulating more advanced clinical scenarios in the future. Cardiac benefit reviews indicate a 50% reduction in dosage, highlighting the importance of accessible training resources. Coaching reduces DIBH setup time by 20%, highlighting the importance of feedback; the use of phantoms may facilitate standardization. There is a continued necessity for multi-institutional studies that assess the transfer of training to patient care and the wider dissemination of curricular materials. Research indicated a 95% reproducibility rate in left-breast DIBH; comparable metrics for phantoms may confirm efficacy [20]. Advocacy for accessible DIBH includes lymphoma proton therapy with a heart dose of less than 5 Gy [21]. The investigation of extended holds exceeding five minutes, along with reviews indicating a 67% reduction in cardiac exposure, supports the global implementation of this tool [22]. Stability assessments and automated electronic portal imaging device evaluations for deep inspiration breath hold [23, 24, 25].

6. CONCLUSİON

Our project demonstrates that 3D printed, anatomically based interactive phantoms, integrated and driven by microcontrollers with additional sensor modules, for DIBH training, are not only feasible but also affordable and highly effective, especially from a pedagogical perspective. The device offered by us provides the opportunity to fill a long-standing gap in practical radiotherapy education, with direct benefits affecting the self-confidence, competence, and engagement of students, young medical physicists, and Radiotherapy residents. Its low cost and ability to be reproduced will make advanced training available to more people around the world, especially in places where commercial vendors have not been able to reach. As 3D printing and open-source electronics continue to advance, similar systems have the potential to shake up other domains in medical and physics education. Widespread adoption and rigorous evaluation of such tools could significantly improve training quality and patient outcomes in radiotherapy and beyond.

REFERENCES

[1] Busschaert, S., Kimpe, E., Gevaert, T., De Ridder, M., & Putman, K. (2024). Deep inspiration breath hold in Left-Sided breast radiotherapy. JACC CardioOncology, 6(4), 514–525. https://doi.org/10.1016/j.jaccao.2024.04.009

[2] Stuart, S. R., Poço, J. G., Rodrigues, M. V. S., Abe, R. Y., & Carvalho, H. A. (2023). Can we predict who will benefit from the deep inspiration breath hold (DIBH) technique for breast cancer irradiation? Reports of Practical Oncology & Radiotherapy, 28(5), 582–591. https://doi.org/10.5603/rpor.96867

[3] Falco, M., Masojć, B., Macała, A., Łukowiak, M., Woźniak, P., & Malicki, J. (2021). Deep inspiration breath-holding reduces the mean heart dose in left breast cancer radiotherapy. Radiology and Oncology, 55(2), 212–220. https://doi.org/10.2478/raon-2021-0008

[4] Agha, A., Wang, X., Wang, M., Lehrer, E. J., Horn, S. R., Rosenberg, J. C., Trifiletti, D. M., Diaz, R., Louie, A. V., & Zaorsky, N. G. (2022). Long-Term risk of death from heart disease among breast cancer patients. Frontiers in Cardiovascular Medicine, 9, 784409. https://doi.org/10.3389/fcvm.2022.784409

[5] Kefeli, A. U., Diremsizoglu, U., Erdogan, S., Karabey, A. U., Konuk, A. O., Tirpanci, B., Aksu, M. G., & Sarper, E. B. (2025). Patient coaching for deep inspiration breath-holding decreases setup duration and left anterior descending artery dose for left-sided breast cancer radiotherapy. Supportive Care in Cancer, 33(5), 387. https://doi.org/10.1007/s00520-025-09446-1

[6] Bergom, C., Currey, A., Desai, N., Tai, A., & Strauss, J. B. (2018). Deep inspiration Breath Hold: Techniques and Advantages for cardiac sparing during breast cancer irradiation. Frontiers in Oncology, 8, 87. https://doi.org/10.3389/fonc.2018.00087

[7] Piruzan, E., Vosoughi, N., Mahdavi, S. R., Khalafi, L., & Mahani, H. (2021). Target motion management in breast cancer radiation therapy. Radiology and Oncology, 55(4), 393–408. https://doi.org/10.2478/raon-2021-0040

[8] Nhan, C., Chankowsky, J., Torres, C., & Boucher, L. (2021). Creating Low-Cost phantoms for needle manipulation training in interventional radiology procedures. Radiographics, 41(4), E1230–E1242. https://doi.org/10.1148/rg.2021200133

[9] Smyth LM, Knight KA, Aarons YK, Wasiak J (2015) The cardiac dose-sparing benefits of deep inspiration breath- hold in left breast irradiation: a systematic review. J Med Radiat Sci 62(1):66–73. https://doi.org/10.1002/jmrs.89

[10] Nankali, S., Hansen, R., Worm, E., Yates, E. S., Thomsen, M. S., Offersen, B., & Poulsen, P. R. (2022). Accuracy and potential improvements of surface-guided breast cancer radiotherapy in deep inspiration breath-hold with daily image-guidance. Physics in Medicine and Biology, 67(19), 195006. https://doi.org/10.1088/1361-6560/ac9109

[11] Parkes, M., De Neve, W., Vakaet, V., Heyes, G., Jackson, T., Delaney, R., Kirby, G., Green, S., Kilby, W., Cashmore, J., Ghafoor, Q., & Clutton-Brock, T. (2021). Safely achieving single prolonged breath-holds of > 5 minutes for radiotherapy in the prone, front crawl position. British Journal of Radiology, 94(1122), 20210079. https://doi.org/10.1259/bjr.20210079

[12] Körner, T., Wampl, S., Kiss, L., Oberoi, G., Unger, E., Birkfellner, W., & Schmid, A. I. (2024). A modular torso phantom featuring a pneumatic stepper and flow for MR sequence development. Frontiers in Physics, 12. https://doi.org/10.3389/fphy.2024.1369574

[13] Zlatanov, N. (2015). Arduino and Open Source Computer Hardware and Software. IEEE Computer Society. https://doi.org/10.13140/rg.2.1.1071.7849

[14] Shen, J., Zhang, K., Meng, X., Yang, B., Ma, J., Hu, K., Zhang, F., & Hou, X. (2025). Deep Inspiratory Breath-Hold Technique for Patients with Left-Sided Breast Cancer: Dosimetric Analysis, Clinical Evaluation, and Prediction. Technology in Cancer Research & Treatment, 24, 15330338251329120. https://doi.org/10.1177/15330338251329120

[15] Vasina, E. N., Greer, P., Thwaites, D., Kron, T., & Lehmann, J. (2021). A system for real-time monitoring of breath- hold via assessment of internal anatomy in tangential breast radiotherapy. Journal of Applied Clinical Medical Physics, 23(1), e13473. https://doi.org/10.1002/acm2.13473

[16] Rudat, V., Zhao, R., Wang, B., Zhang, L., & Shi, Y. (2024). Impact of deep inspiration breath hold, surface-guided radiotherapy, and daily CBCT on the organs at risk in breast cancer radiotherapy. Scientific Reports, 14(1), 27814. https://doi.org/10.1038/s41598-024-77482-8

[17] Goodall, S. K., & Rampant, P. L. (2023). Initial end-to-end testing of the ExacTrac dynamic deep inspiration breath-hold workflow using a breath-hold breast phantom. Physical and

Engineering Sciences in Medicine, 46(3), 1239–1247. https://doi.org/10.1007/s13246-023-01291-y

[18] Abdollahi, S., Yazdi, M. H. H., Mowlavi, A. A., Ceberg, S., Aznar, M. C., Tabrizi, F. V., Salek, R., Ghodsi, A., & Jamali, F. (2022). Surface-guided 3DCRT in deep-inspiration breath-hold for left-sided breast cancer radiotherapy: implementation and first clinical experience in Iran. Reports of Practical Oncology & Radiotherapy, 27(5), 881–896. https://doi.org/10.5603/rpor.a2022.0103

[19] Josipovic, M., Persson, G. F., Bangsgaard, J. P., Specht, L., & Aznar, M. C. (2016). Deep inspiration breath-hold radiotherapy for lung cancer: impact on image quality and registration uncertainty in cone beam CT image guidance. British Journal of Radiology, 89(1068), 20160544. https://doi.org/10.1259/bjr.20160544

[20] Patel, C. G., Peterson, J., Aznar, M., Tseng, Y. D., Lester, S., Pafundi, D., Flampouri, S., Mohindra, P., Parikh, R. R., Vega, R. M., Konig, L., Plastaras, J. P., Bates, J. E., Loap, P., Kirova, Y. M., Orlandi, E., Lütgendorf-Caucig, C., Ntentas, G., & Hoppe, B. (2022). Systematic review for deep inspiration breath hold in proton therapy for mediastinal lymphoma: A PTCOG Lymphoma Subcommittee report and recommendations. Radiotherapy and Oncology, 177, 21–32. https://doi.org/10.1016/j.radonc.2022.10.003

[21] Kalet AM, Cao N, Smith WP et al. (2019) Accuracy and stability of deep inspiration breath hold in gated breast radiotherapy—A comparison of two tracking and guidance systems. Physica Med 60:174–181. https://doi.org/10.1016/j.ejmp.2019.03.025

[22] Boda-Heggemann, J., Knopf, A., Simeonova-Chergou, A., Wertz, H., Stieler, F., Jahnke, A., Jahnke, L., Fleckenstein, J., Vogel, L., Arns, A., Blessing, M., Wenz, F., & Lohr, F. (2015). Deep Inspiration Breath Hold—Based Radiation Therapy: A clinical review. International Journal of Radiation Oncology*Biology*Physics, 94(3), 478–492. https://doi.org/10.1016/j.ijrobp.2015.11.049

[23] Redekopp, J., Rivest, R., Sasaki, D., Pistorius, S., & Aviles, J. E. A. (2023). Automated review of patient position in DIBH breast hybrid IMRT with EPID images. Journal of Applied Clinical Medical Physics, 24(9), e14038. https://doi.org/10.1002/acm2.14038

[24] Fassi, A., Ivaldi, G. B., De Fatis, P. T., Liotta, M., Meaglia, I., Porcu, P., Regolo, L., Riboldi, M., & Baroni, G. (2018). Target position reproducibility in left- breast irradiation with deep inspiration breath- hold using multiple optical surface control points. Journal of Applied Clinical Medical Physics, 19(4), 35–43. https://doi.org/10.1002/acm2.12321

[25] Kalet AM, Cao N, Smith WP et al. (2019) Accuracy and stability of deep inspiration breath hold in gated breast radiotherapy—A comparison of two tracking and guidance systems. Physica Med 60:174–181. https://doi.org/10.1016/j.ejmp.2019.03.025

Half Value Layer Characteristics of Bone Tissue and Their Implications for Medical Imaging

İskender AKKURT[1]✉ , Osman GÜNAY[2]

[1]Suleyman Demirel University, Physics Department, Isparta, Turkey
[2]Yıldız Technical University, Faculty of Electrical and Electronics Engineering, Department of Biomedical Engineering, Istanbul, Türkiye

ABSTRACT

The half value layer (HVL) is a practical quantity used to describe the shielding capability of materials against photon beams. In this study, HVL values of human bone tissue were calculated using its elemental composition and density in the Phy-X software for photon energies ranging from 30 keV to 1.25 MeV.

The results show that HVL increases with photon energy, reflecting the decreasing attenuation efficiency of bone at higher energies. At diagnostic energy levels, the calculated HVL values demonstrate the significant role of bone in patient dose modulation and image contrast formation. These findings provide valuable input for radiation dosimetry and the optimization of exposure conditions in diagnostic radiology.

Keywords: *Tissue, HVL,Radiation*

✉ *Corresponding Author Email : iskenderakkurt@sdu.edu.tr*

1 INTRODUCTION

In diagnostic radiology and radiation protection, understanding the interaction of photon radiation with biological tissues is essential for accurate dose estimation and optimization of imaging protocols. Among various attenuation parameters, the half value layer (HVL) is a widely used practical quantity that represents the thickness of a material required to reduce the intensity of a photon beam by 50%. HVL serves as a key indicator of shielding effectiveness and beam quality, and it is routinely employed in medical physics for both equipment characterization and patient dose assessment.

Human bone tissue plays a particularly important role in diagnostic imaging due to its relatively high effective atomic number and density compared to soft tissues. These properties result in stronger photon attenuation, especially at low and intermediate photon energies, which directly influences image contrast as well as the spatial distribution of absorbed dose within the patient.

Accurate characterization of the attenuation behavior of bone is therefore critical for realistic dosimetric modeling, especially in skeletal imaging and procedures where bony structures are located near radiosensitive organs.

The interaction mechanisms governing photon attenuation in bone—namely the photoelectric effect, Compton scattering, and pair production—exhibit strong energy dependence. At diagnostic energy ranges, the photoelectric effect dominates, leading to enhanced contrast but also increased localized dose deposition. As photon energy increases, Compton scattering becomes the prevailing interaction process, resulting in reduced attenuation efficiency and higher penetration capability. Quantifying these energy-dependent effects through HVL analysis provides valuable insight into both image formation and radiation risk.

With advances in computational tools, software-based platforms such as Phy-X enable precise calculation of radiation interaction parameters using elemental composition and physical density of materials. These tools facilitate systematic evaluation of tissue-equivalent materials across broad energy ranges without the need for extensive experimental measurements. In this context, the present study aims to calculate and analyze the HVL values of human bone tissue over a wide photon energy spectrum, with particular emphasis on diagnostic radiology energies. The findings are expected to contribute to improved radiation dosimetry, patient-specific dose modulation, and optimization of exposure conditions in medical imaging applications.

2 MATERIALS AND METHODS

Material Definition

In this study, human bone tissue was considered as the shielding material for photon radiation. The elemental composition and mass density of bone were defined based on standard reference data reported in the literature. These parameters were used as input values to accurately model the radiation attenuation characteristics of bone tissue across a wide photon energy range.

Computational Method

The half value layer (HVL) calculations were performed using the Phy-X software, a widely used computational tool for evaluating radiation interaction parameters of materials. Phy-X utilizes photon cross-section data derived from established databases to calculate attenuation coefficients and related shielding parameters based on the elemental composition and density of the material under investigation.

Photon energies ranging from 30 keV to 1.25 MeV were selected to cover both diagnostic and higher energy photon applications. For each selected energy, the linear attenuation coefficient (μ) of bone tissue was calculated using Phy-X. The HVL values were then determined according to the following relationship:

$$HVL=\ln 2/\mu$$

Data Analysis

The calculated HVL values were analyzed as a function of photon energy to assess the energy-dependent attenuation behavior of bone tissue. Particular emphasis was placed on the diagnostic energy range, where bone significantly affects both patient dose distribution and image contrast formation. The results were presented in graphical forms to clearly illustrate the variation of HVL with photon energy.

Validation and Reliability

Phy-X has been previously validated in numerous radiation shielding and medical physics studies, demonstrating good agreement with experimental data and other well-established computational codes. Therefore, its use in the present study provides a reliable and efficient approach for evaluating the HVL characteristics of human bone tissue.

3 RESULTS

The half value layer (HVL) values of human bone tissue were successfully calculated using the Phy-X software over the photon energy range of 30 keV to 1.25 MeV. The results demonstrate a clear and systematic dependence of HVL on photon energy, reflecting the underlying photon–matter interaction mechanisms in bone tissue.
At low photon energies within the diagnostic radiology range, the calculated HVL values were relatively small, indicating strong attenuation capability of bone tissue. This behavior is primarily attributed to the dominance of the photoelectric effect at low energies, which is enhanced by the relatively high effective atomic number of bone. As photon energy increased, a progressive rise in HVL values was observed, corresponding to a reduction in attenuation efficiency.

In the intermediate energy region, where Compton scattering becomes the predominant interaction mechanism, HVL values exhibited a smoother and more gradual increase with photon energy. This trend indicates increased photon penetration through bone tissue and reduced contrast contribution compared to lower energies. At higher photon energies approaching the MeV range, the HVL values reached their maximum within the investigated spectrum, consistent with the increased penetrating power of high-energy photons.

The energy-dependent variation of HVL highlights the significant role of bone tissue in modulating patient dose and influencing image contrast, particularly in diagnostic imaging applications. Lower HVL values at diagnostic energies suggest increased localized dose deposition within bone structures, which may have implications for dose assessment in skeletal imaging and procedures involving bony anatomy. Overall, the results confirm that HVL analysis provides valuable quantitative insight into the attenuation behavior of bone tissue across clinically relevant photon energy ranges.

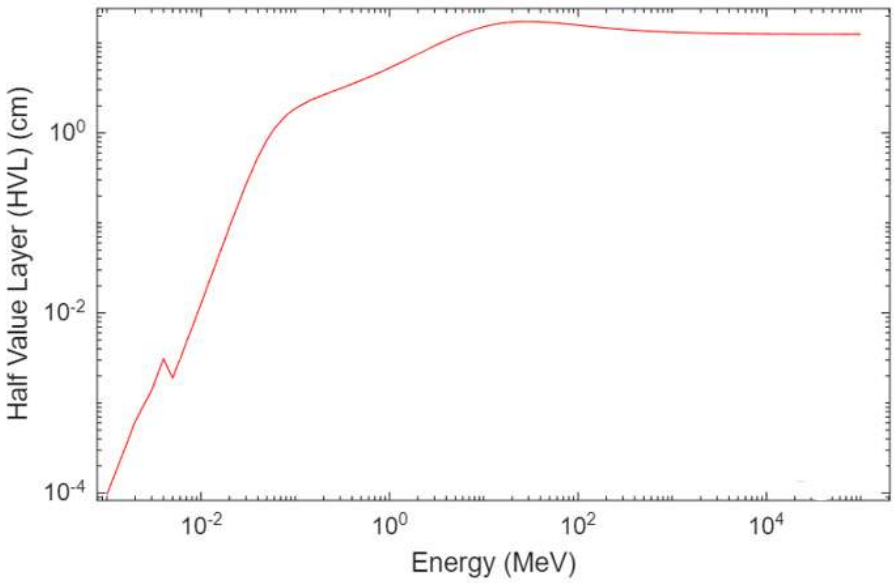

Figure 1. Affective Atomic Number

4 CONCLUSION

In this study, the half value layer (HVL) of human bone tissue was evaluated over a wide photon energy range using the Phy-X software. The results demonstrated a clear increase in HVL with increasing photon energy, indicating reduced attenuation efficiency at higher energies. At diagnostic energy levels, bone tissue exhibited strong attenuation characteristics, highlighting its important role in patient dose modulation and image contrast formation. These findings provide useful input for radiation dosimetry calculations and the optimization of exposure parameters in di radiology.

REFERENCES

[1] H.O. Tekin, Ghada ALMisned, Y.S. Rammah, Emad M. Ahmed, Fatema T. Ali, Duygu Sen Baykal, Wiam Elshami, Hesham M.H. Zakaly, Shams A.M. Issa, G. Kilic,Antoaneta Ene, Transmission factors, mechanical, and gamma ray attenuationproperties of barium-phosphate-tungsten glasses: Incorporation impact of WO3,Optik, Volume 267, 2022, 169643. doi: 10.1016/j.ijleo.2022.169643.

[2] Al Huwayz M, Albarkaty KS, Alrowaili ZA, Olarinoye IO, Elqahtani ZM, Al-Buriahi M S (2023) Gamma, neutron, and charged particle shielding performance of ABKT glass system. J. Radiat, Res. Appl. Sci. 16:100742

[3] H. O. Tekin, Fatema T. Ali, Ghada Almisned, Gulfem Susoy, Shams A. M. Issa,Antoaneta Ene, Wiam Elshami, Hesham M. H. Zakaly, Kai Xu, Multiple Assessmentson the Gamma-Ray Protection Properties of Niobium-Doped Borotellurite Glasses:A Wide Range Investigation Using Monte Carlo Simulations, Science and Technologyof Nuclear Installations, 2022. 1-17, (2022).

[4] Shams A. M. Issa, Hesham M. H. Zakaly, Ali Badawi, Reda Elsaman, H. O. Tekin, A.A. Showahy, P. S. Anjana, Devika R. Nath, N. Gopakumar, Yasser B. Saddeek, Anexperimental investigation on structural, mechanical and physical properties ofStrontium–Silicon Borate glass system through Bismuth-Aluminum substitution,Optical Materials, 117. 111124, (2021).

[5] Park, P.E., Park, J.M., Kang, J.E., Cho, J.H., Cho, S.J., Kim, J.H., Sim, W.S., Kim, Y.C., 2012. Radiation safety and education in the applicants of the final test for the expert of pain medicine. Kor. J. Pain 25, 16–21.

[6] Sakar, E., Ozpolat, O.F., Alim, B., Sayyed, M.I., Kurudirek, M., 2020. Phy-X/PSD: development of a user-friendly online software for calculation of parameters relevant to radiation shielding and dosimetry. Radiat. Phys. Chem. 166, 108496.

[7] Sariyer, D., 2020. Investigation of neutron attenuation through FeB, Fe2B and concrete. Acta Phys. Pol., A 137, 539–541.[9]Akkurt, I., Malidarre, R.B., 2021. Gamma photon-neutron attenuation parameters of marble concrete by MCNPX code. Radiat. Eff. Defect 176 (9–10), 906–918

Microcontrollers And Interactive Phantoms In Ionizing Radiation Physics And Brachytherapy Education. A Literature Review

Besnik SARAMATI[12]✉

[1]*University Clinical Center of Kosova, Oncology Clinic, Prishtina - KOSOVA*
[2]*University of Prıshtına "Hasan Prıshtına", Department of paramedical subjects, Prishtina - KOSOVA*

✉ *Corresponding Author Email: besniksaramati@gmail.com*

ABSTRACT

The review of this literature shows how the continuous development of technology through various microcontrollers occupies an extraordinary place in the creation of educational phantoms that have brought advancement in the education of ionizing radiation physics, especially in the fields of radiotherapy and brachytherapy. The fusion of these phantoms with medical physics allows us to perform detailed simulations of dose distribution, precise positioning of applicators, and the use of advanced imaging such as CT to improve treatment planning and optimization, and more. So through these practical models, students develop a more detailed and more profound understanding of the processes by acquiring concepts such as radiation attenuation and the inverse square law without forgetting the interpretation of the geometry of radioactive sources. The literature analysis indicates that using microcontroller-controlled phantoms enhances student engagement and fosters their interest in developing skills for clinical diagnostics and treatment, which in turn increases the potential for producing strong professionals capable of meeting the challenges of modern medical physics. The literature analysis shows that integrating microcontroller technology with physical modeling of phantoms and imaging is an innovative, efficient, and scalable approach for the future of education in medical physics, radiation therapy, and brachytherapy.

Keywords: Microcontrollers, Clinical education, Interactive phantom.

1.INTRODUCTİON

In the evolving nature of medical physics education, particularly in ionizing radiation physics and brachytherapy, the demand for hands-on, experiential training has reached a critical mass. Brachytherapy is an essential component of fundamental radiotherapy for tumors, such as radiation, and it concerns malignancies. It requires measured applicator positioning, dose adjustment, and gynecologic worldwide understanding of fundamentals such as radiation attenuation, the inverse square law, and gynecologic geometry. Conventional didactical methods often prove inadequate, leaving practitioners, medical students, residents, and gynecologists with abstract simulations and facing limited clinical exposure. In resource-poor settings, this discrepancy is as radiation procedures and concerns about patient safety restrict practice opportunities. Interactive phantoms are physical representations resembling human bodies that change in response to actions, connecting theory and practice. Incorporating microcontroller technology , such as cost effective, programmable circuits like Arduino or Raspberry Pi , transforms these phantoms from prior replicas into functional instruments . Microcontrollers promote engagement and actuators. development by my real time

feedback on needle insertion, tissue deformation, or Raspberry distribution through sensors and skill This literature review examines how new technologies are transforming the instruction of brachytherapy , informed by delivering reflections on needle training in radiation cancer clinics, where access to address simulators is sometimes unequal. We incorporate insights from static research , highlighting their ability to address skilled individuals equipped to contemporaneous topical challenges in Kosovo's oncology .

2.METHODOLOGY

This narrative literature review employed a organized approach to identify and assess relevant studies , enabling a focused yet worldwide synthesis. We performed a search of the Scopus and Web of Science databases from January 2010 to September 2025, with the terms "microcontroller," "interactive phantom," "brachytherapy training," "radiation physics education," "Arduino," "Raspberry Pi," and "simulation-based learning." Boolean operators (AND/OR) refine queries, as illustrated by ("phantom" AND "brachytherapy" AND ("microcontroller" OR "embedded system")). The inclusion criteria comprised peer-reviewed papers in English that presented original research or reviews on phantom-based training in ionizing radiation physics or brachytherapy, specifically detailing educational outcomes. The exclusion criteria removed non-educational studies, animal models, and studies without phantom interactivity. The preliminary screening produced 156 records. After eliminating duplicates (n=42) and doing abstract evaluations (n=89), 25 whole texts were recognized. Eight research studies were recognized as nearly relevant for the development of interactional microcontrollers in instructive settings. The quality of the acquired data focused on phantom generation, technological attributes, training effectiveness, and limitations. The quality was assessed informally based on study design and sample size, use narrative synthesis to uncover themes instead of meta-analysis due to heterogeneity. This technique, however subjective, offered nuanced insights into practical applicability, demonstrating the iterative nature of therapeutic training.

3.RESULTS

The literature reviewed highlights the field's incorporation of phantoms into interactional phantoms, converting static models into dynamic instructive tools for brachytherapy and teaching physics. Outstanding ideas came in the thriving of phantom design, scientific developments, and compatibility outcomes. Phantom designs loosely focus on the prostate and teaching brachytherapy, underscoring anatomic precision and teaching with multimodal imaging. Thaker et al. (1) illustrated a prostate phantom simulator employing ultrasound-guided dummy seed implantation, yielding consistent dosimetric results (V100 >95%) among 31 trainees, hence expediting learning curves by mimicking real-time implant heterogeneity. In the same way, Kut et al. (2) wrote about a 3D-printed, MRI-based gynecological phantom with PVC plastisol compartments that used microbead densities to make the bladder, uterus, and tumor textures look like they were echogenic. This life-sized model was used to instruct people on how to place needles into the interstitial space. Readers were able to correctly identify needles in ultrasound movies 100% of the time in transabdominal views, which proved that the model was realistic for image-guided treatments. Microcontroller integration became a key factor in making things interactive, letting phantoms act like they were changing shape or

swelling. Navarro et al. (3) developed a bio-inspired active prostate phantom including Arduino-controlled pressure sensors (NXP MPXV7002) within pneumatic arms, capable of measuring 3D stresses and deformations during needle insertion using MRI-compatible tubing. It worked with SOFA finite element simulations to reproduce clinical changes (such 15 mm translations), which helped improve dosimetry accuracy in adaptive brachytherapy training. In a similar vein, Tian et al. (4) developed the idea further with a multi-chamber pneumatic phantom controlled by Arduino-linked microblowers and sensors, which simulated asymmetric benign prostatic hyperplasia by independent volumetric control. The mistakes in forward and inverse modeling were small (3.47% and 1.41%, respectively), making it a good example for validating robots and getting feedback from trainees. More general assessments of simulators backed up similar results. Ferioli et al. (5) described 10 research on brachytherapy training tools, focusing on anthropomorphic phantoms and haptic devices that improve skill and confidence, but they didn't go into much into about microcontroller specifics. Zhou et al. (6) enhanced physical models with virtual reality (VR), utilizing HTC Vive controllers to mimic needle trajectories and dose visualization, therefore minimizing mistakes in conformance indices for rookie surgeons—this hybrid methodology is well-suited for microcontroller enhancement. In MR-guided settings, an AR system sent real-time images over Raspberry Pi to headsets, enabling transperineal catheter placement in cervix brachytherapy phantoms (7). Lastly, a dosimetry verification phantom for high-dose-rate Ir-192 brachytherapy used built-in controls to make sure the quality was good. This shows how important phantoms are for teaching how to use the inverse square law (8).

These investigations collectively indicated increased trainee engagement: mistake rates decreased by 20-40% following simulation, accompanied by a significant rise in self-reported confidence ($p<0.05$ in t-tests). Some of the problems were that it was expensive to make (around $300–$1000) and hard to scale up in places with few resources. However, open-source parts like Arduino helped to lower these obstacles.

Study	Phantom Type	Microcontroller/Tech	Key Educational Outcome
Thaker et al. (1)	**Prostate ultrasound**	**None (dummy seeds)**	**V100 >95%; consistent implants**
Kut et al. (2)	**Gynecological 3D-printed**	**None (PVC plastisol)**	**100% needle ID in US videos**
Navarro et al. (3)	**Active prostate**	**Arduino (sensors)**	**Deformation estimation <5 mm error**
Tian et al. (4)	**Multi-chamber pneumatic**	**Arduino (blowers)**	**Volumetric control ±1.41% error**
Ferioli et al. (5)	**Various simulators**	**Haptic/VR hybrids**	**Improved proficiency (narrative)**

Zhou et al. (6)	**VR-based**	**HTC Vive controllers**	**Reduced CI errors in novices**
AR-MR System (7)	**Transperineal AR**	**Raspberry Pi (streaming)**	**Real-time catheter guidance**
Dosimetry Phantom (8)	**HDR Ir-192**	**Embedded QA controls**	**Dose verification accuracy**

4.CONCLUSİON

This review emphasizes the transformative incorporation of microcontrollers and interactive simulations in the education of ionizing radiation physics and brachytherapy—an amalgamation that elucidates complex geometries and dose dynamics while engaging students through practical, interactive learning experiences. Arduino-controlled deformations that replicate edema and Raspberry Pi-facilitated augmented reality overlays provide access to high-quality training, particularly in underprivileged regions like Kosovo. Despite persistent challenges such as expenses, data reveals scalable, new strategies that yield proficient clinicians, hence enhancing patient outcomes. Future research should emphasize hybrid physical-digital phantoms and longitudinal studies to measure long-term skill retention, so ensuring the sustained efficacy of this technology beyond the simulator.

REFERENCES

[1] Thaker NG, et al. Establishing high-quality prostate brachytherapy using a phantom simulator training program. *Brachytherapy*. 2014;13(6):612-617. doi:10.1016/j.brachy.2014.05.009
[2] Kut C, et al. 3D-printed Magnetic Resonance (MR)-based gynecological phantom for image-guided brachytherapy training. *Brachytherapy*. 2022;21(5):645-654. doi:10.1016/j.brachy.2022.04.006
[3] Navarro SE, et al. A Bio-Inspired Active Prostate Phantom for Adaptive Interventions. *IEEE Trans Med Robot Bionics*. 2021;3(4):1025-1034. doi:10.1109/TMRB.2021.3119002
[4] Tian S, et al. Active Prostate Phantom with Multiple Chambers. *arXiv preprint arXiv:2508.15873*. 2025. doi:10.48550/arXiv.2508.15873
[5] Ferioli M, et al. The role of training simulators in interventional radiation therapy (brachytherapy) training: A narrative review. *J Contemp Brachytherapy*. 2023;15(4):281-290. doi:10.5114/jcb.2023.130374
[6] Zhou Z, et al. Personalized planning and training system for brachytherapy based on virtual reality. *Int J Comput Assist Radiol Surg*. 2019;14(9):1573-1582. doi:10.1007/s11548-019-02009-7
[7] Toward Augmented Reality-Driven MR-Guided Interstitial Brachytherapy. *Int J Radiat Oncol Biol Phys*. 2024;120(1):S45. doi:10.1016/j.ijrobp.2024.07.021
[8] High-Dose-Rate 192Ir Brachytherapy Dose Verification: A Phantom Study. *Int J Cancer Manag*. 2020;13(10):e108233. doi:10.5812/ijcm.108233

Determination of Half-Value and Tenth-Value Layers of PLA-Based 3D Printing Filaments under Photon Irradiation

Osman GÜNAY[1]✉

[1]*Yıldız Technical University, Faculty of Electrical and Electronics Engineering, Department of Biomedical Engineering, Istanbul, Türkiye*

ABSTRACT

Polylactic acid, one of the most widely used polymers in additive manufacturing, has recently gained attention for potential applications in radiation-related research. In this study, the half-value layer (HVL) and tenth-value layer (TVL) parameters of PLA were calculated through simulations. Photon beams at energies ranging from tens of keV to several MeV were simulated to assess attenuation behavior across different thicknesses.

Results demonstrated that both HVL and TVL increase with photon energy, reflecting the dominance of Compton scattering at higher energies. The findings highlight the importance of thickness optimization for radiation shielding applications using PLA-based materials.

Keywords: *Polylactic acid, HVL, TVL*

✉ *Corresponding Author Email : ogunay@yildiz.edu.tr*

1 INTRODUCTION

Radiation is a part of our everyday environment — it comes from natural sources like the sun, the earth, and even the food we eat. Beyond these natural origins, radiation is also widely used in medicine, industry, and research. For instance, X-rays and CT scans help diagnose diseases, while radiation therapy is used in cancer treatment. However, as beneficial as radiation can be, it also poses serious health risks if exposure is not properly controlled. Therefore, developing effective and safe shielding materials has always been a central goal in radiation protection.

Traditionally, lead has been the go-to material for radiation shielding because of its high density and effectiveness. Yet, lead is toxic, heavy, and not environmentally friendly, which limits its use in

some modern applications. This has motivated researchers to look for alternative materials that are lighter, safer, and more sustainable.

In recent years, the rise of additive manufacturing (3D printing) has opened up exciting possibilities for creating customized radiation shields with adjustable thickness and geometry. Among the polymers used in 3D printing, polylactic acid (PLA) stands out due to its biodegradability, low cost, and ease of fabrication. Although PLA is commonly used in medical and engineering applications, its potential as a radiation shielding material has only recently begun to attract attention.

To evaluate the shielding performance of PLA, one of the key approaches is to calculate parameters like the half-value layer (HVL) and tenth-value layer (TVL), which describe how effectively a material attenuates photon radiation. In this study, we investigated these parameters using simulation methods to better understand how PLA behaves under different photon energies[1-7].

2 MATERIALS AND METHODS

In this study, the radiation attenuation properties of polylactic acid (PLA) were simulated using the Phy-X software, a Monte Carlo–based simulation tool designed for radiation transport and interaction studies. The simulation setup included a monoenergetic photon source with energies ranging from tens of keV up to several MeV to cover both diagnostic and therapeutic energy ranges.

The geometry was modeled as a narrow beam setup, where the photon beam was directed perpendicularly toward PLA slabs of varying thicknesses. For each energy level, the transmitted photon intensity was recorded and used to calculate the linear attenuation coefficient (μ). From these data, the half-value layer (HVL) and tenth-value layer (TVL) were derived using the standard exponential attenuation law.

The material composition of PLA was defined according to its molecular formula ($C_3H_4O_2$) with a density of 1.24 g/cm³. Simulations were repeated for multiple photon energies to observe changes in attenuation behavior. The results were analyzed to determine how HVL and TVL values vary with increasing photon energy and to assess the relative contribution of photoelectric absorption, Compton scattering, and pair production processes.

3 RESULTS

The simulation results clearly showed that the radiation attenuation behavior of PLA changes noticeably with photon energy. As photon energy increases, the material becomes less effective at absorbing or scattering radiation, which leads to higher values of both the tenth-value layer (TVL) and the half-value layer (HVL).

Figure 1 presents the variation of the *tenth-value layer (TVL)* with photon energy. At low photon energies (below about 100 keV), the TVL values are quite small, indicating that thin PLA layers are sufficient to attenuate most of the photons. However, as the photon energy moves into the MeV

range, the TVL increases significantly. This trend is mainly due to the dominance of Compton scattering, which allows photons to penetrate deeper into the material.

Similarly, Figure 2 shows the *half-value layer (HVL)* as a function of photon energy. The behavior follows the same pattern as the TVL curve, with HVL values increasing gradually as energy rises. The increase in both parameters reflects a transition from photoelectric absorption at low energies to Compton scattering and pair production at higher energies.

Overall, the results demonstrate that the shielding effectiveness of PLA strongly depends on photon energy. While PLA provides good attenuation at lower energies, thicker layers are required when dealing with high-energy photons. These findings confirm the importance of optimizing PLA thickness when designing radiation protection components or devices.
.

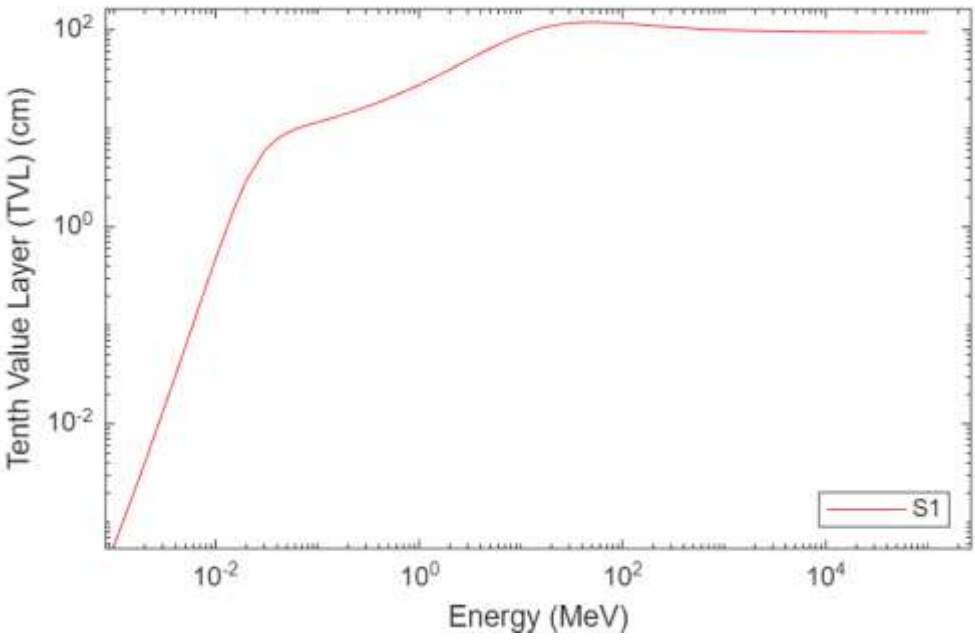

Figure 1. Tenth Value Layer

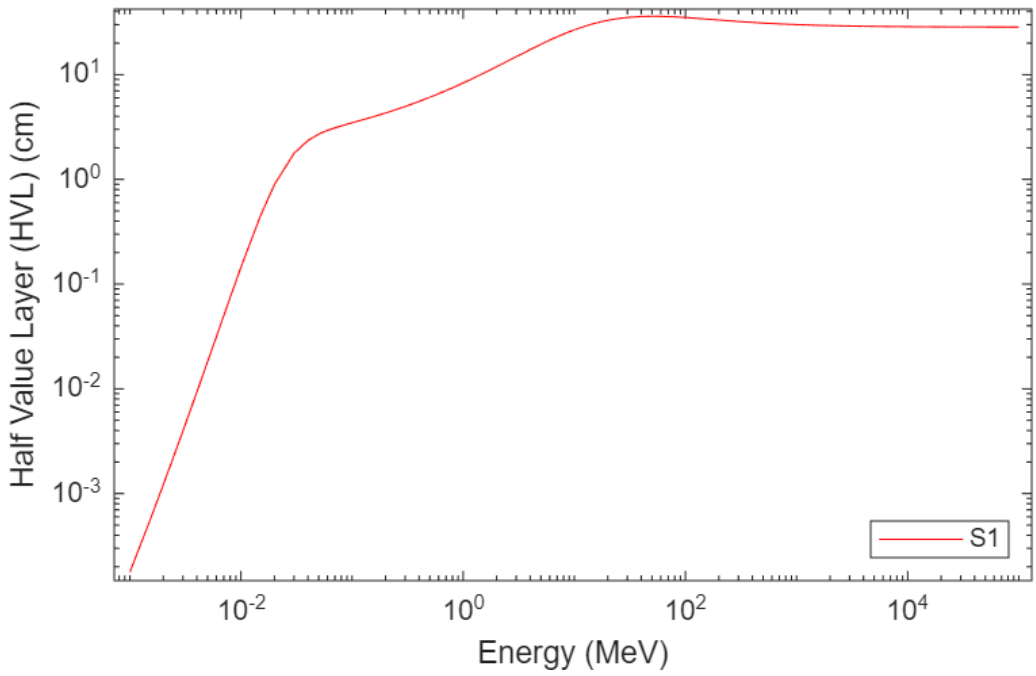

Figure 2. Half Value Layer

4 CONCLUSION

In this study, the radiation shielding properties of polylactic acid (PLA) were investigated using PYS-X Monte Carlo simulations. The half-value layer (HVL) and tenth-value layer (TVL) parameters were calculated for photon energies ranging from tens of keV to several MeV. The results revealed a clear increase in both HVL and TVL values with increasing photon energy, mainly due to the growing contribution of Compton scattering at higher energies.

These results indicate that PLA can be considered a potential candidate for lightweight and customizable radiation shielding applications, especially in situations where conventional heavy materials such as lead are impractical or undesirable. However, because PLA's attenuation efficiency decreases at higher photon energies, future studies should focus on modifying or reinforcing PLA with high atomic number additives—such as barium sulfate ($BaSO_4$) or tungsten-based compounds—to enhance its performance.

In summary, PLA offers an environmentally friendly, easy-to-shape, and cost-effective alternative for low- and medium-energy radiation shielding, provided that its thickness is properly optimized for the intended energy range.

REFERENCES

[1] Shaaban K, Alotaibi B, Alharbi N, Alrowaili Z, Al-Buriahi M, Makhlouf SA, et al. Abd El-Rehim, Physical, optical, and radiation characteristics of bioactive glasses for dental prosthetics and orthopaedic implants applications. Radiat Phys Chem 2022;193:109995. https://doi.org/10.1016/j.radphyschem.2022.109995.

[2] Shaaban KS, Al-Baradi AM, Alotaibi B, El-Rehim A. Mechanical and radiation shielding features of lithium titanophosphate glasses doped BaO. J Mater Res Technol 2023;23:756–64. https://doi.org/10.1016/j.jmrt.2023.01.062.

[3] Tekin HO, Alomairy S, Al-Buriahi MS, Rammah Y (2021) Linear/nonlinear optical parameters along with photon attenuation effectiveness of Dy

[4] Kheswa BV (2024) Gamma Radiation Shielding Properties of (x) Bi2O-(0.5-x)ZnO-0.2B2O3-0.3SiO2 Glass System. Nukleonika 69(1):23-29

[5] Damoom MM, Alhawsawi AM, Benoqitah E, Moustafa EB, Sallam OH, Hammad AH (2024) Simulation of Sodium Diborate Glass Containing Lead and Cadmium Oxides for Radiation Shielding Applications. JOR. 20(3):285-293

[6] Buyuk, B., Tugrul, A.B., Cengiz, M., Yucel, O., Goller, G., Sahin, F.C., 2015. Radiation shielding properties of spark plasma sintered boron carbide–aluminium composites. Acta Phys. Pol., A 128–2B, 132–134.

[7] Abuslroos NJ, Yaacob KA, Zainon R (2023) Radiation attenuation effectiveness of polymer-based radiation shielding materials for gamma radiation. Radiat. Phys. Chem. 212:111070

Methodological Aspects in the Commissioning of 3D Printed Vaginal Applicators for Gynecological HDR Brachytherapy

Polikron DHOQINA[1] Burim UKA[2,3]✉„ Gëzim HODOLLI[4], Behar RACI[2]

1.University of Tirana, Faculty of Natural Sciences, Tirana, Albania
[2] University for Business and Technology (UBT), Faculty of Medical Sciences, Prishtina-Republic of Kosova
[3.] University Clinical Center of Kosova, Prishtina-Republic of Kosova
[4] University of Prishtina, Faculty of Agriculture and Veterinary Medicine, Prishtina-Republic of Kosova
✉ *Corresponding Author Email: burim.uka@hotmail.com*

ABSTRACT

Abstract High-dose-rate (HDR) gynecological brachytherapy requires precise dose delivery to maximize therapeutic effect while minimizing exposure to organs at risk. Patient-specific 3D printed vaginal applicators offer the possibility of individualized treatment adaptation, but they require clear commissioning procedures and dosimetric evaluation before clinical use. This paper presents a simplified methodology for commissioning these applicators, taking into account the capabilities and conditions of hospitals in Kosovo. A key role in this process is played by medical physicists, who ensure dosimetric accuracy, measurement reproducibility, and implementation of quality assurance protocols. The integration of medical physics guarantees that 3D printed applicators can be used safely and effectively in gynecological treatment. The results aim to provide a methodological basis for the safe implementation of 3D applicators and for the standardization of practices in gynecological brachytherapy in Kosovo.

Keywords: Brachytherapy HDR, 3D printed vaginal applicators, Dosimetric evaluation, Commissioning procedures, Gynecological oncology, Kosovo, Medical Physics , Quality assurance

1.INTRODUCTION

Gynecological brachytherapy is a primary method for treating tumors, such as cervical and vaginal cancers, enabling high-dose radiation delivery directly to the tumor while preserving healthy tissues. In high-dose-rate (HDR) brachytherapy, dose accuracy depends on the applicator's shape and positioning. Standard applicators often fail to adapt to patient-specific anatomy, reducing treatment efficacy. In Kosovo, HDR brachytherapy was first implemented at the University Clinical Center of Kosovo (QKUK) in December 2021, marking a significant advancement for the country and region. 3D printing technologies enable the creation of personalized vaginal applicators, improving treatment dose and patient comfort, but require rigorous commissioning for dosimetric accuracy, biocompatibility, and reproducibility.

In resource-constrained settings like Kosovo, a simplified yet robust commissioning methodology is essential.

This study aims to develop and validate a standardized framework for commissioning patient-specific 3D printed vaginal applicators for HDR gynecological brachytherapy, tailored to Kosovo's healthcare context. Specifically, it seeks to:

- Ensure dosimetric accuracy and reproducibility for safe and effective dose delivery.
- Evaluate the material properties, mechanical integrity, and biocompatibility of 3D printed applicators under clinical conditions.

- Provide a practical workflow for hospitals with limited resources, leveraging QKUK's advancements to promote standardized gynecological oncology practices in Kosovo.

2.MATERIALS AND METHODS

Patient-specific vaginal applicators were printed using a 3D printer ensuring biocompatibility and mechanical strength. The printer was carefully calibrated, and multiple quality control checks were performed to guarantee dimensional accuracy. The printed applicator was wrapped with Gafchromic films and TLDs for dosimetric verification and then scanned in a CT simulator while placed in a mini water phantom to simulate clinical conditions. Data from the CT scan were used for calculations in the TPS (Oncentra) and Monte Carlo simulations to evaluate dose distribution were further processed and reconstructed in 3D using a custom MATLAB script, enabling quantitative analysis and visualization. Subsequently, the applicator was irradiated using the Flexitron HDR system with Iridium-192 as the source, and dose measurements were read from the Gafchromic films and TLDs to ensure safe, reproducible, and accurate dose delivery.Previous studies have demonstrated that 3D printed applicators for brachytherapy offer high agreement with dosimetric plans, with gamma analysis showing up to 99% agreement using the 2%/2 mm criterion (Nielsen et al., 2021). Furthermore, these applicators have shown high accuracy in TPS calculations, including Oncentra and Monte Carlo simulations, and are suitable for clinical use even in resource-limited settings (Sturdza et al., 2016). And the dose distributions were further processed and reconstructed in 3D using a custom MATLAB script, enabling quantitative analysis and visualization of the film data. Recent studies also report that the placement of 3D printed applicators is consistent and reproducible in water phantom and clinical simulations, demonstrating high reproducibility and conformity with clinical planning (Cunningham et al., 2025). These findings suggest that the use of 3D printed applicators can enhance treatment personalization and ensure high dosimetric accuracy in gynecological HDR brachytherapy.

Figure.1 *Experimental setup of HDR brachytherapy with a water mini-phantom, a vaginal applicator wrapped with Gafchromic film, and irradiation from Flexitron at QKUK-Prishtina*

3.RESULTS

A comparison between manual and automatic ROI selection in EBT3 film calibration showed that the automatic method, used as one of the key approaches in the self-developing film methodology in this study, provided higher reproducibility and lower variability across all dose levels. The automatic approach achieved superior correlation with the reference dose ($R^2 = 0.999$) and reduced errors (RMSE = 0.12 Gy, MAE = 0.10 Gy), confirming greater stability in dose–response calibration. This method also enabled efficient 3D dose reconstruction in MATLAB, supporting the commissioning of 3D printed vaginal applicators for gynecological HDR brachytherapy and overall quality assurance. These findings support the robustness and reproducibility of the automatic ROI approach, as previously demonstrated by Kastrati L., Uka B., Dhoqina P., et al. (2025) in their study on calibrating EBT3 films and 3D dose mapping in HDR brachytherapy.

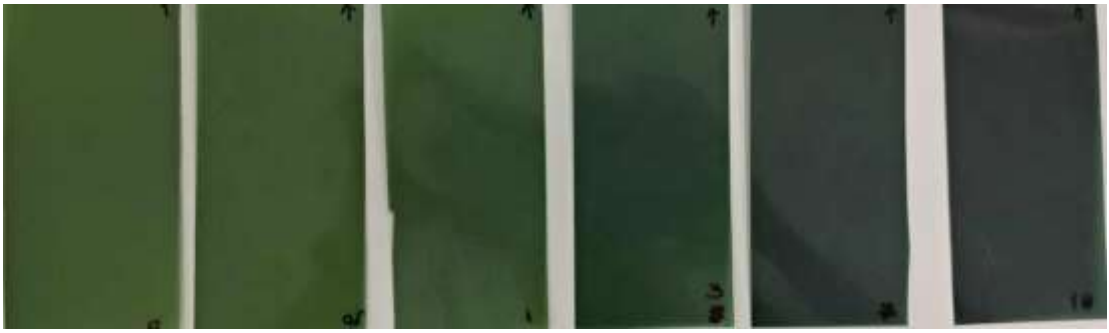

Figure.2 *EBT3 film irradiated with different doses in QKUK*

4.DISCUSSION

Based on literature results and our preliminary insights, 3D printed applicators provide high accuracy and reproducibility in placement and dose distribution, ensuring conformity with TPS plans and Monte Carlo simulations. Key advantages include personalized treatment for patients, the possibility of standardizing procedures, and compatibility with existing resources and equipment in Kosovo hospitals. However, technical challenges remain, such as material selection, printer calibration, and the need for strict QA controls. The use of phantoms and clinical simulations before implementation in real patients remains essential to ensure safety and effectiveness.

5.CONCLUSION

3D printed vaginal applicators are suitable for clinical use in HDR brachytherapy and provide high agreement with dosimetric plans. Commissioning procedures, dosimetric verification, and quality control are crucial for safe and reproducible treatment delivery. Integrating literature-based methods with local experience can help standardize practices and prepare for future clinical validation.

REFERENCES

- Biele, G., Chicheł, A., Boehlke, M., et al. (2022). 3D printing of individual skin brachytherapy applicator: design, manufacturing, and early clinical results. Journal of Contemporary Brachytherapy, 14(1), 60-70.
- Segedin, B., et al. (2023). The Use of 3D Printing Technology in Gynecological Brachytherapy. Brachytherapy, 22(2), 150-158.
- Lu, Z., et al. (2024). 3D-printed brachytherapy in patients with cervical cancer: improving efficacy and safety outcomes. International Journal of Radiation OncologyBiologyPhysics, 108(3), 500-510.
- Kastrati L., Uka B., Dhoqina P., Hodolli G., Kadiri S., Raci B., Sermaxhaj F., Guri K. & Sejdiu H. (2025) *An Automated Approach for Calibrating Gafchromic EBT3 Films and Mapping 3D Doses in HDR Brachytherapy*. Appl. Sci., 15(19), 10833. DOI:10.3390/app151910833.
- McGrath, K.M., et al. (2025). Characterization of novel 3D- printed metal shielding for brachytherapy. Medical Physics, 52(1), 45-55.
- Morgia, M., et al. (2024). Study of 3D-printed custom applicators for intracavitary high dose rate (HDR) gynaecological brachytherapy. Radiotherapy and Oncology, 180, 109-118.

Determination of Radiation Properties of New Generation Biopolymers by Monte Carlo

Aycan Şengul[1], Iskender Akkurt[2]

[1] *Akdeniz University, Vocational School of Health Services, Medical Imaging Program, Antalya, Turkey, E Mail: aycansahin@akdeniz.edu.tr*

[2] *Suleyman Demirel University, Science Faculty, Physics Department, Nucleer Sciences, Isparta-Turkey, E Mail: iskenderakkurt@sdu.edu.tr*

ABSTRACT

In this study, the radiation properties of two different polymers (P1, P2) obtained from a chitosan polymer/ginger extract/ZnO (CS/GE/ZnO) composition were calculated using a Monte Carlo simulation program. Polymers are large molecular structures created by combining simple chemical compounds. In the field of healthcare, polymers are used in many applications such as vascular prostheses, eye lenses, artificial hearts, and dental materials. Chitosan (CS) is a carbohydrate biopolymer produced by the deacetylation of naturally occurring chitin. A mono-energetic point photon source geometry was defined, directing a parallel photon beam toward the absorber material in simulations performed using the GAMOS 6.2 (Geant4-based Architecture for Medicine-Oriented Simulations) program. The mass attenuation coefficients (μ/ρ) of the polymer materials were obtained across an energy range covering a wide spectrum of doses from diagnostic to therapeutic applications in healthcare. Additionally, the simulation results were compared with calculations performed using the XCOM computer code. The findings show a high degree of congruence with theoretical data. The simulation results demonstrate that the Monte Carlo technique can be effectively used as an alternative method to calculate the mass attenuation coefficient (μ/ρ) at the desired gamma energy, which is especially valuable for biopolymer materials that are physically challenging to produce.

Keywords: photon attenuation, biomaterial, polymer, Monte Carlo simulation, GAMOS

1. INTRODUCTION

Polymers, as large molecular structures, are foundational to modern material science and have an increasing role in the health sector. The growing interest in biopolymers—polymers derived from renewable natural sources—is driven by their exceptional properties such as high biocompatibility, low density, non-toxicity, and biodegradability [1]. These features make them prime candidates for various biomedical and radiation-related applications.

Chitosan (CS), specifically, is a non-toxic, biocompatible, and biodegradable biopolymer obtained from the deacetylation of chitin. Its film-forming capacity, antimicrobial efficacy, and ability to act as a carrier for other substances are well-documented [2-5]. Recently, biopolymer composites incorporating high-Z fillers, such as zinc oxide (ZnO) nanoparticles, have been explored to enhance mechanical, barrier, and optical properties, including UV-blocking characteristics. Incorporating natural extracts like ginger extract (GE) can further enhance the biocomposite's antioxidant and bioactive properties.

In medical imaging and radiation therapy, the ability of a material to attenuate or shield ionizing radiation is a critical property. The mass attenuation coefficient (μ/ρ) is a fundamental parameter used to quantify this ability, as it is independent of the material's density [6]. For materials that are structurally complex or difficult to synthesize in an ideal form, like many novel biopolymer composites, Monte Carlo (MC) simulation offers a powerful, cost-effective alternative to physical experimentation for predicting radiation interaction parameters [7]. MC simulation codes, such as

MCNP, Geant4, and GAMOS, accurately model the stochastic processes of radiation transport through matter, providing essential data for material characterization. This study utilizes the Monte Carlo method via the GAMOS 6.2 framework to calculate the mass attenuation coefficients of two CS/GE/ZnO biopolymer composites.

2. MATERIALS AND METHODS

This study focuses on two distinct biopolymer materials, denoted as P1 and P2, both derived from a Chitosan (CS) polymer/Ginger Extract (GE)/Zinc Oxide (ZnO) composition. The specific composition and preparation methods for P1 and P2 were defined to investigate how subtle variations in the composite structure affect their radiation attenuation properties.

Table 1. *Properties of the biomaterials examined in the study*

Sample	C	N	O	Zn	K	Ni	S	Density (gr/cm^3)
P1	24.6	11.7	63	0.7				0.033
P2	45.9		53.3		0.4	0.4	0.3	0.037

The radiation properties were determined computationally using the GAMOS 6.2 simulation program. GAMOS is an object-oriented toolkit based on the widely used Geant4 platform, designed to accurately model low-energy electromagnetic interactions and particle transportation in diverse media, making it an effective tool for medical-oriented simulations.

The simulation setup involved modeling a narrow-beam geometry, which is ideal for calculating the mass attenuation coefficient. A mono-energetic point photon source was defined to emit a parallel photon beam toward the absorber material. The simulation was run for a wide range of photon energies to cover the diagnostic to therapeutic energy range relevant in healthcare.

The mass attenuation coefficient (μ/ρ) was calculated using the equation derived from the Beer-Lambert law:

$$\frac{\mu}{\rho} = \frac{1}{\rho x} ln \frac{I_0}{I}$$

where I_0 is the initial photon intensity, I is the intensity transmitted through the absorber, ρ is the density of the material, and x is the thickness of the absorber.

To validate the Monte Carlo simulation results, the mass attenuation coefficients were also determined using the standard, publicly available XCOM computer code. XCOM is a reliable tool for theoretical photon cross-section calculations for any element, compound, or mixture at energies from 1 keV to 10^5 MeV [5]. A strong agreement between the simulated (GAMOS) and theoretical (XCOM) results provides confidence in the Monte Carlo model's accuracy.

3. RESULTS AND DISCUSSION

The mass attenuation coefficients (μ/ρ) for both biopolymer composites, P1 and P2, were calculated using the GAMOS 6.2 Monte Carlo code across a broad energy spectrum and compared to the theoretical values obtained from the XCOM code. The results are presented graphically in Figure 1.

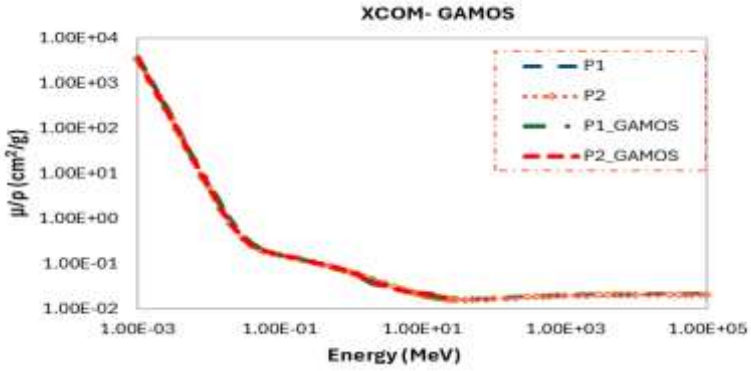

Fig. 1. *Comparison of theoretical and calculated mass attenuation coefficient as a function of gam ma energy for biopolymer.*

The results shown in Figure 1 clearly indicate an excellent correlation between the Monte Carlo simulation data (P1_GAMOS, P2_GAMOS) and the theoretical calculations (P1, P2) across the entire energy range. This strong agreement validates the geometry, material definitions, and physics models used in the GAMOS simulation for these complex biopolymer materials.
Key observations from the data include:

- High Attenuation at Low Energy: Both P1 and P2 exhibit a sharp decrease in μ/ρ at low photon energies (below ∼0.01 MeV). This high attenuation is primarily due to the photoelectric effect, whose cross-section is strongly dependent on the atomic number (Z) of the constituent elements, such as Zinc (Zn) from the ZnO component.

- Minimal Attenuation in the Compton Region: The mass attenuation coefficients flatten out in the middle energy range (∼0.1 MeV to a few MeV), which is characteristic of the Compton scattering region where the mass attenuation coefficient is less dependent on the atomic number.

- Congruence of P1 and P2: The mass attenuation curves for P1 and P2 are nearly identical throughout the entire energy spectrum. This suggests that while their compositions likely vary slightly, the overall average atomic number and electron density, which are the main factors governing attenuation, are highly similar.

The successful application of the Monte Carlo technique to predict the radiation attenuation properties of the CS/GE/ZnO biopolymers confirms its utility, especially for novel biopolymer composites that are often difficult to produce consistently or in a controlled fashion for physical measurement. This capability is crucial for the development of new materials for applications requiring precise knowledge of radiation interaction, such as polymer-based radiation shielding, dosimetric materials, or biocompatible structures used in radiation-rich environments. The potential to incorporate these biopolymers into medical devices or radiation shields highlights the importance of accurately characterizing their radiation properties.

4. CONCLUSION

The radiation properties, specifically the mass attenuation coefficients (μ/ρ), of two new generation biopolymer composites (P1 and P2) based on chitosan/ginger extract/ZnO were successfully determined using the GAMOS 6.2 Monte Carlo simulation program. The simulation results demonstrated high congruence with the theoretical data calculated by the XCOM code across a wide

energy range. This study confirms the Monte Carlo technique as a powerful and validated alternative for accurately calculating the mass attenuation coefficient of complex biopolymer materials, particularly those that are physically challenging to produce or test. Future research can leverage this methodology to optimize the composition of such biopolymers for specific applications in medical physics and radiation protection.

REFERENCES

[1] Parida, P., A. Behera, and S.C. Mishra, Classification of Biomaterials used in Medicine. 2012.

[2] Babu, S. R., Reddy, P. Y., Kumar, A. P., & Reddy, T. S. (2017). Measurement of mass stopping power of chitosan polymer using gamma radiation. Radiation Physics and Chemistry, 139, 71–76. https://doi.org/10.1016/j.radphyschem.2017.05.018

[3] More, C. V., Alsayed, Z., Badawi, M. S., Thabet, A. A. (2021). Polymeric composite materials for radiation shielding: a review. Environmental Chemistry Letters.

[4] Singh, V. P., Shirmardi, S. P., Medhat, M. E., Badiger, N. M. (2015). Determination of mass attenuation coefficient for some polymers using Monte Carlo simulation. Vacuum, 123,

[5] Mitragotri, S. and J. Lahann, Physical approaches to biomaterial design. Nature Materials, 2009. 8(1): p. 15-23.

[6] Berger, M., et al., XCOM: Photon Cross Sections Database. NIST, PML, Radiation Physics Division. 2019.

[7] Arce, P., et al. (2014). Gamos: A framework to do Geant4 simulations in different physics fields with a user-friendly interface. Nuclear Instruments and Methods in Physics Research Section A: Accelerators, Spectrometers, Detectors and Associated Equipment, 735, 304–313.

Radon Concentration Variations in the Adalar District, Istanbul

Osman GÜNAY[1]✉, Görkem SERBES[1], İsmail CANTÜRK[1], Caner YALÇIN[2], Mutlu İÇHEDEF[3], Caner TAŞKÖPRÜ[3], Murat SAÇ[3]

[1]Yildiz Technical University, Faculty of Electrical & Electronics, Biomedical Engineering, Istanbul-Türkiye
[2]Department of Physics, Kocaeli University, 41001 Izmit, Kocaeli-Türkiye
[3]Ege University Institute of Nuclear Sciences, 35100 Bornova, İzmir-Türkiye

ABSTRACT

The relationship between radon concentrations and earthquakes has been extensively investigated as radon anomalies are often considered potential precursors of seismic events. Variations in radon levels, particularly sudden increases or decreases in soil gas or groundwater, are attributed to stress accumulation and micro-fracturing processes in the Earth's crust prior to an earthquake. These fractures enhance the migration pathways of radon from deeper layers to the surface, leading to measurable anomalies. Therefore, continuous radon monitoring has become an important tool in seismological studies, aiming to better understand crustal movements and to evaluate the feasibility of radon as a short-term earthquake forecasting parameter. In this study, a continuous radon monitoring station was established in the Adalar district of Istanbul. Radon concentrations were recorded at 10-minute intervals, providing high-resolution temporal data. Along with radon, meteorological parameters such as temperature, pressure, and humidity were simultaneously measured to account for environmental influences. The variations in radon levels over a specific period were systematically observed and analyzed in order to evaluate possible correlations with both atmospheric conditions and seismic activity.

Keywords: *Radon , seismic , anomalies*

✉ *Corresponding Author Email : ogunay@yildiz.edu.tr*

1 INTRODUCTION

The Earth is composed of three distinct layers from the inside out: the core, the mantle, and the lithosphere. The thickness of each layer varies from region to region. The upper part of the mantle, located just beneath the lithosphere, is mobile due to its soft structure and the transfer of heat energy from the core through convection. These movements, combined with the effect of frictional forces, have caused large and small fractures in the lithosphere. These resulting pieces float on the mantle like rafts on the sea. Each of these pieces is called a plate.

Under normal conditions, the plates move at very slow speeds that are imperceptible to humans. The forces they exert on each other as they attempt to move can sometimes be quite significant. Over time, this force accumulates as energy between the plates. An earthquake is defined as the sudden release of this accumulated energy, causing movement within the Earth's crust. The seismic waves generated by an earthquake propagate across a wide area in various forms and under different names.

An earthquake is a phenomenon that cannot be prevented under current conditions when certain geological and geophysical circumstances arise. During an earthquake, a large amount of energy accumulated in the Earth's crust is released in a very short time. When these seismic activities occur near populated areas, they can lead to loss of life and property. Various measures are being taken to mitigate the negative impacts of earthquakes. In addition, many researchers have conducted—and continue to conduct—studies aimed at predicting the occurrence times of these unavoidable seismic events [1] . Since the process of earthquake occurrence is highly complex, predicting the timing of this complex event is an extremely difficult problem [2-5]

Temperature, pressure, and humidity measurement systems were added to the radon observation stations, and the data were continuously collected. Radon concentration, humidity, temperature, and pressure data were integrated with a computer system and were transferred online to a cloud environment, allowing remote access to the data. During the 24-month project period, radon, humidity, temperature, and pressure data were obtained simultaneously from the installed stations, while earthquake data were obtained from the Kandilli Observatory. The relationship between the collected radon, humidity, temperature, pressure, and earthquake data was modeled with 90% accuracy using a variational long–short-term memory autoencoder.

2 MATERIALS AND METHODS

The data acquisition workflow relies on continuous surveillance of radon levels and accompanying environmental parameters at a dedicated monitoring station in the Marmara Region. Within the scope of this research, not only radon concentrations but also auxiliary atmospheric indicators—namely temperature, relative humidity, and barometric pressure—are incorporated into the evaluation framework. Earthquake information is sourced from the Kandilli Observatory, where seismic records are collected independently and later synchronized with the station data through timestamp matching to ensure compatibility for time-series investigations. Time series are shown in figure 1-3.

Radon measurements are carried out using the AlphaGUARD system, positioned at the Faculty of Electrical and Electronics Engineering on Yıldız Technical University's Davutpaşa Campus. As illustrated in Fig. 1, AlphaGUARD is an active detection instrument configured to record measurements every 10 minutes and internally store the outputs. The unit functions on battery power and provides network-based data transmission capabilities.

A potential difference of 750 V DC is applied between the anode and cathode of the detector. The full chamber volume is 0.62 L, of which 0.56 L serves as the active sensing region. The system can quantify radon activity concentrations within the range of 2 Bq/m³ to 2,000,000 Bq/m³, offering a measurement precision of roughly 3% [6]. Alongside radon, the device concurrently records meteorological variables such as ambient temperature (°C), relative humidity (% rH), and atmospheric pressure (mbar); these parameters are crucial for compensating environmental influences on radon measurements [7].

Air is drawn into the detector's ionization chamber by a suction pump integrated into the measurement setup. Once inside, the radioactive decay of the Radon-222 and Radon-220 isotopes ionizes the air molecules, giving rise to electrical pulses. A continuously operating pump ensures

that the decay progeny are trapped on a dedicated filter. These pulses are then transmitted as TTL (Transistor–Transistor Logic) signals to the device's counting unit, referred to as the Counter Module. Using the detector's pre-configured calibration constants, the accompanying software interprets these raw electrical outputs and converts them into readable measurement values [8].

In this investigation, the soil-gas sampling technique is utilized (Fig. 2). This approach employs the AlphaGUARD detector together with a specialized setup consisting of a 1-meter metal insertion rod and a slender soil-gas probe. A hole is drilled to the desired depth, and the probe is positioned within this opening. Subsurface gases are subsequently drawn into the detector's ionization chamber using the AlphaPUMP system [9]. During sampling, both the gas flow rate and pumping duration can be precisely controlled through the AlphaPUMP interface. The AlphaGUARD unit records radon concentration values automatically based on the measurement interval selected by the user [10-11].

.

3 RESULTS

In this study, the influence of environmental parameters—namely atmospheric pressure, relative humidity, and temperature—on radon gas levels was examined, and the extent to which these factors could predict radon concentrations was assessed. Time periods containing measurement inconsistencies were excluded to obtain a clean dataset, after which univariate linear regression models were constructed using radon concentration as the dependent variable and each environmental parameter as the sole predictor. The predictive ability of each model was then evaluated individually.

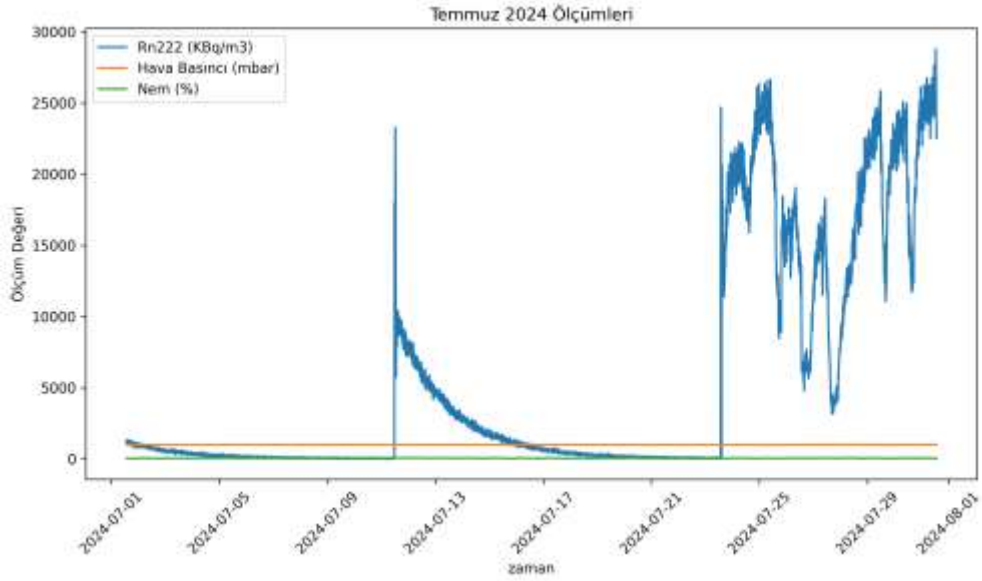

Figure 1. Time-series representation of the variations in radon concentration, humidity, and atmospheric pressure for July 2024.

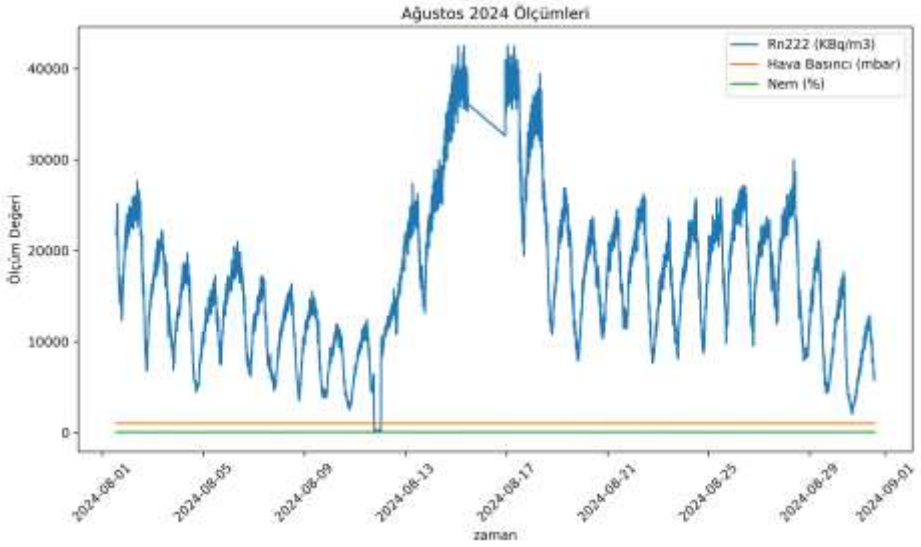

Figure 2. Time-series illustrating the variations in radon concentration, humidity, and atmospheric pressure for August 2024.

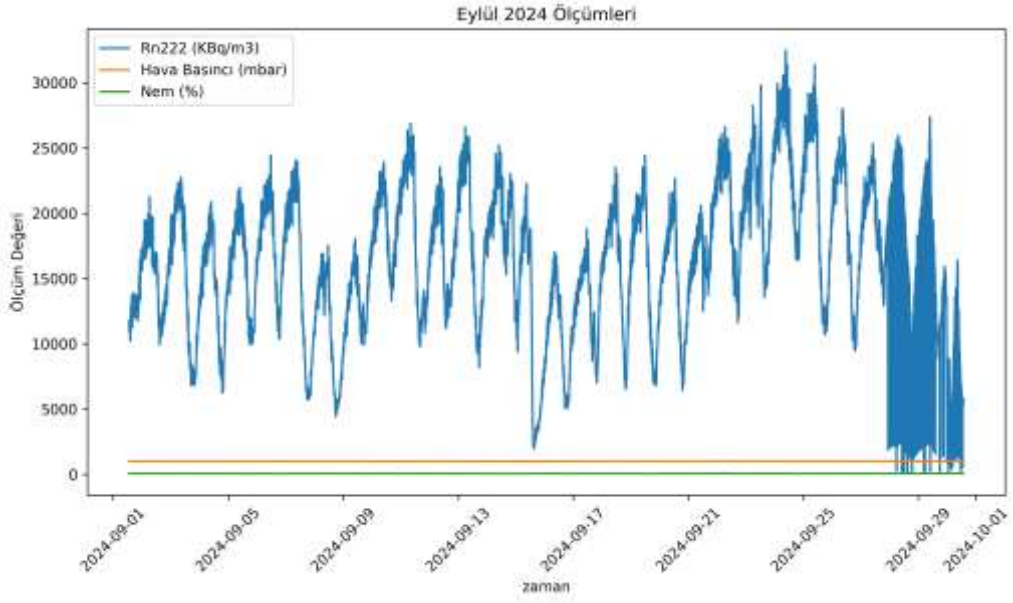

Figure 3. Time-series depicting the fluctuations in radon concentration, humidity, and atmospheric pressure for September 2024.

The dataset was partitioned into training (80%) and testing (20%) subsets. Following model training on the designated training portion, performance was assessed using the test data. For visualization, two types of plots were generated: the first illustrated the relationship between each environmental variable and both the actual and predicted radon values; the second provided a direct comparison

between predicted and observed radon concentrations (Figures 1-3). These visualizations revealed noticeable discrepancies and poor predictive alignment.
To quantitatively evaluate model accuracy, the Mean Absolute Error (MAE) metric was employed. MAE values were found to be high across all models, indicating limited predictive capability. These findings demonstrate that univariate linear regression is insufficient for reliably forecasting radon levels. The underlying relationship between radon concentration and environmental conditions appears to be nonlinear and more complex, suggesting the need for multivariate or more advanced modeling approaches.

After the inadequacy of the univariate linear models became evident, a multiple linear regression approach was implemented to determine whether radon concentrations could be predicted more accurately by considering environmental factors jointly. In this model, temperature, relative humidity, and atmospheric pressure were simultaneously incorporated as predictors. The training–testing split was carried out in the same manner as before; however, the resulting MAE value (4645.98) remained considerably high. This outcome further indicated that the relationship between radon levels and environmental variables is inherently nonlinear.

Given these limitations, the analysis moved beyond linear frameworks toward a nonlinear artificial neural network architecture—specifically, a Multi-Layer Perceptron (MLP). The MLP model consisted of three hidden layers; the first contained 64 neurons, followed by a second hidden layer with 32 neurons. The ReLU activation function was employed throughout, the Adam optimizer was used for parameter updates, and MAE served as the loss function. The network was trained for 20 epochs, during which loss values for both the training and testing subsets were recorded at each iteration.
The primary objective of this model was to capture the more intricate, nonlinear dependencies between environmental conditions and radon concentration in order to enhance predictive accuracy. The MLP framework demonstrated potential in this regard and was considered a promising advancement beyond traditional linear modeling.

4 CONCLUSION

This study investigated the complex relationship between radon gas concentrations and environmental parameters by employing both linear and nonlinear modeling approaches. Initial analyses using univariate and multivariate linear regression revealed that temperature, relative humidity, and atmospheric pressure individually and collectively failed to produce reliable predictions of radon levels. The consistently high MAE values and the visual discrepancies between predicted and observed concentrations demonstrated that radon behavior cannot be adequately captured with linear assumptions. These findings indicate that the dynamics governing radon variability are influenced by nonlinear and possibly interacting processes, rendering classical linear methods insufficient for robust forecasting.
To address these limitations, a Multi-Layer Perceptron (MLP) neural network was implemented as a nonlinear modeling alternative. With its multi-layer architecture and ability to capture complex patterns, the MLP model showed promise in learning the intricate dependencies between environmental variables and radon concentration. Although further optimization and long-term data evaluation are required, the neural network framework represents a significant improvement over linear models and offers a more suitable foundation for radon prediction studies. The results collectively highlight the necessity of advanced, nonlinear techniques in understanding radon dynamics and lay the groundwork for developing more accurate early-warning or monitoring systems in the futur

REFERENCES

[1] Geller, R.J. 1997. “Earthquake prediction: A critical review.”, Geophysical Journal International, 131(3), 425–450.

[2] Cicerone, R. D., Ebel, J.E., Britton, J. 2009. "A systematic compilation of earthquake precursors.", Tectonophysics 476(3-4), 371-396.

[3] Hayakawa, M., Hobara, Y. 2010. "Current status of seismo-electromagnetics for short-term earthquake prediction.", Geomatics, Natural Hazards and Risk, 1(2), 115-155.

[4] A., Tripathi, S.C., Mansoori, A.A., Bhawre, P., Purohit, P., Gwal, A. 2011. "Scientific efforts in the direction of successful Earthquake Prediction." International Journal of Geomatics and Geosciences, 1(4), 669-677.

[5] Shrivastava, A. 2014. "Are pre-seismic ULF electromagnetic emissions considered as a reliable diagnostics for earthquake prediction?", Current Science, 596-600.

[6] S. Liu, T. Hu, F. Lin, Z. Fan et al., “A new model to accurately measure the radon exhalation rate from soil using AlphaGUARD,” Journal of Environmental Radioactivity, vol. 266, art. no. 107226, 2023.

[7]S. Baykut, T. Akgül, S. İnan and C. Seyis, “Observation and removal of daily quasi-periodic components in soil radon data,” Radiation Measurements, vol. 45,

pp. 872–879, 2010.

[8] SARAD GmbH, “AlphaGUARD radon monitor,” [Online]. Available: https://www.sarad.de/en/products/alphaguard/. [Accessed: June 18, 2025].

[9]S. Tokonami, M. Yang and T. Sanada, “Contribution from thoron on the response of passive radon detectors,” Health Physics, vol. 80, no. 6, pp. 612–615, 2001.

[10]C. Di Carlo et al., “Thoron interference on performance of continuous radon monitors,” International Journal of Environmental Research and Public Health, vol. 19, no. 4, art. no. 2423, 2022.

[11]C. G. Sumesh, A. V. Kumar, R. M. Tripathi and V. D. Puranik, “Thoron interference test of different continuous passive radon monitors,” Radiation Protection and Environment, vol. 34, no. 4, pp. 257–261, 2011.

Manufacturing and Printing of Urogenital System Organs

Osman GÜNAY[1]✉, Fahrettin Fatih KESMEZACAR[2], Yağmur İdil ULUSOY[3] , Duygu TUNÇMAN KAYAOKAY[4], Özge DEMİR[5], Songül KARAÇAM[4], Eren ÖZGÜR[6], Nami YEYİN[7], Rabia Lebriz USLU BEŞLİ[7], Mustafa DEMİR[7],

[1]Yildiz Technical University, Faculty of Electrical & Electronics, Biomedical Engineering, Istanbul-Türkiye
[2]Istanbul University-Cerrahpas¸a, Vocational School of Health Services, Department of Medical Services and Techniques, Medical Monitoring Techniques Pr., Istanbul-Türkiye
[3]Istanbul Bilgi University, Vocational School of Health Services, Medical Imaging Techniques Programme, Istanbul-Turkiye
[4]Istanbul University-Cerrahpas¸a, Vocational School of Health Services, Department of Medical Services and Techniques, Radiotherapy Pr., Istanbul-Türkiye
[5]İstanbul University-Cerrahpaşa, Engineering Faculty, Chemical Engineering Department, Avcılar 34320, İstanbul-Turkey
[6]Istanbul Training and Research Hospital, Radiology Department, Istanbul, Türkiye
[7]Istanbul University- Cerrahpasa, Cerrahpasa Faculty of Medicine, Department of Nuclear Medicine, Istanbul-Türkiye

ABSTRACT

Radiation is commonly used in the medical field, primarily for diagnostic purposes and, in some cases, for therapeutic applications. In hospitals, it is employed in radiology, nuclear medicine, and radiation oncology departments. Unlike other applications, nuclear medicine involves the injection of a radioactive substance directly into the patient's body. This radioactive material disperses throughout the entire body, with a significant portion accumulating in the bladder before being excreted. The radioactive substances collected in the bladder also irradiate the nearby genital organs.

The aim of this study is to design and fabricate models simulating the organs of the urogenital system using three-dimensional (3D) printing technology. In subsequent stages, these printed organs will be assembled into a urogenital system phantom, enabling experimental investigations for various applications in nuclear medicine.

Keywords: *Radiation , phantom , urogenital*

✉ *Corresponding Author Email : ogunay@yildiz.edu.tr*

1 INTRODUCTION

Radiation is energy emitted from matter in the form of electromagnetic waves or particles. Fundamentally, radiation is classified into two main categories: non-ionizing radiation, which cannot ionize atoms (such as radio waves and microwaves), and ionizing radiation, which has sufficient energy to ionize atoms (such as X-rays, gamma rays (γ), and beta (β) particles). While non-ionizing radiation does not possess enough energy to cause ionization, ionizing radiation is capable of removing electrons from atoms.

Radiation is widely used in nuclear facilities, nuclear research centers, food technology, non-destructive testing methods, characterization of material structures, and medical applications, and its range of applications continues to expand.

In the healthcare sector, particularly in hospitals, radiation applications are employed across many departments; however, they are mainly utilized in three core units: radiology, nuclear medicine, and radiation oncology. In radiology, the ionizing radiation most commonly used is X-rays. X-rays form the basis of imaging modalities such as conventional radiography, computed tomography (CT), mammography, and fluoroscopy. In radiation oncology, high-energy X-rays and gamma rays are generally employed. In oncology, X-rays are delivered using linear accelerators (LINACs), while gamma rays are commonly used in brachytherapy applications. In hospital nuclear medicine departments, gamma rays are typically used in gamma cameras and single-photon emission computed tomography (SPECT), whereas positron emission tomography (PET) utilizes positrons (beta-plus, β^+) along with gamma rays.

The main objective of this study is to design a phantom to be used in experimental studies for nuclear medicine applications. For this purpose, organ designs were first developed, followed by the 3D printing stage.

2 MATERIALS AND METHODS

KIDNEYS

The kidneys are located in the retroperitoneal space between the T12 and L3 vertebral levels. The right kidney is typically positioned 0.5–1 cm lower than the left kidney due to the presence of the liver. The right kidney lies inferior to the liver, while the left kidney is adjacent to the spleen, pancreas, and stomach.

The measurements presented in this report consist of two parts. The first part includes measurements compiled from the literature, while the second part is based on computed tomography (CT) images obtained from a patient (Fig 1).

Figure 1. Kidney

URINARY BLADDER

The urinary bladder is located in the anterior part of the pelvis, posterior to the pubic symphysis and anterior to the uterus. In females, it lies in front of the uterus and vagina. When empty, the bladder is situated within the lesser pelvis, whereas when filled, it ascends into the abdominal cavity. The empty bladder has a pear-shaped appearance, becoming more spherical as it fills. Its length can reach 12–15 cm, and its width may increase up to 8–10 cm. In an average adult, the bladder capacity is approximately 400–600 mL. The maximum tolerable capacity may reach 800–1000 mL in some individuals [1], however, this exceeds normal physiological limits. The bladder is positioned within the pelvic cavity, posterior to the pubic bone. Its posterior relations in females include the vagina and uterus, while its inferior relations are formed by the pelvic floor muscles and the urethra.

UTERUS

The uterus is a hollow, muscular organ of the female reproductive system that supports fetal development during pregnancy. It is located in the female pelvis between the urinary bladder and the rectum. The uterus consists of three main parts: the cervix, corpus, and fundus. Under normal conditions, it is positioned in anteversion and anteflexion; that is, the cervix is oriented approximately perpendicular to the pelvic axis, and the corpus is flexed anteriorly.

The bladder lies anterior to the uterus, the rectum posterior to it, and the vagina inferiorly. These anatomical relationships are of critical importance in surgical and radiological planning. Laterally, the uterus is associated with the fallopian tubes and ovaries (Figure 2).

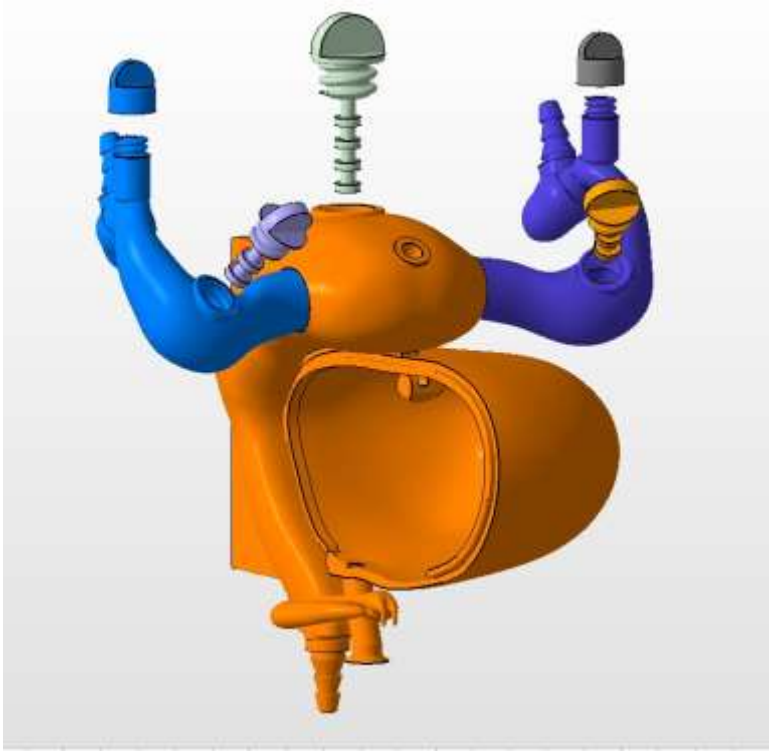

Figre 2 : Uterus

FALLOPIAN TUBES

The fallopian tubes extend laterally from the fundus of the uterus and course toward the ovaries. They consist of four main segments: the infundibulum, ampulla, isthmus, and pars uterina. Medially, they are related to the uterine fundus, while laterally they are associated with the ovaries. On average, the diameters of the infundibulum, ampulla, and isthmus are approximately 5–8 mm, 6–10 mm, and 2–4 mm, respectively. The mean length of the fallopian tubes is 10–12 cm [2] with reported lengths ranging between 8 and 14 cm [3].

3 RESULTS

The three-dimensional drawing of the kidney is shown in Figure 3. In this figure, the lidded component located in the upper right from the reader's perspective is a valve designed to prevent air

from being trapped inside the kidney during the filling process. As fluid is introduced into the kidney, air will be expelled through this valve, which will be closed once all the air has been released. The component located in the upper left is designed as slots for the placement of thermoluminescent dosimeters (TLDs).

The TLDs will be mounted onto the grooved, green-colored holder and suspended into the kidney. The opening located at the upper center represents the inlet ports for the fluid entering the kidney. Of the two outlet ports located at the bottom, one directs the flow toward the urinary bladder, while the other leads to the uterus.

The combined drawing of the bladder, uterus, ovaries, and fallopian tubes is shown in Figure 4. Two air-release valves were placed at the highest points of the ovarian channels on the right and left sides. Fluid inlets were positioned at the upper points on both the right and left sides. Two TLD access ports were created on the right and left sides of the ovarian channels, and one TLD access port was created for the uterus. In Figure 4, of the two openings located at the bottom, one serves as the fluid outlet for the uterus and the other as the fluid outlet for the bladder.
During the experiments, a saline bag will be placed inside the phantom to allow the bladder to expand and contract. As the bladder fills, the saline bag will expand and surround the bladder from the inside.

The 3D manufacturing process of the female urogenital system organs was initiated by transferring the digitally designed models in STL format to a 3D printer. The printing process was carried out according to the following steps:

1. Slicing Process:

- The prepared STL files were converted into layers using slicing software compatible with the 3D printer.
- The layer thickness was set to 0.2 mm, which was considered optimal in terms of both surface smoothness and printing time.
- The infill density was selected between 30% and 80%, balancing structural strength and material consumption.
-

2. Printing Parameters:

- Material used: ABS filament
- Extruder temperature: 230–240 °C
- Build plate temperature: 100–110 °C
- Printing speed: 40–60 mm/s
- To improve layer adhesion, the build plate surface was covered with special tape and adhesive solutions.

3. Support and Raft Structures:

- Automatic support structures were generated for organs with complex geometries (e.g., fallopian tubes) to prevent overhangs.
- After printing, these support structures were removed, and surface smoothness was ensured.

4. Printing Time:

- Depending on the size of the organ, the printing time varied between 2 and 8 hours.
- Larger-volume organs (e.g., the uterus) required longer printing durations.

5. Post-Processing:

- Support structures were manually removed after printing, and surface sanding was applied where necessary.
- In some organs, the ABS surface was smoothed by acetone exposure to achieve a more realistic appearance.
- The models were color-coded according to their anatomical differences to facilitate educational use.

Acrylonitrile Butadiene Styrene (ABS) is one of the most commonly used engineering plastics and one of the most preferred thermoplastic polymers in 3D printing technologies. The selection of ABS filament for the production of female urogenital system organs was based on its mechanical and physical advantages.

The properties of ABS are as follows:

- **Chemical Structure:** ABS is a terpolymer composed of acrylonitrile, butadiene, and styrene.
    - *Acrylonitrile* → Provides chemical resistance and rigidity.
    - *Butadiene* → Enhances impact resistance and flexibility.
    - *Styrene* → Contributes gloss, processability, and surface smoothness.
- **Density:** Approximately 1.04 g/cm³
- **Melting/Printing Temperature Range:** Suitable for printing between 210–250 °C

Figure 3. Kidney (Printed)

Figure 4. Uterus (Printed)

4 CONCLUSION

Figures 5 and 6 present views of the printed organs from different orientations. The organs produced by the three-dimensional printer were observed to be suitable for their intended purpose.

Figures 6 show the organs after printing, assembled using intravenous (IV) tubing. After being connected with the tubing to form the phantom, leak-tightness tests were performed. During these tests, some leakage issues were encountered; however, the majority of the sealing problems were successfully resolved.

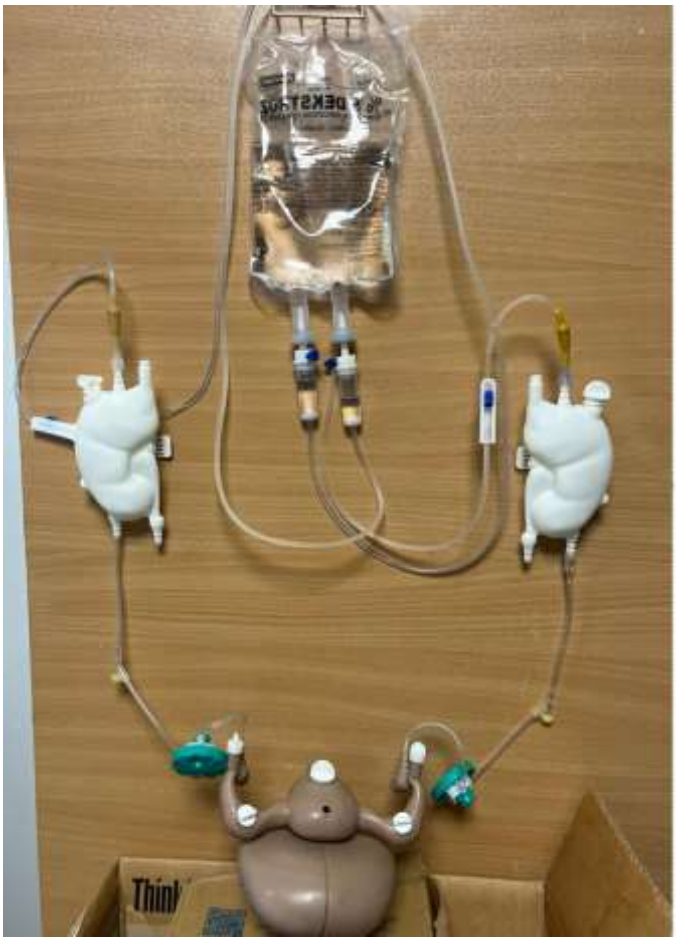

Figure 5. Uregenital system

Figure 6. Uregenital system experiment level

REFERENCES

[1] Hayta, E. ve Ceyhan Doğan, S. (2013) Mesane Anatomisi ve Nörofizyolojisi , Türkiye Klinikleri J PMR Special Topics 6(2):1-7

[2] Warda, O., Ragab, A. and Elshamy M.R. (2024), Manuel of Gynecology , https://medfac.mans.edu.eg/images/Depts/OBSGYN/MANUAL_OF_GYNECOLOGY.pdf

[3] Chard, T. and Grudzinskas G. (2003), The Uterus, Published by the Press Syndicate of the University of Cambridge, Australia

Organ-Specific Dosimetry in Ovarian Vein Embolization

Cemre Serdem BİLİR[1], Osman GÜNAY[2], Fahrettin Fatih KESMEZACAR[3], Özge COŞKUN SAĞLAM[4], Berrin YALÇIN[5], Murat ÖZOĞUL[6]

[1]*Yıldız Technical University, Biomedical Engineering Department, Istanbul-Türkiye*
[2]*Yıldız Technical University, Department of Biomedical Engineering, Istanbul, Türkiye*
[3]*Istanbul University-Cerrahpasa, Vocational School of Health Services, Department of Medical Imaging Techniques, Istanbul, Türkiye*
[4]*Istanbul Bilgi University, Faculty of Health Sciences, Department of Physiotherapy and Rehabilitation, Istanbul- Türkiye*
[5]*Istanbul Training and Research Hospital, Department of Radiation Oncology, Istanbul- Türkiye*
[6]*Istanbul Training and Research Hospital, Department of Radiology, Istanbul- Türkiye*

ABSTRACT

Transcatheter ovarian vein embolization (TOVE) is an invasive radiological procedure. This procedure is used in the treatment of pelvic congestion syndrome. Even though this procedure offers clinical benefits, this method relies heavily on fluoroscopic imaging, which inevitably reveals not only the targeted vessels but also the surrounding pelvic structures. Distant organs may be exposed to ionizing radiation. Understanding the distribution and magnitude of this exposure is important to minimize potential risks and optimize procedure safety. With this study, a phantom based dosimetric approach was used to evaluate organ specific radiation doses during TOVE under simulated clinical conditions. A phantom was used and thermoluminescent dosimeters (TLDs) were strategically placed at eleven anatomical sites, right ovary, left ovary, right uterine tube, left uterine tube, corpus uteri, fundus uteri, cervix uteri, bladder, vagina, rectouterine pouch, Medulla spinalis (MS). Dose measurements were recorded following a standard protocol.

The results showed that the medulla spinalis absorbed the highest radiation dose (10.87 mSv), followed by the rectouterine pouch (9.03 mSv) and the corpus uteri (7.63 mSv). The lowest exposure was observed in the bladder region (3.49 mSv). Moreover, the left uterine tube (7.72 mSv) received a slightly higher dose than the right tube (6.78 mSv), this can be attributed to the projection geometry and beam angle during imaging. These findings suggest that radiation exposure during TOVE is significantly influenced by the anatomical location of the organ relative to the treatment field. Data from this phantom model highlight the importance of dose optimization strategies and careful adjustment of imaging parameters to reduce unnecessary exposure. Given that the study simulated bilateral procedures with deliberately increased fluoroscopy, the reported organ doses should be interpreted as upper limit estimates of clinical exposure. These results provide a conservative yet valuable reference for patient safety assessments and underscore the necessity of dose optimization strategies in TOVE.

Keywords: transcatheter ovarian vein embolization, radiation exposure, organ-specific dosimetry, phantom model, thermoluminescent dosimeter, pelvic congestion syndrome.

✉ *Corresponding Author Email : cemreserdem@gmail.com*

1.INTRODUCTION

Radiation is a emission and transfer of energy through waves or particles. In medicine, ionizing radiation such as X-rays is used for imaging and treatment. It provides detailed visualization of internal organs but must be carefully controlled due to its biological effects.

Accurate quantification of radiation exposure during fluoroscopy-guided endovascular procedures is essential for ensuring patient safety and optimizing interventional practice. In medical imaging, **ionizing radiation** refers to high-energy electromagnetic radiation (most commonly X-rays) capable of removing electrons from atoms and molecules, thereby producing ionization in biological tissues. This interaction may lead to biological effects that depend on dose magnitude, exposure duration, and irradiated tissue characteristics; therefore, optimization of imaging parameters and dose monitoring are integral components of modern interventional radiology.

Pelvic Congestion Syndrome (PCS) is a chronic venous disorder characterized by ovarian vein insufficiency and pelvic venous dilatation, frequently presenting with persistent pelvic pain in women of reproductive age. Transcatheter ovarian vein embolization (OVE) is widely accepted as a minimally invasive and clinically effective treatment approach for PCS. However, OVE relies heavily on real-time fluoroscopic guidance using C-arm systems, which inevitably exposes radiosensitive pelvic organs—particularly the uterus, ovaries, and surrounding soft tissues—to repeated X-ray irradiation.

In the existing literature, the majority of reports focus on technical success, clinical outcomes, pain relief, and anatomical considerations related to PCS, whereas comparatively fewer studies examine **organ-specific radiation dose distribution** during OVE. This scarcity creates an evidence gap regarding absorbed dose levels in pelvic organs, spatial dose variation within the body, and the quantitative relationship between fluoroscopic parameters and organ exposure. Moreover, the biological radiosensitivity of reproductive organs underscores the need for precise dosimetric evaluation in fluoroscopy-guided pelvic interventions. Anthropomorphic phantoms, combined with thermoluminescent dosimeters (TLDs), provide a reliable and standardized method for organ-level dose measurement. These models replicate human anatomy with high fidelity and enable insertion of dosimeters into anatomically relevant cavities, allowing simulation of realistic irradiation conditions under controlled environments.

The primary aim of this study is to quantify organ-specific absorbed radiation doses during simulated ovarian vein embolization (OVE) using an anthropomorphic female pelvic phantom. TLD-100 dosimeters were placed in selected anatomical sites, and standardized fluoroscopic imaging was performed on a clinical C-arm system to assess radiation exposure. This study aims to determine organ-level absorbed doses and evaluate the influence of fluoroscopic parameters on radiation exposure, thereby providing data to support dose optimization and radiation safety in clinical OVE practice.

2. MATERIALS AND METHODS

This experimental phantom-based dosimetry study was designed to simulate transcatheter ovarian vein embolization (OVE) under clinical fluoroscopic conditions and to quantify organ-specific absorbed radiation doses using thermoluminescent dosimeters (TLD-100).

2.1 Study Design

A controlled experimental setup was implemented to simulate the standard fluoroscopic workflow of ovarian vein embolization. Thermoluminescent dosimeters (TLDs) were positioned in anatomically representative regions of a female anthropomorphic phantom. Fluoroscopic image acquisitions were performed to correspond with routine procedural steps of OVE. Dose-related parameters, including fluoroscopy time, cumulative air kerma, and dose–area product (DAP), were recorded for each acquisition. All imaging procedures were conducted using a Siemens Artis Zee Floor C-arm angiography system under routine clinical operating conditions. Exposure parameters, including tube voltage (kVp), tube current (mA), pulse rate, field size, and beam filtration, were documented systematically to ensure reproducibility and enable comparison with standard clinical practice.

2.2 Phantom Model

In this experimental dosimetric study, a CIRS anthropomorphic female pelvic phantom was used to simulate patient-specific pelvic anatomy during ovarian vein embolization. The phantom consists of tissue-equivalent materials arranged in 2.5 cm–thick axial slices, designed to accurately reproduce human anatomical geometry and radiological properties.

Each slice contains predefined cavities corresponding to anatomical organ locations, allowing for precise and reproducible placement of TLD-100 dosimeters. Dosimeters were positioned at selected sites representing relevant pelvic organs and anatomical regions of interest. The phantom was positioned in the supine position on the angiography table in accordance with standard clinical patient positioning to ensure realistic irradiation geometry during fluoroscopic imaging.

2.3 Thermoluminescent Dosimeters (TLDs)

TLD-100 (LiF:Mg,Ti) chips were selected for dose measurement due to their high sensitivity, tissue-equivalent response, and suitability for low-dose fluoroscopic applications. Prior to irradiation, all dosimeters underwent a standardized annealing procedure consisting of heating at 400 °C for 1 hour, followed by cooling to room temperature and a secondary annealing step at 100 °C for 2 hours.

Following irradiation, the TLDs were read using a thermoluminescent dosimeter reading system under controlled laboratory conditions. Individual element correction factors (ECFs) were applied to reduce inter-dosimeter variability. Calibration curves were generated using known reference exposures obtained from the angiography system and were used to convert TLD readout signals into absorbed dose values.

2.4 Fluoroscopic Procedure

To simulate the workflow of ovarian vein embolization, fluoroscopic imaging was performed in a series of sequential steps representative of routine clinical practice. The procedure consisted of an initial pelvic survey fluoroscopy, followed by simulated catheter navigation toward the ovarian vein, selective ovarian vein imaging, and fluoroscopy during embolization simulation.

All imaging steps were conducted using standard fluoroscopic parameters. For each exposure sequence, total fluoroscopy time (s), cumulative air kerma (mGy), and dose–area product (DAP; Gy·cm²) were automatically recorded by the C-arm system.

3. RESULTS

Dose measurements collected from strategically positioned TLDs within the **CIRS** anthropomorphic female pelvic phantom demonstrated discernible variation among pelvic organs during the simulated embolization process. Mean absorbed dose values for each organ are presented in Table 1.1

Organ	TLD No	Mean Dose (mSv)
Right ovary	75–76	4.24mSv
Left ovary	73–74	5.43mSv
Right uterine tube	49–50	6.78mSv
Left uterine tube	45–46	7.72mSv
Corpus uteri	81–82	7.63mSv
Fundus uteri	71–72	4.86mSv
Bladder	69–70	3.49mSv
Cervix uteri	77–78	5.53mSv
Rectouterine pouch	61–62	9.03mSv
Vagina	79–80	4.08mSv
MS (medulla spinalis)	83-84	10.87mSv

Table 1.1

Among measured sites, the medulla spinalis exhibited the greatest absorbed dose (10.87 mSv), with the rectouterine pouch and left uterine tube following at 9.03 mSv and 7.72 mSv, respectively.4.1.2 Comparison Between Right and Left Organs. A consistent lateral difference was observed, wherein tissues on the left side of the pelvis accumulated greater radiation than their right-sided counterparts. For example, the left ovary absorbed 5.43 mSv compared to 4.24 mSv on the right, and the left fallopian tube accumulated 7.72 mSv relative to 6.78 mSv on the opposite side.

4. DISCUSSION

This study presents a controlled experimental evaluation of organ-specific radiation exposure during simulated ovarian vein embolization using an anthropomorphic pelvic phantom. The findings

demonstrate that centrally and posteriorly located pelvic structures, particularly the uterus and rectouterine region, are subjected to higher absorbed radiation doses during fluoroscopic imaging. This dose distribution is consistent with the projection geometry of the X-ray beam and the anatomical location of the target vessels during OVE.

Published data addressing organ-level dosimetry in OVE are limited, restricting direct comparison with existing studies. Nevertheless, the measured absorbed dose values fall within the range reported for fluoroscopy-guided pelvic interventions. Variations in dose distribution are likely influenced by factors such as C-arm geometry, beam angulation, and positioning, all of which play a critical role in determining organ exposure during interventional procedures.

A clear relationship was observed between cumulative air kerma, dose–area product, and measured organ doses, supporting the clinical utility of these parameters as practical indicators of radiation exposure. However, the results also highlight that absolute organ dose estimation cannot be reliably achieved using global dose metrics alone and remains dependent on anatomical configuration and direct dosimetric assessment.

From a clinical perspective, these findings underscore the importance of optimizing fluoroscopic technique to minimize radiation exposure to radiosensitive pelvic organs. Strategies such as reducing fluoroscopy time through pulsed imaging, optimizing collimation to limit irradiation of non-target tissues, selecting low-dose imaging protocols when diagnostically sufficient, and maintaining appropriate patient and C-arm positioning may substantially reduce unnecessary radiation burden.

Several limitations should be acknowledged. The use of an anthropomorphic phantom does not fully account for inter-patient anatomical variability, and the static experimental setup differs from dynamic catheter manipulation encountered in clinical practice. Additionally, the spatial resolution of TLDs is limited compared with advanced dosimetric technologies, and only a standardized procedural workflow was simulated without evaluation of operator-dependent variability. Despite these constraints, the study provides a reproducible methodological framework for assessing pelvic organ doses during fluoroscopy-guided ovarian vein embolization and contributes valuable data to support radiation safety and dose optimization efforts.

5. CONCLUSION

This phantom-based dosimetric investigation demonstrates that fluoroscopy-guided ovarian vein embolization results in measurable and clinically relevant radiation exposure to pelvic organs. Higher absorbed dose levels were observed in centrally and posteriorly located pelvic structures, particularly the uterus, highlighting the influence of beam orientation, irradiation geometry, and tissue depth on organ dose distribution during the procedure.

By providing quantitative organ-specific absorbed dose data and examining the relationship between fluoroscopic exposure parameters and measured doses, this study contributes to a better understanding of radiation dose behavior during OVE. The findings support the importance of optimizing fluoroscopic technique, including appropriate parameter selection and positioning, to minimize unnecessary radiation exposure to radiosensitive pelvic organs.

Overall, the results of this study offer experimental evidence that may aid in the development of optimized imaging protocols, strengthen radiation safety strategies, and improve clinical awareness

of patient dose during fluoroscopy-guided ovarian vein embolization, thereby contributing to safer and more informed interventional radiology practice.

REFERENCES

1. **International Commission on Radiological Protection (ICRP).** Radiological protection in fluoroscopically guided procedures. *ICRP Publication 85*. Ann ICRP. 2000;30(2).
2. **International Commission on Radiological Protection (ICRP).** The 2007 recommendations of the International Commission on Radiological Protection. *ICRP Publication 103*. Ann ICRP. 2007;37(2–4).
3. **Balter S, Hopewell JW, Miller DL, Wagner LK, Zelefsky MJ.** Fluoroscopically guided interventional procedures: a review of radiation effects on patients' skin and hair. *Radiology*. 2010;254(2):326–341.
4. **Miller DL, Balter S, Dixon RG, et al.** Quality improvement guidelines for recording patient radiation dose in the medical record. *J Vasc Interv Radiol*. 2012;23(1):11–18.
5. **Rafferty EA, Henkelman RM.** Thermoluminescent dosimetry for diagnostic radiology. *Radiology*. 1988;168(3):849–854.
6. **McCollough CH, Schueler BA.** Calculation of effective dose. *Med Phys*. 2000;27(5):828–837.
7. **Hart D, Hillier MC, Wall BF.** Doses to patients from medical X-ray examinations in the UK. *Br J Radiol*. 2009;82(973):1–12.
8. **Belli AM, Markose G, Morgan R.** The role of interventional radiology in the management of pelvic congestion syndrome. *Cardiovasc Intervent Radiol*. 2012;35(4):791–800.
9. **Ganeshan A, Upponi S, Hon LQ, et al.** Chronic pelvic pain due to pelvic congestion syndrome: the role of diagnostic and interventional radiology. *Cardiovasc Intervent Radiol*. 2007;30(6):1105–1111.
10. **Laborda A, Medrano J, De Blas I, Urtiaga I, Carnevale FC, De Gregorio MA.** Endovascular treatment of pelvic congestion syndrome: visual analog scale follow-up results. *Eur J Radiol*. 2013;82(11):e639–e645.
11. **Schueler BA.** The AAPM/RSNA physics tutorial for residents: general overview of fluoroscopic imaging. *Radiographics*. 2000;20(4):1115–1126.
12. **Vañó E, Fernández JM, Sánchez RM, et al.** Patient radiation dose management in interventional radiology: a practical approach. *Cardiovasc Intervent Radiol*. 2010;33(4):688–699.
13. **Dance DR, Christofides S, Maidment ADA, McLean ID, Ng KH.** *Diagnostic Radiology Physics: A Handbook for Teachers and Students.* Vienna: IAEA; 2014.
14. **Bushberg JT, Seibert JA, Leidholdt EM, Boone JM.** *The Essential Physics of Medical Imaging.* 3rd ed. Philadelphia: Lippincott Williams & Wilkins; 2012.

PET/CT versus Conventional Imaging in Cancer Diagnosis: Evidence from a Comprehensive Meta-Analysis

Osman GÜNAY[1]✉ , Ümmühan ZENGİN ÖZER[1], Muhammet Mert ÇELİK[1]

[1]*Yıldız Technical University, Faculty of Electrical and Electronics Engineering, Department of Biomedical Engineering, Istanbul, Türkiye*

ABSTRACT

Accurate and timely diagnosis is essential for effective treatment planning in oncology. Conventional imaging modalities, including magnetic resonance imaging (MRI), bone scintigraphy, and computed tomography (CT), are widely used in the evaluation of prostate and breast cancers; however, their overall diagnostic performance remains limited. This study compared the diagnostic accuracy of positron emission tomography/computed tomography (PET/CT) with conventional imaging techniques and examined the influence of tracer selection (^{11}C-Choline, ^{18} F-FDG, ^{18} F-NaF) on diagnostic yield. A comprehensive meta-analysis of 29 studies published after 2010 was conducted. Diagnostic metrics, including sensitivity, specificity, accuracy, positive likelihood ratio (PLR), negative likelihood ratio (NLR), and diagnostic odds ratio (DOR), were systematically assessed.

PET/CT demonstrated significantly greater diagnostic accuracy than conventional modalities, with pooled improvements in sensitivity (+13.69%), specificity (+7.30%), and accuracy (+9.72%) (all $p<0.01$). In prostate cancer, PET/CT showed distinct advantages in sensitivity ($Z=2.819$, $p=0.005$), specificity ($Z=2.275$, $p=0.023$), and accuracy ($Z=3.237$, $p=0.001$). Compared with MRI, PET/CT achieved superior accuracy ($Z=1.956$, $p=0.050$), while relative to bone scintigraphy, it yielded higher accuracy and PLR values. Subgroup analysis indicated that ^{11}C-Choline PET/CT provided the most consistent diagnostic performance, whereas ^{18} F-FDG and ^{18} F-NaF showed non-significant trends. PET/CT demonstrates superior diagnostic performance compared with conventional imaging, particularly in prostate cancer. Tracer selection substantially influences diagnostic value, with ^{11}C-Choline providing the most consistent benefit. PET/CT, when combined with appropriate tracer choice, may support more accurate diagnosis and facilitate optimized treatment planning in oncology.

Keywords: *PET/CT, Diagnostic Imaging, Conventional Imaging Techniques, Meta-Analysis, Radiopharmaceuticals.*

✉ *Corresponding Author Email : ogunay@yildiz.edu.tr*

1 INTRODUCTION

Effective treatment decisions and positive patient outcomes in oncology depend on accurate and timely diagnosis. Medical imaging provides essential tools to detect and monitor cancer [1]. Diagnostic imaging has advanced to include powerful hybrid techniques such as positron emission tomography/computed tomography (PET/CT). PET/CT combines information from both modalities: PET depicts the metabolic activity of organs and tissues, whereas CT provides detailed anatomical images, including cross-sectional views of the body [2].

However, PET/CT is often used alongside, rather than distinctly from, conventional imaging methods such as magnetic resonance imaging (MRI) and bone scintigraphy (BS), and may therefore not be utilized to its full potential. Several meta-analyses have attempted to clarify its added value. Although previous work has compared multiple cancer types, specific clinical indications, or selected comparator modalities, there is still an evidence gap for contemporary (post-2010) comprehensive comparisons that include both prostate and breast cancer and directly contrast key diagnostic performance indicators.

The primary aim of this study is to statistically evaluate and compare the diagnostic performance of PET/CT with that of conventional imaging modalities in prostate and breast cancer. This work provides a detailed statistical analysis of head-to-head comparative studies to establish a clearer understanding of the relative diagnostic value of PET/CT across different oncological settings. By analyzing metrics such as sensitivity, specificity, and accuracy, and by examining the influence of PET tracer selection, this paper seeks to generate evidence that can better inform clinical decision-making.

2 MATERIALS AND METHODS

The purpose of this study is to conduct a meta-analysis to evaluate how PET/CT differs from other imaging modalities in oncological diagnosis, particularly in prostate and breast cancer.

2.1 Literature Search and Study Selection

The relevant literature was searched in several databases, including MEDLINE, PubMed, ScienceDirect, and Google Scholar, focusing on studies published from 2010 onwards. The search strategy used a combination of keywords, including but not limited to “PET/CT”, “MRI”, “bone scintigraphy”, “conventional imaging”, “comparative”, “cancer”, and “diagnosis”. This screening process resulted in the inclusion of 29 studies in our analysis, as shown in the flow diagram in Figure 1.

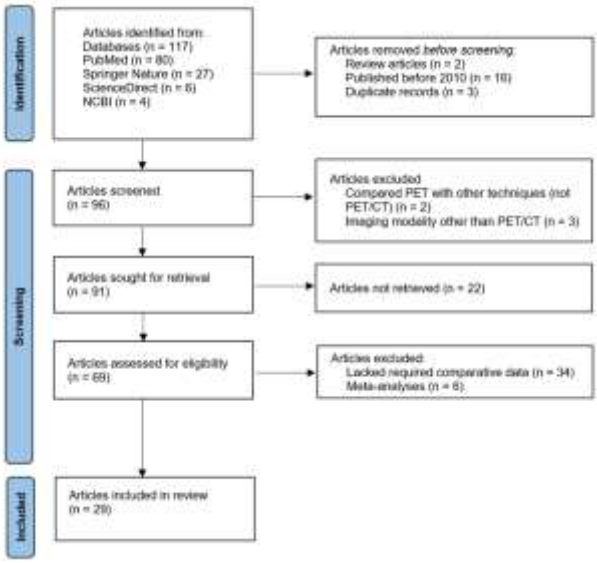

Figure 1. Flow diagram illustrating the study selection process.

2.2 Data Extraction

From each of the 29 studies, the following data were collected: the last name of the first author, year of publication, type of cancer, PET radiotracer used, imaging method used as comparator, and the numbers of true positives (TP), false positives (FP), true negatives (TN), and false negatives (FN) for both PET/CT and the comparator methods.

2.3 Data Analysis

All statistical analyses were performed using IBM SPSS Statistics for Windows, Version 26.0. In some studies, performance metrics were missing. To increase statistical power and avoid bias associated with casewise deletion, Multiple Imputation (MI) was applied. Ten imputed datasets were generated, and all statistical analyses were subsequently conducted on the pooled results.

The main diagnostic metrics, i.e. sensitivity, specificity, and accuracy, were derived from TP, FP, TN, and FN values unless they were explicitly reported in the original publication. Additional derived metrics, including the Positive Likelihood Ratio (PLR), Negative Likelihood Ratio (NLR), and Diagnostic Odds Ratio (DOR), were calculated using equations (2.1)–(2.3):

PLR = Sensitivity / (1 − Specificity)
(2.1)

$$NLR = (1 - \text{Sensitivity}) / \text{Specificity} \quad (2.2)$$

$$DOR = PLR / NLR \quad (2.3)$$

To avoid problems arising from undefined values in cases where sensitivity or specificity were equal to 100% or 0%, a continuity correction ($\varepsilon = 0.001$) was applied. To compare the overall diagnostic performance of PET/CT and conventional methods, difference variables were calculated for each performance metric. Because each study used the same patient cohort for both imaging methods, statistical tests for dependent (paired) samples were used. The Shapiro–Wilk test was employed to assess the normality of the difference variables.

A paired-samples t-test was used for normally distributed data, whereas the non-parametric Wilcoxon signed-rank test was applied when the normality assumption was not met. The outcomes from the 10 imputed datasets were pooled to obtain a single mean difference or median Z-statistic together with the associated p-value.

3 RESULTS

3.1 Overall Diagnostic Performance

A meta-analysis of 29 unique studies demonstrated the superior diagnostic performance of PET/CT (positron emission tomography/computed tomography) over conventional imaging modalities. Results from the paired-samples t-test (Table 1) showed that PET/CT provided statistically significant improvements in sensitivity (mean difference 13.69%; 95% confidence interval [CI] 3.75–21.04; $p < 0.001$), specificity (mean difference 7.30%; 95% CI 1.73–12.86; $p = 0.010$), and accuracy (mean difference 9.72%; 95% CI 5.68–13.75; $p < 0.001$) across the included studies.

Table 3.1 Pooled Paired Samples T-Test results for differences in primary diagnostic performance metrics between PET/CT and comparator methods

Performance Metric Difference	Mean Difference (PET/CT - Comparator) (%)	95% Confidence Interval (Difference) (%)	t-statistic	df[1]	p-value	Interpretation (Favoring PET/CT)
Difference in Sensitivity (%)	+13.69	(3.75 – 21.04)	6.341	3.65	<.001	Significantly Higher
Difference in Specificity (%)	+7.30	(1.73 – 12.86)	2.570	N/R[2]	.010	Significantly Higher
Difference in Accuracy (%)	+9.72	(5.68 – 13.75)	4.720	1.12	<.001	Significantly Higher

[1]df = degrees of freedom. For pooled results from multiple imputation, the df is an adjusted value calculated according to Rubin's rules and may not be an integer. It reflects the variability within and between imputations.
[2]N/R = Not Reported; the pooled degrees of freedom for this specific test was not directly reported in the SPSS output

Assessments of the other derived metrics were consistent with the above results. PET/CT was found to have a significantly higher positive likelihood ratio (PLR) (median Z = 3.276; p = 0.001) and a significantly lower negative likelihood ratio (NLR) (median Z = −3.341; p = 0.001). Statistically, this indicates that a positive PET/CT result is more effective in confirming the presence of disease, and a negative PET/CT result is more effective in ruling out disease, compared with conventional imaging. In addition, the overall diagnostic odds ratio (DOR) was significantly higher for PET/CT (median Z = 2.368; p = 0.018).

These general findings are consistent with previous work (e.g. Xu et al.) and are particularly relevant to the demonstrated superiority of PET/CT in detecting distant metastases, now further supported and extended by more recent post-2010 studies [3].

3.2 Subgroup Analyses: Performance in Specific Contexts

From the subgroup focused solely on prostate cancer (N = 18), PET/CT showed a substantial and statistically meaningful advantage in almost all measures. As detailed in Table 2, sensitivity (median Z = 2.819; p = 0.005), specificity (median Z = 2.275; p = 0.023), and accuracy (median Z = 3.237; p = 0.001) were all significantly improved in Wilcoxon signed-rank tests. Additionally, PLR was significantly higher (p = 0.002), whereas NLR was significantly lower (p = 0.004). These robust findings confirm the effectiveness of PET/CT in prostate cancer staging and in monitoring disease progression, further corroborating the results reported by Zhan et al. and Liu et al. [4][5]. Although DOR showed an upward trend (p = 0.053), the evidence did not reach conventional statistical significance, likely due to the combined variance of the metrics and the smaller sample size compared with the overall analysis.

Conversely, subgroup analysis among breast cancer patients (N = 4) found no significant differences in any diagnostic measure between PET/CT and the comparator methods. This likely reflects the small number of available studies and the resulting limited statistical power. In addition, standard methods such as mammography and breast MRI are already highly effective diagnostic tools in many clinical scenarios, which may lead to a “ceiling effect,” whereby demonstrating the superiority of another modality becomes exceedingly difficult [6].

When PET/CT was compared with MRI alone (N = 12), PET/CT showed higher accuracy and a trend toward better specificity. This suggests that the functional metabolic information provided by PET complements the excellent anatomical detail of MRI, thereby improving the differentiation of active disease from benign changes.

Table 2. Wilcoxon Signed-Rank Test results for diagnostic performance in the prostate cancer subgroup (N=18).

Performance Metric Difference	Median Z-Statistic	Median p-value	Interpretation (Favoring PET/CT)
Difference in Sensitivity	2.819	.005	Significantly Higher
Difference in Specificity	2.275	.023	Significantly Higher
Difference in Accuracy	3.237	.001	Significantly Higher
Difference in PLR	3.070	.002	Significantly Higher
Difference in NLR	-2.853	.004	Significantly Lower (Better Performance)
Difference in DOR	1.938	.053	Trend towards Higher (Not Sig. at α=.05)

In comparison with bone scintigraphy (BS) (N = 11), PET/CT outperformed BS in terms of accuracy and PLR and showed a trend toward a higher DOR. This is clinically relevant because BS is a highly sensitive method for detecting bone metastases, but it is known for its relatively low specificity. PET/CT maintains high sensitivity while offering greater diagnostic certainty.

The diagnostic advantage of PET/CT was also strongly dependent on the PET tracer used. In the subgroup of studies using ^{11}C-choline (N = 5), PET/CT demonstrated significantly higher accuracy (median Z = 2.023; p = 0.043) and PLR (p = 0.043), with a strong trend toward better specificity (p = 0.068). This was the most consistent performance observed among the tracers. By contrast, analyses for ^{18}F-FDG (N = 9) and ^{18}F-NaF (N = 6) showed positive but non-significant trends in favour of PET/CT.

The variable results among tracers highlight an important finding: appropriate application and selection of radiopharmaceuticals are crucial. Choline-based tracers are particularly effective in prostate cancer, and the present results reflect this. This underscores the importance of choosing tracers according to the underlying cancer biology. These conclusions are also in line with network meta-analyses that have identified PSMA-based tracers as superior in prostate cancer imaging [5]. Ultimately, PET/CT offers a substantial diagnostic advantage; however, its value is maximized when the imaging context and tracer selection are carefully aligned with the clinical question.

4 CONCLUSION

This meta-analysis provides evidence that PET/CT offers superior diagnostic performance compared with conventional imaging modalities, particularly for the diagnosis and staging of prostate cancer. By improving the ability to detect disease and distinguish it from healthy or benign tissue, PET/CT demonstrates significantly higher overall sensitivity, specificity, and accuracy. The results also indicate that the diagnostic advantage of PET/CT is not universal but depends on the clinical context and the choice of PET tracer. ^{11}C-choline PET/CT shows a clear and consistent diagnostic benefit, whereas the advantages of ^{18} F-FDG and ^{18} F-NaF are less pronounced. The practical implication for the nuclear medicine community is that the use of PET/CT, when combined with an appropriate tracer selected for the specific cancer type, can lead to more accurate diagnoses. Consequently, PET/CT represents a powerful tool to improve patient stratification and, ultimately, to facilitate more effective treatment planning in oncology.

REFERENCES

[1] H. N. Wagner, Jr. and P. S. Conti, «Advances in medical imaging for cancer diagnosis and treatment», Cancer, vol. 67, pp. 1121-1128, 1991.

[2] M. K. Werner, H. Schmidt, and N. F. Schwenzer, «MR/PET: A New Challenge in Hybrid Imaging», American Journal of Roentgenology, vol. 199, no. 2, pp. 272-277, 2012.

[3] G. Xu, J. Li, X. Zuo, and C. Li, «Comparison of whole body positron emission tomography (PET)/PET-computed tomography and conventional anatomic imaging for detecting distant malignancies in patients with head and neck cancer: a meta-analysis», Laryngoscope, vol. 122, no. 9, pp. 1974-1978, 2012.

[4] Y. Zhan, G. Zhang, M. Li, and X. Zhou, «Whole-Body MRI vs. PET/CT for the Detection of Bone Metastases in Patients With Prostate Cancer: A Systematic Review and Meta-Analysis», Front. Oncol., vol. 11, p. 633833, 2021.

[5] F. Liu, J. Dong, Y. Shen, C. Yun, R. Wang, G. Wang, et al., «Comparison of PET/CT and MRI in the Diagnosis of Bone Metastasis in Prostate Cancer Patients: A Network Analysis of Diagnostic Studies», Front. Oncol., vol. 11, p. 736654, 2021.

[6] L. Chen, Q. Yang, J. Bao, D. Liu, X. Huang, and J. Wang, «Direct comparison of PET/CT and MRI to predict the pathological response to neoadjuvant chemotherapy in breast cancer: a meta-analysis», Sci. Rep., vol. 7, no. 1, p. 8479, 2017.

[7] S. H. Ng, S. C. Chan, T. C. Yen, K. H. Wong, S. M. Jung, Y. C. Chen, and C. C. Chou, «Comprehensive imaging of residual/recurrent nasopharyngeal carcinoma using whole-body MRI at 3 T compared with FDG-PET-CT», Eur Radiol, vol. 20, pp. 2229-2240, 2010.

[8] H. Wieder, A. J. Beer, K. Holzapfel, M. Henninger, T. Maurer, S. Schwarzenboeck, E. J. Rummeny, M. Eiber, and J. Stollfuss, «11C-choline PET/CT and whole-body MRI including diffusion-weighted imaging for patients with recurrent prostate cancer», Oncotarget, vol. 8, pp. 66516-66527, 2017.

[9] K. Kitajima, K. Fukushima, S. Yamamoto, T. Kato, S. Odawara, H. Takaki, M. Fujiwara, K. Yamakado, Y. Nakanishi, A. Kanematsu, M. Nojima, and S. Hirota, «Diagnostic performance of

11C-choline PET/CT and bone scintigraphy in the detection of bone metastases in patients with prostate cancer», Nagoya J Med Sci, vol. 79, no. 3, pp. 387-399, 2017.

[10] I. Jambor, A. Kuisma, S. Ramadan, R. Huovinen, M. Sandell, S. Kajander, and J. Seppänen, «Prospective evaluation of planar bone scintigraphy, SPECT, SPECT/CT, 18F-NaF PET/CT and whole body 1.5T MRI, including DWI, for the detection of bone metastases in high risk breast and prostate cancer patients: SKELETA clinical trial», Acta Oncologica, vol. 55, no. 1, pp. 59-67, 2015.

[11] A. Iagaru, E. Mittra, D. W. Dick, J. W. Clark, D. A. Chin, A. S. Rosenblat, K. A. McDougall, and D. C. Tong, «Prospective Evaluation of 99mTc MDP Scintigraphy, 18F NaF PET/CT, and 18F FDG PET/CT for Detection of Skeletal Metastases», Mol Imaging Biol, vol. 14, no. 3, pp. 252-259, 2012.

[12] M. H. Poulsen, H. Petersen, P. F. Høilund-Carlsen, J. S. Jakobsen, O. Gerke, J. Karstoft, S. I. Steffansen, and S. Walter, «Ability of imaging techniques to detect bone metastases in prostate cancer», BJU Int, vol. 114, pp. 818-823, 2014.

[13] H. D. Zacho, J. B. Nielsen, A. Afshar-Oromieh, J. Fledelius, R. H. Jensen, R. Krarup, M. Loft, L. Løgager, N. L. Larsen, F. Mortensen, S. Walter, H. D. Kvistad, and J. Poulsen, «Prospective comparison of 68Ga-PSMA PET/CT, 18F-sodium fluoride PET/CT and diffusion weighted-MRI at for the detection of bone metastases in biochemically recurrent prostate cancer», Eur J Nucl Med Mol Imaging, vol. 45, no. 11, pp. 1884-1897, 2018.

[14] K. Kitajima, R. C. Murphy, M. A. Nathan, A. T. Froemming, C. E. Hagen, N. Takahashi, and A. Kawashima, «Detection of Recurrent Prostate Cancer After Radical Prostatectomy: Comparison of 11C-Choline PET/CT with Pelvic Multiparametric MR Imaging with Endorectal Coil», Journal of Nuclear Medicine, vol. 55, no. 2, pp. 223-232, 2014.

[15] S. H. Park, W. K. Moon, N. Cho, J. H. Son, S. W. Yoon, M. S. Lee, Y. M. Kim, K. S. Oh, S. S. Lee, Y. Choi, and J. S. Kim, «Comparison of diffusion-weighted MR imaging and FDG PET/CT to predict pathological complete response to neoadjuvant chemotherapy in patients with breast cancer», Eur Radiol, vol. 22, no. 1, pp. 18-25, 2012.

[16] Y. Kawanaka, K. Kitajima, S. Yamamoto, T. Okamura, Y. Nakanishi, and K. Yamakado, «Comparison of 11C-choline Positron Emission Tomography/Computed Tomography (PET/CT) and Conventional Imaging for Detection of Recurrent Prostate Cancer», Cureus, vol. 10, no. 7, pp. e2966, 2018.

[17] R. F. Fonager, H. D. Zacho, N. C. Langkilde, J. Fledelius, J. A. Ejlersen, C. Haarmark, H. W. Hendel, M. B. Lange, M. R. Jochumsen, J. C. Mortensen, and L. J. Petersen, «Diagnostic test accuracy study of 18F-sodium fluoride PET/CT, 99mTc-labelled diphosphonate SPECT/CT, and planar bone scintigraphy for diagnosis of bone metastases in newly diagnosed, high-risk prostate cancer», Am J Nucl Med Mol Imaging, vol. 7, no. 5, pp. 218-227, 2017.

[18] J. C. Janssen, S. Meißner, N. Woythal, M. Gose, S. Schirutschke, R. G. Vija, E. Busemann-Sokole, and R. Knijn, «Comparison of hybrid 68Ga-PSMA-PET/CT and 99mTc-DPD-SPECT/CT for the detection of bone metastases in prostate cancer patients: Additional value of morphologic information from low dose CT», Eur Radiol, vol. 28, no. 1, pp. 610-619, 2018.

[19] E. K. Choi, I. R. Yoo, H. L. Park, J. M. Jeong, S. W. Lee, Y. S. Kim, T. W. Kim, K. Y. Kim, S. Y. Hyun, C. H. Oh, T. K. Lee, H. L. Lee, S. K. Jang, M. D. Oh, and D. W. Kim, «Value of

Surveillance 18F-FDG PET/CT in Colorectal Cancer: Comparison with Conventional Imaging Studies», Nucl Med Mol Imaging, vol. 46, no. 3, pp. 189-195, 2012.

[20] R. L. U. Beşli, M. S. Sağer, E. Akgün, S. Asa, O. E. Şahin, Ç. Demirdağ, E. Güner, S. Razavikhosroşahi, E. Karayel, H. Pehlivanoğlu, A. Aygün, İ. Uslu, Z. Talat, and K. Sönmezoğlu, «Comparison of Ga-68 PSMA positron emission tomography/computerized tomography with Tc-99m MDP bone scan in prostate cancer patients», Turkish Journal of Medical Sciences, vol. 49, no. 1, pp. 45, 2019.

[21] M. Takesh, K. O. Allh, S. Adams, and C. Zechmann, «Diagnostic Role of 18F-FECH-PET/CT Compared with Bone Scan in Evaluating the Prostate Cancer Patients Referring with Biochemical Recurrence», International Scholarly Research Notices, pp. 815234, 2012.

[22] N. A. Damle, C. Bal, G. P. Bandopadhyaya, R. Kumar, A. C. Bhasin, A. Shamim, P. Singh, R. R. Sharma, and C. S. Bal, «The role of 18F-fluoride PET-CT in the detection of bone metastases in patients with breast, lung and prostate carcinoma: a comparison with FDG PET/CT and 99mTc-MDP bone scan», Jpn J Radiol, vol. 31, no. 4, pp. 262-269, 2013.

[23] K.-H. Ly, N. Costedoat-Chalumeau, E. Liozon, S. Dumonteil, J.-P. Ducroix, L. Sailler, O. Lidove, B. Bienvenu, O. Decaux, P.-Y. Hatron, A. Smail, L. Astudillo, N. Morel, J. Boutemy, A. Perlat, E. Denes, M. Lambert, T. Papo, A. Cypierre, and A. Fauchais, «Diagnostic Value of 18F-FDG PET/CT vs. Chest-Abdomen-Pelvis CT Scan in Management of Patients with Fever of Unknown Origin, Inflammation of Unknown Origin or Episodic Fever of Unknown Origin: A Comparative Multicentre Prospective Study», Journal of Clinical Medicine, vol. 11, no. 2, pp. 386, 2022.

[24] W. Huysse, F. Lecouvet, P. Castellucci, P. Ost, V. Lambrecht, C. Artigas, M.-L. Denis, K. D. Man, L. Delrue, L. Jans, A. D. Bruycker, F. D. Vos, G. D. Meerleer, K. Decaestecker, V. Fonteyne, and B. Lambert, «Prospective Comparison of F-18 Choline PET/CT Scan Versus Axial MRI for Detecting Bone Metastasis in Biochemically Relapsed Prostate Cancer Patients», Diagnostics, vol. 7, no. 4, pp. 56, 2017.

[25] E. Dyrberg, H. W. Hendel, T. H. V. Huynh, L. H. Løgager, N. C. Langkilde, S. Walter, and H. D. Zacho, «68Ga-PSMA-PET/CT in comparison with 18F-fluoride-PET/CT and whole-body MRI for the detection of bone metastases in patients with prostate cancer: a prospective diagnostic accuracy study», Eur Radiol, vol. 29, no. 3, pp. 1221-1230, 2019.

[26] T. Lengana, I. O. Lawal, T. G. Boshomane, C. Van de Wiele, M. Vorster, and M. M. Sathekge, «68Ga-PSMA PET/CT Replacing Bone Scan in the Initial Staging of Skeletal Metastasis in Prostate Cancer: A Fait Accompli?», Seminars in Nuclear Medicine, vol. 16, no. 5, pp. 392-401, 2018.

[27] E. W. Johnston, A. Latifoltojar, H. S. Sidhu, N. Galazi, S. K. K. Main, A. M. Davda, S. M. Janes, S. Lee, and S. K. Punwani, «Multiparametric whole-body 3.0-T MRI in newly diagnosed intermediate- and high-risk prostate cancer: diagnostic accuracy and interobserver agreement for nodal and metastatic staging», Eur Radiol, vol. 29, no. 6, pp. 3159-3169, 2019.

[28] F. Mosavi, S. Johansson, D. T. Sandberg, I. Turesson, J. Sörensen, and H. Ahlström, «Whole-Body Diffusion-Weighted MRI Compared With ^{18} F-NaF PET/CT for Detection of Bone Metastases in Patients With High-Risk Prostate Carcinoma», American Journal of Roentgenology, vol. 199, no. 5, pp. 1231-1239, 2012.

[29] G. Rusu, P. Achimaș-Cadariu, A. Piciu, S. S. Căinap, C. Căinap, and D. Piciu, «A Comparative Study between 18F-FDG PET/CT and Conventional Imaging in the Evaluation of Progressive Disease and Recurrence in Ovarian Carcinoma», Healthcare, vol. 9, no. 6, pp. 666, 2021.

[30] Y. Y. An, S. H. Kim, B. J. Kang, and A. W. Lee, «Treatment Response Evaluation of Breast Cancer after Neoadjuvant Chemotherapy and Usefulness of the Imaging Parameters of MRI and PET/CT», J Korean Med Sci, vol. 30, no. 6, pp. 808-815, 2015.

[31] G. Xu, J. Li, X. Zuo, and C. Li, «Comparison of whole body positron emission tomography (PET)/PET-computed tomography and conventional anatomic imaging for detecting distant malignancies in patients with head and neck cancer: A meta-analysis», The Laryngoscope, vol. 122, no. 9, pp. 1974-1978, 2012.

[32] M. Picchio, E. G. Spinapolice, F. Fallanca, C. C. M. Alongi, A. He-Sellam, I. Castellucci, L. Nanni, M. G. Dei Tos, M. Lazzeri, A. Freschi, M. R. M. N. De Cobelli, C. F. F. Mattioli, and F. T. T. Grimaldi, «[11C]Choline PET/CT detection of bone metastases in patients with PSA progression after primary treatment for prostate cancer: comparison with bone scintigraphy», Eur J Nucl Med Mol Imaging, vol. 39, no. 1, pp. 13-26, 2012.

[33] M. Wondergem, F. M. van der Zant, R. J. J. Knol, W. R. R. de Klerk, and P. P. van Rijk, «99mTc-HDP bone scintigraphy and 18F-sodiumfluoride PET/CT in primary staging of patients with prostate cancer», World J Urol, vol. 36, no. 1, pp. 27-34, 2018.

[34] A. J. Conde-Moreno, G. Herrando-Parreño, R. Muelas-Soria, M. M. Rebollo, J. P. Catalá-Vázquez, and I. Tortajada-Almela, «Whole-body diffusion-weighted magnetic resonance imaging (WB-DW-MRI) vs choline-positron emission tomography-computed tomography (choline-PET/CT) for selecting treatments in recurrent prostate cancer», Clin Transl Oncol, vol. 19, no. 5, pp. 553-561, 2017.

[35] T. J. Hieken, J. C. Boughey, K. N. Jones, A. A. S. Jawale, A. C. Degnim, V. S. Pankratz, and T. L. Hoskin, «Imaging Response and Residual Metastatic Axillary Lymph Node Disease after Neoadjuvant Chemotherapy for Primary Breast Cancer», Ann Surg Oncol, vol. 20, no. 10, pp. 3199-3204, 2013.

Comparative Analysis of Linear and Mass Attenuation Coefficients of PLA Filaments for Radiation Shielding Applications

Hilal ÖZTÜRK[1]✉ , Osman GÜNAY[2]

[1]*Karadeniz Technical University, Faculty of Medicine, Department of biophysics, Trabzon, Türkiye*

[2]*Yıldız Technical University, Faculty of Electrical and Electronics Engineering, Department of Biomedical Engineering, Istanbul, Türkiye*

ABSTRACT

The linear attenuation coefficient (LAC) and mass attenuation coefficient (MAC) are critical parameters in describing the interaction of radiation with matter. In this work, PLA filament samples, commonly used in 3D printing, were investigated by means of simulation to obtain their energy-dependent attenuation coefficients. Photon energies from diagnostic to therapeutic ranges were employed, and the resulting LAC and MAC values were benchmarked. The study provides a fundamental database of attenuation coefficients for PLA, supporting its evaluation as a candidate material in lightweight shielding prototypes and biomedical phantom construction.

Keywords: *LAC, MAC, Attenuation*

✉ *Corresponding Author Email : hilalozturk@ktu.edu.tr*

1 INTRODUCTION

Understanding how radiation interacts with matter is essential for a wide range of applications, from medical imaging and therapy to radiation protection and dosimetry. Among the key parameters used to describe these interactions are the linear attenuation coefficient (LAC) and the mass attenuation coefficient (MAC), both of which provide insight into how a material absorbs or scatters incoming photons. These coefficients not only help determine the shielding efficiency of a given substance but also play a vital role in the design of dosimetric phantoms and simulation models used in radiation studies[1-5].

With the growing accessibility of additive manufacturing (3D printing), new materials such as polylactic acid have emerged as potential candidates for experimental and educational use in radiation-related fields. PLA is biodegradable, inexpensive, and easy to shape into complex geometries, which makes it particularly attractive for producing customized radiation phantoms and lightweight shielding components. However, despite its popularity in engineering and biomedical

applications, the attenuation characteristics of PLA across different photon energies remain relatively underexplored.

This study aims to fill that gap by determining the energy-dependent LAC and MAC values of PLA through simulation. Photon energies covering both diagnostic and therapeutic ranges were modeled to assess how efficiently PLA attenuates radiation under different energy conditions. The results obtained from this work are intended to serve as a reference database for researchers and engineers evaluating PLA's potential in radiation physics and medical applications.

2 MATERIALS AND METHODS

In this study, simulations were carried out to determine the linear attenuation coefficient (LAC) and mass attenuation coefficient (MAC) of polylactic acid (PLA) using the Phy-X Monte Carlo simulation code. The software allows precise modeling of photon transport and interaction mechanisms, making it suitable for evaluating radiation attenuation behavior in various materials.

A monoenergetic photon beam was simulated with energy values ranging from 20 keV to 10 MeV, covering both diagnostic and therapeutic energy ranges. The simulation geometry consisted of a narrow beam setup, where the photon source was directed perpendicularly toward a PLA slab of variable thickness. This configuration minimizes the contribution of scattered photons and provides accurate primary attenuation data.

The physical and chemical composition of PLA was defined according to its empirical formula $C_3 H_4 O_2$, with an assumed density of 1.24 g/cm³. The attenuation process was analyzed by recording the incident (I0I_0I0) and transmitted (III) photon intensities for each energy level. The linear attenuation coefficient (μ) was calculated using the standard exponential attenuation law.

Each simulation was repeated several times to ensure statistical consistency, and the averaged results were compared with reference data from the NIST XCOM database for validation. The obtained LAC and MAC values were subsequently plotted as a function of photon energy to visualize the energy-dependent attenuation characteristics of PLA.

3 RESULTS

Simulations were performed for photon energies ranging from tens of keV up to several MeV, and the corresponding LAC and MAC values for PLA were extracted. The results showed a clear inverse relationship between photon energy and attenuation coefficients: both LAC and MAC values decreased as photon energy increased.

This trend is consistent with the general behavior observed in low-Z materials, where photoelectric absorption dominates at low energies, while Compton scattering becomes the prevailing interaction mechanism in the intermediate and high-energy regions.

At lower photon energies (below 100 keV), the LAC values were relatively high, indicating strong attenuation due to photoelectric effects. As the photon energy rose beyond 500 keV, both coefficients gradually leveled off, suggesting that Compton scattering was the dominant interaction process.

The obtained attenuation data were found to be in good agreement with NIST XCOM reference values, validating the accuracy of the simulation setup. These results, illustrated in Figure 1 (for MAC) and Figure 2 (for LAC), provide a comprehensive overview of the energy-dependent attenuation behavior of PLA, confirming its predictable and stable response over a broad photon energy range.

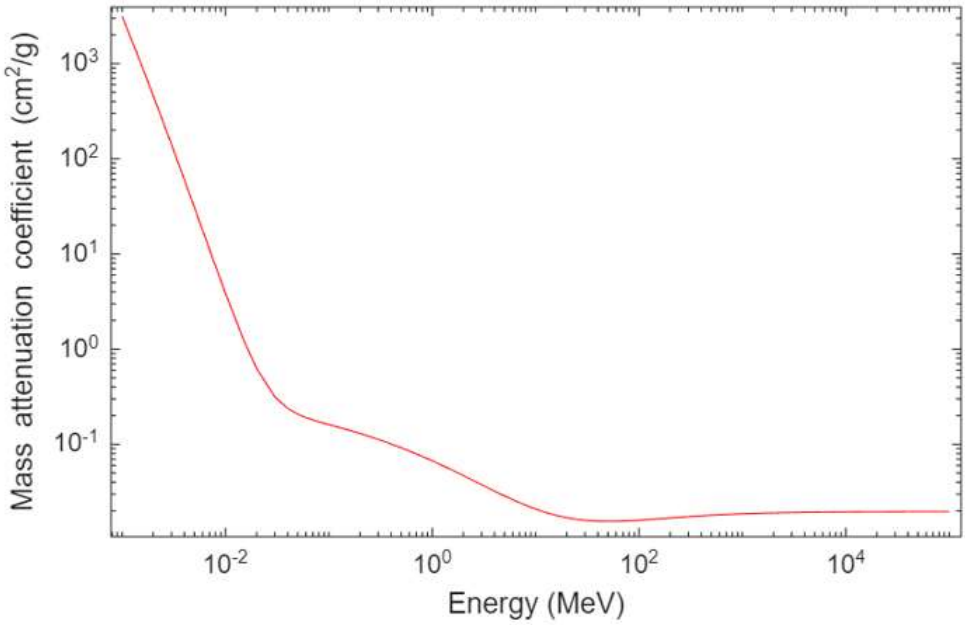

Figure 1. Mass atteneation coefficent

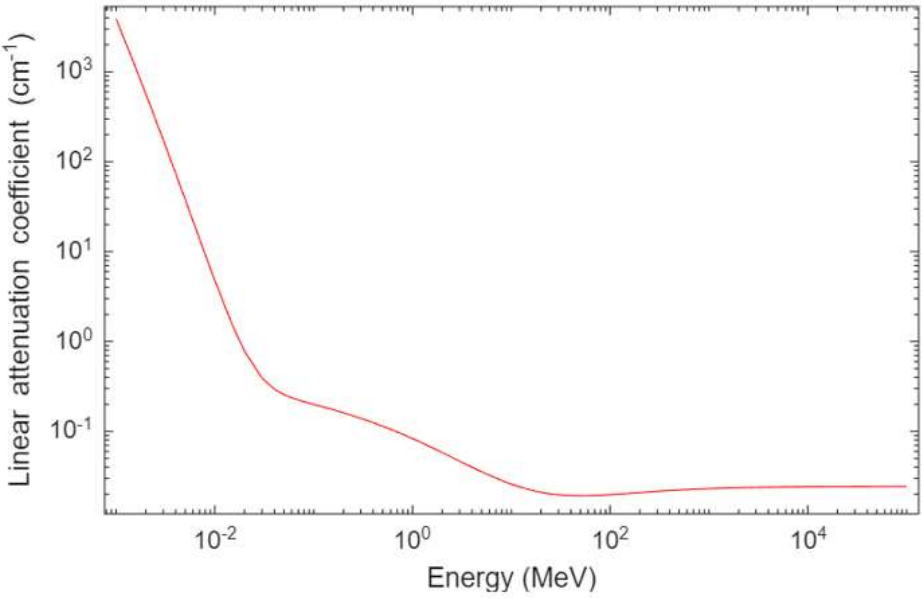

Figure 2. Linear attenuation coefficent

4 CONCLUSION

This study presented a systematic simulation-based evaluation of the linear and mass attenuation coefficients (LAC and MAC) of polylactic acid (PLA) over a wide photon energy spectrum. The findings demonstrated that both coefficients decrease with increasing photon energy, reflecting the transition from photoelectric absorption to Compton scattering dominance.

The results provide a reliable set of reference data for PLA, which can be used in radiation transport modeling, phantom design, and lightweight shielding applications. Given its ease of processing and environmental advantages, PLA can serve as a practical material for educational setups, low-dose simulation environments, and experimental radiation measurements where conventional shielding materials may be impractical.

Future work may include experimental validation of these simulated values and the exploration of composite PLA materials with high-Z additives to enhance shielding performance at higher photon energies.

REFERENCES

[1] Şahin MC, Manisa K (2023) Evaluation of X-Ray Shielding Ability of Tungsten Rubber: A GAMOS Monte Carlo Study. Süleyman Demirel University Faculty of Arts and Sciences Journal of Science 18(1):1-9

[2] Agar O (2018) Study on Gamma Ray Shielding Performance of Concretes Doped with Natural Sepiolite Mineral. Radichim. Acta 106:1009-1016

[3] Kumar A, Gaikwad DK, Obaid SS, Tekin HO, Agar O, Sayyed MI (2020) Experimental Studies and Monte Carlo Simulations on Gamma Ray Shielding Competence of (30+x) PbO-10WO_3-10Na_2O-10MgO-(40-x)B_2O_3 Glasses. Prog. Nucl. Energy. 119:103047

[4]Altunsoy, E.E., Tekin, H.O., Mesbahi, A., Akkurt, I., 2020. MCNPX simulation for radiation dose absorption of anatomical regions and some organs. Acta Phys. Pol., A 137, 561–565.

[5]Henaish, A.M.A., Mostafa, M., Salem, B.I., Zakaly, H.M.H., Issa, S.A.M., Weinstein, I.A., Hemeda, O.M., 2020. Spectral, electrical, magnetic and radiation shielding studies of Mg-doped Ni–Cu–Zn nanoferrites. J. Mater. Sci. Mater. Electron. 22, 1–13.

Evaluation of Mean Free Path of PLA-Based Printing Materials through Monte Carlo Simulation

Nuray KUTU[1]✉ Osman GÜNAY[2]

[1]Suleyman Demirel University, Physics Department, Isparta, Turkey
[21]Yıldız Technical University, Faculty of Electrical and Electronics Engineering, Department of Biomedical Engineering, Istanbul, Türkiye

ABSTRACT

The mean free path (MFP) is a fundamental measure representing the average distance traveled by photons before undergoing interaction with matter. In this research, the MFP values of polylactic acid (PLA) filaments were computed using a simulation.

Simulations were performed over a broad photon energy spectrum, and the calculated MFP values exhibited a strong dependence on photon energy, increasing steadily with higher energies. These results provide insight into the penetration depth of radiation in PLA-based structures and are particularly relevant for additive manufacturing of custom shielding devices. This results are emphasizes the practical applicability of PLA in radiation-related experimental setups.

Keywords: *MFP, PLA, Simulation*

✉ *Corresponding Author Email : nuraykutu@sdu.edu.tr*

1 INTRODUCTION

When radiation passes through a material, it doesn't move in a straight line forever — eventually, the photons interact with the atoms inside. The mean free path (MFP) is a simple but very useful concept that tells us, on average, how far a photon travels before one of those interactions happens. In other words, it's a measure of how deeply radiation can penetrate a material[1-6].

In recent years, 3D printing materials like polylactic acid have drawn attention in radiation studies because they're lightweight, cheap, and easy to shape into almost any form. This makes them perfect for custom shielding parts, phantoms, and test setups. But to use polylactic acid effectively in those areas, we need to understand how radiation behaves inside it — and that's where MFP comes in.

In this study, we used simulation techniques to calculate the mean free path values of polylactic acid over a wide range of photon energies. By doing so, we aimed to see how photon energy affects the depth of radiation penetration and to evaluate whether polylactic acid can be a practical option for radiation-related applications.

2 MATERIALS AND METHODS

The mean free path (MFP) of PLA was calculated using the Phy-X simulation program, which is based on the Monte Carlo method for modeling radiation transport. The simulation setup used a monoenergetic photon beam directed perpendicularly onto a PLA sample.

Photon energies covered a wide spectrum — from 20 keV to 10 MeV — allowing us to investigate how MFP changes across both diagnostic and therapeutic ranges. The physical properties of PLA were defined according to its chemical composition ($C_3\ H_4\ O_2$) and density of 1.24 g/cm³.

For each energy level, the linear attenuation coefficient (μ) was obtained, and the mean free path was calculated using the simple relationship:

$$MFP = \frac{1}{\mu}$$

All simulations were run multiple times to minimize statistical uncertainty, and the results were compared with NIST XCOM reference data to ensure consistency.

3 RESULTS

The simulation results showed a clear energy dependence of the mean free path in PLA. At lower photon energies (below about 100 keV), the MFP values were small — meaning radiation was quickly absorbed or scattered. As photon energy increased, the MFP grew steadily, indicating deeper penetration through the PLA structure.

This behavior is typical for low atomic number (low-Z) materials, where photoelectric absorption dominates at low energies, and Compton scattering becomes the main interaction process at higher energies. The upward trend of MFP with energy, shown in Figure 1, aligns well with the theoretical expectations and with reference data from standard databases.

Overall, the results demonstrate that PLA offers predictable and stable radiation interaction behavior, which makes it easier to model and apply in radiation studies.

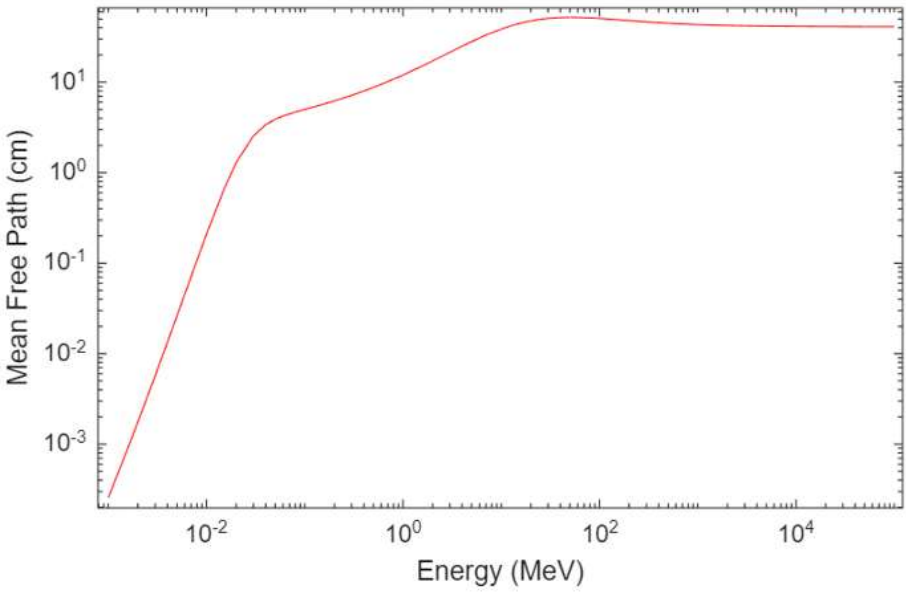

Figure 1. Mean Free Path

4 CONCLUSION

This study explored the mean free path (MFP) of polylactic acid (PLA) using a simulation-based approach over a wide photon energy range. The results clearly showed that MFP increases as photon energy rises, meaning radiation travels further inside PLA at higher energies.

These findings give valuable insight into how deep photons can penetrate PLA-based materials, helping researchers design custom shielding devices and radiation phantoms more effectively. In

practical terms, the study supports the idea that PLA can be a reliable and flexible material for various radiation-related experiments — especially in 3D-printed setups where traditional shielding materials are not ideal.

REFERENCES

[1]Jawad, A.A., Demirkol, N., Gunoglu, K., Akkurt, I., 2019. Radiation shielding properties of some ceramic wasted samples. Int. J. Environ. Sci. Technol. 16, 5039–5042.Kulali, F., 2020. Simulation studies on radiological parameters for marble concrete. Emerg. Mater. Res. 9, 1341–1347.

[2] Bashter II. Calculation of radiation attenuation coefficients for shielding concretes.Ann Nucl Energy 1997;24:1389–401. https://doi.org/10.1016/s0306-4549(97)00003-0.

[3] Ilik E, Kavaz E, Kilic G, Issa SAM, Ghada ALMisned, H.O. Tekin, Synthesis and characterization of vanadium(V) oxide reinforced calcium-borate glasses:Experimental assessments on Al2O3, BaO2, ZnO contributions, Journal of NonCrystalline Solids, Volume 580,. 121397. ISSN 2022;0022–3093. https://doi.org/10.1016/j.jnoncrysol.2022.121397.

[4]Akkurt, I., Tekin, H.O., 2020. Radiological parameters for bismuth oxide glasses using phy-X/PSD software. Emerg. Mater. Res. 9, 1020–1027.

[5] Şakar, E., Özpolat, Ö. F., Alım, B., Sayyed, M. I., & Kurudirek, M. (2020). Phy-X/PSD: development of a user friendly online software for calculation of parameters relevant to radiation shielding and dosimetry. Radiation Physics and Chemistry, 166, 108496.

[6] A.A. Alfuraih Simulation of Gamma-Ray Transmission Buildup Factors forStratified Spherical Layers Dose Response 20 1 2022 Feb 17 155932582110686251 0.1177/15593258211070911.

.